DEMOCRATIC AND POPULAR REPUBLIC OF ALGERIA

MINISTRY OF HIGHER EDUCATION AND SCIENTIFIC RESEARCH
UNIVERSITY MOHAMED BOUDIAF OF M'SILA - M'SILA

Faculty of Sciences

Department of Physics

Option: Applied Physics

Serial N°: ……..

Enrolment N°: D.PHM/3C/04/17

Thesis

Submitted to obtain the degree of

3rd Cycle Doctorate

Entitled

Synthesis, characterization and study of the properties of zinc oxide-based nanocomposites

Presented By:

Benrezgua Elhadj

Defended on: 13 / 07 / 2021

In front of the jury composed of:

Name & First name	**Grade**	**Establishment**	**Quality**
Belhouchet Hocine	Pr	Mohamed Boudiaf University of M'sila	President
Deghfel Bahri	Pr	Mohamed Boudiaf University of M'sila	Supervisor
Mahroug Abdelhafid	MCA	Mohamed Boudiaf University of M'sila	Co-Supervisor
Labga Noudjoud	MCA	Mohamed El Bachir El Ibrahimi University of BBA	Examiner
Mezahi Fatima Zohra	MCA	Mohamed Boudiaf University of M'sila	Examiner
Meglali Omar	MCA	Mohamed Boudiaf University of M'sila	Examiner

Academic year: **2020 /2021**

ACKNOWLEDGEMENTS

Praise be to **Allah** for the success in the realization and completion of this work.

I would like to express my sincere gratitude to my supervisor **Pr. DEGHFEL Bahri**, I am grateful to him for having directed my work while leaving me free to explore my ideas. I thank him for his advice, opinion, help, and for being present and motivating.

My sincere thanks go also to my co-supervisor **Dr. MAHROUG Abdelhafid**, for guiding me throughout achieving this work.

I am highly grateful to **Pr. AZMIN Ahmed Mohamed**, co-supervisor abroad from University of Science, Penang, Malaysia, for receiving me in his research laboratory within the framework of the exceptional national program under the academic year 2019-2020, without his support and encouragement, it would have been difficult to complete my research.

It is an honour for me that **Pr. BELHOUCHET Hocine** has accepted to chair the jury.

My sincere thanks go to **Dr. LABGA Noudjoud** from Mohamed El Bachir El Ibrahimi University of BBA for accepting to participate as an examiner in this jury.

My sincere thanks also go to **Dr. MEZAHI Fatima Zohra** for having accepted to examine this work.

My thanks also go to **Dr. MEGLALI Omar** for have being an examiner of this work.

My sincere thanks also go to my parents for their infinite patience and for providing me with an ideal working environment. This project was made possible thanks to their support.

Finally, I would like to express my deepest thanks to all the academic and administrative staff of the Physics department at MOHAMED Boudiaf University - M'sila.

E. Benrezgua 2021

TABLE OF CONTENTS

Page

CHAPTER III: Theory and computational method

CHAPTER IV: Results and discussions

LIST OF TABLES

Page

LIST OF FIGURES

Page

LIST OF FIGURES

General introduction

GENERAL INTRODUCTION

Considerable efforts are recently focused on semiconducting metal oxides materials such as TiO_2, SnO_2, ZnO and CuO, which have been the subject of a great deal of many researches and have aroused great interest in the academic and industrial world. At the nanoscale form, these materials offer a remarkable change in their properties compared to the corresponding micro and macro form. The development of such materials is linked to their attractive physical features and advantages, i.e. stable, non-toxic, low cost, etc. These materials (oxides) are good candidates for applications in different technological areas, especially in photovoltaics and optoelectronics. **[1–7]**.

Transparent Conductive Oxides (OCTs) are attractive materials in many technological areas. Their electric conductivity and transparency in the visible range, make them ideal candidates for various applications such as photovoltaics and UV photodetectors **[1, 5]**. Zinc oxide (ZnO) is a semiconductor material belonging to the family of OCTs, n-type II-VI semiconductor with a wurtzite crystal structure, a direct band gap material (Eg=3.37 eV) at room temperature, and ixhibits a high excitonic binding energy of 60 meV **[8]**. Due to its semiconducting, piezoelectric, and optical properties, ZnO offers many possible applications **[1–5]**. The improvement of the properties of ZnO thin films is commonly done through doping **[9]**. In the last decade there has been an increasing interest in ZnO thin films doped with transition metal (TM) such as Mn, Fe, Co, Ni, Cu and Ag [**10]** . Among the variety of TM, copper (Cu) has been used as dopant **[11–13]**. It exhibits an ionic radius close to that of the Zn and then can easily substitute it in ZnO host lattice. Cu dopant, as an economical option, has been chosen to change the properties of ZnO host lattice such as photocatalytic activity, conductivity and tuning of the green emission **[14,15]**.

There are various techniques that have been used to fabricate ZnO thin films such as magnetron sputtering **[16]**, sol–gel process **[17]**, **[18]**, chemical vapor deposition **[19]**, spray pyrolysis **[20]**, molecular beam epitaxy **[21]**, pulsed laser deposition (PLD) **[22]** and microwave plasma growth **[23]**. Sol–gel technique attracts much attention because of its advantages including safety, low cost, simple deposition equipment on a large-area films with uniform thickness. Properties of CZO thin films have been frequently investigated **[24–29]** but most of them are limited to some low Cu concentration.

On the other hand, ZnO is a material that contains a transition metal Zn of *3d* electrons, which provide interesting phenomena in condensed matter physics **[30, 31]**. The first-principles method based on density functional theory (DFT) in the local density approximation (LDA) has been successfully applied to study molecules, surfaces, interfaces, and solid states. This first-principles approach can accurately predict the ground state properties of materials **[32–34]**. However, this conventional approach (DFT-LDA) cannot effectively describe the localization of highly correlated *d* and *f* electrons in transition materials **[35, 36]**. To solve this problem, various corrections have been proposed such as the hybrid DFT-HF **[37]**, dynamic mean field theory (DMFT) **[38]** and DFT-LDA+U **[35]**. Thus, DFT–LDA+U approach becomes a necessity to significantly improve such calculations **[35, 39–41]**. There have been several theoretical studies on Cu doped ZnO such as **[42–47]**, which have provided some new insights into the understanding of the effect of doping on the properties of ZnO. However, the calculated band gap of CZO was found much smaller than the experimental band gap value.

The objective of this work was to deposit pure ZnO and copper-doped ZnO thin films on glass substrates using the Sol-Gel spin coating method. Then, the effect of the Cu doping concentration on the structural, optical, morphological, and electronic properties of the elaborated films, was investigated. On the other hand, the first-principles method based on DFT-LDA with the semi-empirical Hubbard U model (DFT–LDA+U), as implemented in the CASTEP code, has been applied to calculate the structural, electronic, optical, and magnetic properties of Cu-doped and undoped ZnO wurtzite materials, in order to improve especially the underestimation of the experimental energy band gap. Thus, the calculated results were compared with other experimental and theoretical results available in the literature.

The present work is based on two review papers and an original research paper. A brief outline of the whole thesis is presented in the following.

The first chapter presents a theoretical and experimental literature reviews. The first review aims to provide a timely overview on the development of CZO thin films by sol-gel, spin- and dip-coating as reported in literature survey from 2010 to 2020. Starting with preparation materials, solution preparation, depositing the materials and finally the properties of thin films. The structural, morphologies, electronic, optical, bonding, vibrational and magnetic properties as well as chemical composition of CZO thin films, will be reviewed in detail. In the second review, the progress of first-principles calculation within DFT + U method for CZO materials, are summarized. The effect of selected Hubbard-U value on the structural, optical, electronic and magnetic properties, including optimized crystal structure and calculated energy band gap, is also discussed.

The second chapter presents a general description of the sol-gel process, describes the experimental spin coating technique used to prepare thin films, discuss the elaboration protocol of doped and undoped ZnO thin films. The morphological, structural and optical characterization techniques are briefly explained.

In the third chapter, the theoretical background to the present work is laid out. The quantum mechanics, density functional theory (DFT) is introduced. Details of its implementation within the computational code used in the present calculations, i.e. *CASTEP (*Cambridge Serial Total Energy Package: Commercialized by Accelrys*) is* included. Having introduced the basic theory, we move on to the application of DFT to real systems, including the strongly localized d or f electrons**,** i.e. the Hubbard correction**.**

The fourth chapter is devoted to present and discuss the obtained results and is subdivided into two parts:

The first part focussed on the presentation of results obtained from characterization by various techniques of pure ZnO and copper-doped zinc oxide (CZO) thin films with somewhat higher Cu contents x (x = 1%, 3.12%, 6,25% and 12.5%) and low thickness. The structural, electronic and optical properties and the surface morphology of CZO thin films are then discussed.

In order to linking of experimental results with theory, usually separated in the literature, and to enhance the energy band gap, DFT–LDA+U approach was used to predict the properties of pure and CZO wurtzite structures, which were compared, wherever possible, with their corresponding measured values. These were to be the subject of the second part of the fourth chapter.

Finally, a brief summary of the main conclusions obtained either from simulation of Cu-doped ZnO wurtzite structure or various characterizations of CZO thin films, is given.

References

[1] S.H. Jeong, J.H.Park,B.T. Lee. Effects of Mg doping rate on physical properties of Mg and Al co-doped Zn1− x− 0.02 MgxAl0. 02O transparent conducting oxide films prepared by rf magnetron sputtering. Journal of alloys and compounds, 2014, vol. 617, p. 180-184.

[2] A. Das, P.G. Roya ,A. Dutta, S.Senb ,P. Pramanik ,D. Das ,A. Banerjee , A. Bhattacharyy. Mg and Al co-doping of ZnO thin films: Effect on ultraviolet photoconductivity. Materials Science in Semiconductor Processing, 2016, vol. 54, p. 36-41.

[3] A.Jayalatha, K. Jonnal ,R. Reddy,P . Srinivasan,K. Jayanth ,B. Ganesh ,K. Mani ,P. Shankar ,J. Bosco, B. Rayappan, Room temperature ammonia sensing properties of ZnO thin films grown by spray pyrolysis: Effect of Mg doping. Journal of Alloys and Compounds, 2016, vol. 688, p. 422-429.

[4] A. Chayma, B. Chaker, E. Habib,G. Bernard, and F, Mokhtar. Mg doping induced high structural quality of sol–gel ZnO nanocrystals: application in photocatalysis. Applied surface science, 2015, vol. 349, p. 855-863.

[5] A.Mahroug, S.Boudjadar, S.Hamrit,L. Guerbous, Structural, optical and photocurrent properties of undoped and Al-doped ZnO thin films deposited by sol–gel spin coating technique. Materials Letters, 2014, vol. 134, p. 248-251.

[6] S. Bhuvaneshwari ,N. Gopalakrishnan, Hydrothermally synthesized Copper Oxide (CuO) superstructures for ammonia sensing. Journal of colloid and interface science, 2016, vol. 480, p. 76-84.

[7] A. Taufik,A. Albert,R. Saleh, Sol-gel synthesis of ternary CuO/TiO2/ZnO nanocomposites for enhanced photocatalytic performance under UV and visible light irradiation. J. Photochem. Photobiol., A, 2017, vol. 344, p. 149-162.

[8] Ü. Özgür, I.Ya ,C. Alivov, A.Liu,A. Teke,M. A. Reshchikov,S. Doğan,V. Avrutin,S.-J. Cho,H. Morkoç, A comprehensive review of ZnO materials and devices. Journal of applied physics, 2005, vol. 98, no 4, p. 11.

[9] A. Mahroug. Study of thin films of Zinc Oxide doped with Aluminum and Cobalt produced by the sol gel-spin coating technique. 2015.

[10] B.G.Shohany, and, A.K. Zak. Doped ZnO nanostructures with selected elements-Structural, morphology and optical properties: A review. Ceramics International, 2020, vol. 46, no.5, p. 5507-5520.

[11] D.R. Miller, S. A. Akbar, and P. A. Morris. Nanoscale metal oxide-based heterojunctions for gas sensing: a review. Sensors and Actuators B: Chemical, 2014, vol. 204, p. 250-272.

[12] S.Parka,C. -H.Kima, W.-J. Lee ,S.Sung, M.-H. Yoon . Sol-gel metal oxide dielectrics for all-solution-processed electronics. Materials Science and Engineering: R: Reports, 2017, vol. 114, p. 1-22.

[13] A. B. Djurišić, Y.H. Leung,M.C. Nag, Strategies for improving the efficiency of semiconductor metal oxide photocatalysis. Materials Horizons, 2014, vol. 1, no 4, p. 400-410.

[14] H.A. Al-Khanbashi, W. Shirbeeny, A. A. Al-Ghamdi, L. M. Bronstein, W.E. Mahmouda. Development of highly conductive and transparent copper doped zinc oxide thin films via 2-methoxyethanol modified sol – gel dip-coating technique. Ceramics International, 2014, vol. 40, no 1, p. 1927-1932.

[15] W. Vallejo, A. Cantillo,B. Salazar ,D.-U. Carlos ,W. Ramos ,E. Romero and M. Hurtado. Comparative Study of ZnO Thin Films Doped with Transition Metals (Cu and Co) for Methylene Blue Photodegradation under Visible Irradiation. Catalysts, 2020, vol. 10, no 5, p. 528.

[16] A. Kronenberger, A.Polity, D.M. Hofmann, B.K. Meyer, A. Schleife, F.Bechstedt, Structural, electrical, and optical properties of hydrogen-doped ZnO films. Physical Review B, 2012, vol. 86, no 11, p. 115334.

[17] R. Amari, A. Mahroug, A. Boukhari, B. Deghfel, N. Selmi, Structural, optical and luminescence properties of ZnO thin films prepared by sol-gel spin-coating method: effect of precursor concentration. Chinese Physics Letters, 2018, vol. 35, no 1, p. 016801.

[18] A. Mahroug, R. Amari, A. Boukhari, B. Deghfel, L. Guerbous, N. Selmi, Synthesis, structural, morphological, electronic, optical and luminescence properties of pure and manganese-doped zinc oxide nanostructured thin films: effect of doping. Journal of Nanoelectronics and Optoelectronics, 2018, vol. 13, no 5, p. 732-742.

[19] D. Shuang, X.X. Zhu, J.B. Wang, X.L. Zhong, G.J. Huang, C. Heb, The influence of Mn content on luminescence properties in Mn-doped ZnO films deposited by ultrasonic spray assisted chemical vapor deposition. Applied surface science, 2011, vol. 257, no 14, p. 6085-6088.

[20] A. Mhamdi, R. Mimouni, A. Amlouk, M. Amlouk, and S. Belgacem, Study of copper doping effects on structural, optical and electrical properties of sprayed ZnO thin films. Journal of alloys and compounds, 2014, vol. 610, p. 250-257.

[21] Y. Darma, S. Muhammady, Y.N. Hendri, E. Sustini, R. Widita, and K. Takase, Tuning the point-defect evolution, optical transitions, and absorption edge of zinc oxide film by thermal exposure during molecular beam epitaxy growth. Materials Science in Semiconductor Processing, 2019, vol. 93, p. 50-58.

[22] Z.E. Vakulov, E.G. Zamburg, D.A. Khakhulin, O.A. Ageev, Thermal stability of ZnO thin films fabricated by pulsed laser deposition. Materials Science in Semiconductor Processing, 2017, vol. 66, p. 21-25.

[23] W. Thongsuksai, G. Panomsuwan, A. Rodchanarowan , (2018). Fast and convenient growth of vertically aligned ZnO nanorods via microwave plasma-assisted thermal evaporation. Materials Letters, 2018, vol. 224, p. 50-53.

[24] S.S. Zahirullah, J. Prince, and P. H. Inbaraj, Structural and optical properties of Cu-doped ZnO nanorods by silar method. Materials technology, 2017, vol. 32, no 12, p. 755-763.

[25] T. Saidani, M. Zaabat, M. S. Aida, B. Boudine, Effect of copper doping on the photocatalytic activity of ZnO thin films prepared by sol–gel method. Superlattices and Microstructures, 2015, vol. 88, p. 315-322.

[26] S. Osali, H. Esfahani ,F. Dabir , P.Tajaslan, Structural and electro-optical properties of electrospun Cu-Doped ZnO thin films. Solid State Sciences, 2019, vol. 98, p. 106038.

[27] A. Sreedhar, J.H. Kwon, J. Yi, J.S. Kim, J.S. Gwag, Enhanced photoluminescence properties of Cu-doped ZnO thin films deposited by simultaneous RF and DC magnetron sputtering. Materials Science in Semiconductor Processing, 2016, vol. 49, p. 8-14.

[28] K. Joshi, M. Rawat, S. K. Gautam, R. G. Singh, R. C. Ramola, F. Singh, Band gap widening and narrowing in Cu-doped ZnO thin films. Journal of Alloys and Compounds, 2016, vol. 680, p. 252-258

[29] S. Roguai, A. Djelloul, A structural and optical properties of Cu-doped ZnO films prepared by spray pyrolysis. Applied Physics A, 2020, vol. 126, no 2, p. 1-8.

[30] Y. TokurA, M. Kawasaki, and N. Nagaosa, Emergent functions of quantum materials. Nature Physics, 2017, vol. 13, no 11, p. 1056-1068.

[31] Y. Tokura, N. Nagaosa, Orbital physics in transition-metal oxides. science, 2000, vol. 288, no 5465, p. 462-468.

[32] M.K. Yaakob, M.F.M. Taib, M.S.M. Deni, A. Chandra, L. Lu, M. Z. A. Yahya, First principle study on structural, elastic and electronic properties of cubic BiFeO3. Ceramics International, 2013, vol. 39, p. S283-S286.

[33] M.F.M. Taib, M.K. Yaakob, O. H. Hassan, M.Z.A. Yahya, Structural, electronic, and lattice dynamics of PbTiO3, SnTiO3, and SnZrO3: A comparative first-principles study. Integrated Ferroelectrics, 2013, vol. 142, no 1, p. 119-127.

[34] M.F.M. Taib, M. K. Yaakob, O. H. Hassan, A. Chandra, A. K. Arof, and M. Z. A. Yahya, First principles calculation on structural and lattice dynamic of SnTiO3 and SnZrO3. Ceramics International, 2013, vol. 39, p. S297-S300.

[35] V. I. Anisimov, F. Aryasetiawan, A. I. Lichtenstein, First-principles calculations of the electronic structure and spectra of strongly correlated systems: the LDA + U method. Journal of Physics: Condensed Matter , 1997, vol. 9, no 4, p. 767.

[36] S. L. Dudarev, G. A. Botton, S. Y. Savrasov, C. J. Humphreys, A. P. Sutton . Electron-energy-loss spectra and the structural stability of nickel oxide: An LSDA + U study. Physical Review B , 1998, vol. 57, no 3, p. 1505

[37] A.D. Becke, A new mixing of Hartree–Fock and local density-functional theories. The Journal of chemical physics, 1993, vol. 98, no 2, p. 1372-1377.

[38] G. Kotliar , D. Vollhardt, Strongly correlated materials: Insights from dynamical mean-field theory. Physics today, 2004, vol. 57, no 3, p. 53-60.

[39] M.K. Yaakob, N.H. Hussin, M.F.M. Taib, T.I. T.Kudin, O.H. Hassan, A.M.M. Ali, M. Z. A. Yahya, First principles LDA+ U calculations for ZnO materials. Integrated Ferroelectrics, 2014, vol. 155, no 1, p. 15-22

[40] J.-Q. Wen, J.-M. Zhang, Z.-G. Qiu, X. Yang,Z.-Q. Li, The investigation of Ce doped ZnO crystal: the electronic, optical and magnetic properties. Physica B: Condensed Matter , 2018, vol. 534, p. 44-50.

[41] Q. Hou, D. Xi, W. Li, X. Jia, Z. Xu, First-principles research on the optical and electrical properties and mechanisms of In-doped ZnO. Physica B: Condensed Matter, 2018, vol. 537, p. 258-266.

[42] Z. Ma, F. Ren, X. Ming, Y. Long, A. A. Volinsky, Cu-doped ZnO electronic structure and optical properties studied by first-principles calculations and experiments. Materials, 2019, vol. 12, no 1, p. 196.

[43] F. Li, C. Zhang, M. Zhao. Magnetic and optical properties of Cu-doped ZnO nanosheet: First-principles calculations. Physica E: Low-dimensional Systems and Nanostructures, 2013, vol. 53, p. 101-105.

[44] L. Chen, S. Li, Y. Cui, Z. Xiong, H. Luo, Y. Gao, Manipulating the electronic and magnetic properties of ZnO monolayer by noble metal adsorption: a first-principles calculations. Applied Surface Science, 2019, vol. 479, p. 440-448.

[45] A. K. Nayek, H. Luitel, B. Haldar, D. Sanyal, M. Chakrabarti, Ferromagnetic property of copper doped ZnO: A first-principles study. Computational Condensed Matter, 2020, vol. 23, p. e00455.

[46] C. Xia, F. Wang, and C. Hu, Theoretical and experimental studies on electronic structure and optical properties of Cu-doped ZnO. Journal of alloys and compounds, 2014, vol. 589, p. 604-608.

[47] D.Q. Fang, A. De Sarkar, R. Q. Zhang. First-principles study on the origin of ferromagnetism in n-type Cu-doped ZnO. Solid state communications, 2012, vol. 152, no 12, p. 1057-1060.

CHAPTER I

Literature review

I. 1. A review on synthesis and properties of copper doped zinc oxide thin films

I.1.1. Introduction

Hexagonal Zinc oxide (ZnO) with wurtzite structure and tetrahedrally coordinated atoms, is the most stable phase, which usually exhibits a preferred orientation along *c*-axis, a spontaneous polarization **[1]** and a mix of ionic and covalent type Zn-O bonding **[2, 3]**. At ambient experimental conditions, transparent ZnO having a high exciton binding energy (60 meV) and direct large band-gap (Eg) (3.37 eV), is a promising candidate for several applications such as gas sensor **[4, 5],** photo catalytic processes **[6, 7]**, transparent conducting electrodes **[8, 9]**, laser system **[9, 10]**, light emitting diode **[11, 12]**.

Fabrication of transparent conducting oxides (TCO) thin films with desired properties, like grain shape and size, surface morphology, band gap, transmittance, growth mode, is important task for different practical applications. Preparation conditions, synthesis method and doping process are the main factors for controlling such properties. Nontoxic and chemically stable TCO such as ZnO, have several interesting properties and they have been widely doped with transition metal elements such as copper (Cu). In addition to these advantages, the elaboration of TCO by a low cost and simple method, like sol-gel process, constitute a combination that attract the attention of several researchers to exploring the effect of the preparation conditions on the properties of Cu doped ZnO (CZO) thin films. There are many factors influencing the growth mode of CZO thin films and then their properties **[13-20]**. These factors are subdivided into three main categories, i.e., dopant element, synthesis method and appropriate environment. Reproducibility with desired properties remains to be a major problem in thin films preparation and this must be resolved before they can be used in various opto-electronics applications. Numerous techniques have been used to improve the properties of ZnO films such as spray pyrolysis **[13]**, pulsed laser deposition (PLD) **[14]**, reactive magnetron sputtering **[15]**, molecular beam epitaxy **[16],** chemical vapor deposition (CVD) **[17]**, dip coating **[20]** and spin coating **[18, 19]**.

ZnO from sol-gel solution, used as source for spin coating or dip coating, is a relatively low cost and simple process. It possesses the ability to achieve uniform CZO nanostructures at low temperatures and under very controlled and stable conditions. Transition metals doped ZnO thin films have been studied with various elements such as Silver (Ag) **[11],** Copper (Cu) **[5],** Aluminium (Al) **[8]**, Antimony (Sb) **[14]**, Cobalt (Co) **[18]** and Sodium (Na) **[20]**. Among them, Cu is extensively used to enhance the properties of ZnO host lattice **[4, 12, 21-31]** such as

transparency **[21, 32]**, ferromagnetism **[33, 34]**, crystalline quality and conductivity **[35].** It is easy to substitute Zn atom sites by Cu atom because they have approximately the same ionic size **[36]**.

Since ZnO is quite common materials for different applications, many reviews on ZnO were published for the last 10 years. However, on 'doped' and 'thin film' of ZnO are still limited. For example, Fan et al **[37]** considered the copper as p-type ZnO promising materials in addition to elements from different group and they focused only on the application of such materials; Zhu et al. **[38]** also pointed out the copper as a potential candidate, among others, to the room-temperature gas sensing of ZnO-based gas sensor; later on, Das et al. **[39]** explained the different synthesis techniques of the CuO-ZnO nanocomposite and gave effect on morphologies and also discussed its practical applications; recently, Ghanbari Shohanry et al. **[40]** reviewed the effect of adding elements categorized by seven groups, in which Cu was only illustrated as belonging to transition metals group, on the structural and optical properties and the surface morphology of the ZnO nanostructures.

To the best of our knowledge, reviews on specifically Cu dopant ZnO thin films, have not been reported yet. Its interesting to have a review devoted mainly to the properties of ZnO thin films based on the doping with a specified element, i.e. Cu and prepared by a simple and low-cost method, i.e. sol-gel. The compilation of articles will be providing a huge database to the researchers working on CZO thin films properties.

The first review aims to provide a timely overview on the development of CZO thin films by sol-gel, spin- and dip-coating as reported in literature survey from 2010 to 2020. It starts with the elaboration of materials, i.e. preparation of the solution and its deposition on a substrate, and it finishes by investigating the various properties of CZO thin films such as structural, electronic, optical, bonding, vibrational and magnetic properties as well as surface morphology and chemical composition, will be reviewed in detail.

I.1.2. Synthesis of CZO thin films

The preparation and growth technique of raw materials played an important role in controlling the properties of thin films. Different physical and chemical properties can be found for the same deposited material by various elaboration techniques, in which its properties are strongly influenced by the experimental conditions. Sol-gel process is a low cost and simple chemical synthesis methods of CZO thin films. It is also involving several parameters such as

additive,solvent, substrate, solution stirring and aging time, preheating, coating method, and annealing**.** The sol–gel process or soft chemistry is well suited for the synthesis of composite nanopowders, oxide nanoparticles and organic–inorganic materials using spin or dip routes. The key advantages of this process is the ability to achieve uniform nanostructures at low temperatures, while the introduction of impurities from byproducts of the reaction is considered its major disadvantage **[41]**.

Focussing on findings from various sources **[21, 28, 32, 35, 42-54],** parameters involved in the sol-gel process during elaboration of CZO thin films, such as source of the precursor and its concentration, type of solvent, additive species and their concentration, stirring and aging time of the sol, preheating, annealing, coating method, speed and type of the substrate, will be discussed in detail in the following section;

- **i.** Precursors: the viscosity of the sol-gel is controlled by changing the concentration of the precursors, which strongly influences the CZO film thickness **[43]**,
- **ii.** Solvents: the choice of solvent is important for CZO thin films preparation in such that precursors are soluble in the solvent medium and get easily decomposed into volatile compounds **[55]**,
- **iii.** Additives: structural properties and growth mode of CZO thin films are found to be based on the concentration of additives **[56]**,
- **iv.** Substrate: morphology and growth mode of CZO films are found to be influenced by the deposition on different kinds of substrates **[57]**,
- **v.** Heating and annealing coating: the amount of porosity can be lowered by increasing the annealing temperature, which influences the surface area of the CZO thin film **[25]**,
- **vi.** Speed and coating mode: higher angular velocities lead to thin and uniform layers on flat substrates, whereas in dip coating process, higher withdrawal speeds result in thicker films **[58]**.

The sol-gel is dropped onto a substrate, which rotates at high speed in the spin coating method. This causes the excess liquid to flow out of the substrate (**Figure 1a**). The constant rotation speed allows to cover the substrate with uniform film thickness. Evaporation then removes the solvent leaving behind a dry solid film **[59]**. Finally, the nanoparticles aggregate to agglomerates by drying and heating **[60, 61]**. In the dip-coating method, a substrate is immersed into a solution containing the sol-gel and then removed at a specific speed under very controlled and stable conditions to obtain a regular porous film (**Figure 1b**). Films deposited by this technique are usually X-ray amorphous and require a calcination step to obtain crystallization **[59, 62].** There are many works published on synthesis of CZO thin films by different routes, elaborated either by spin-coating **[28, 48, 50, 63]** or dip-coating **[32, 35, 43, 47, 49, 53].**

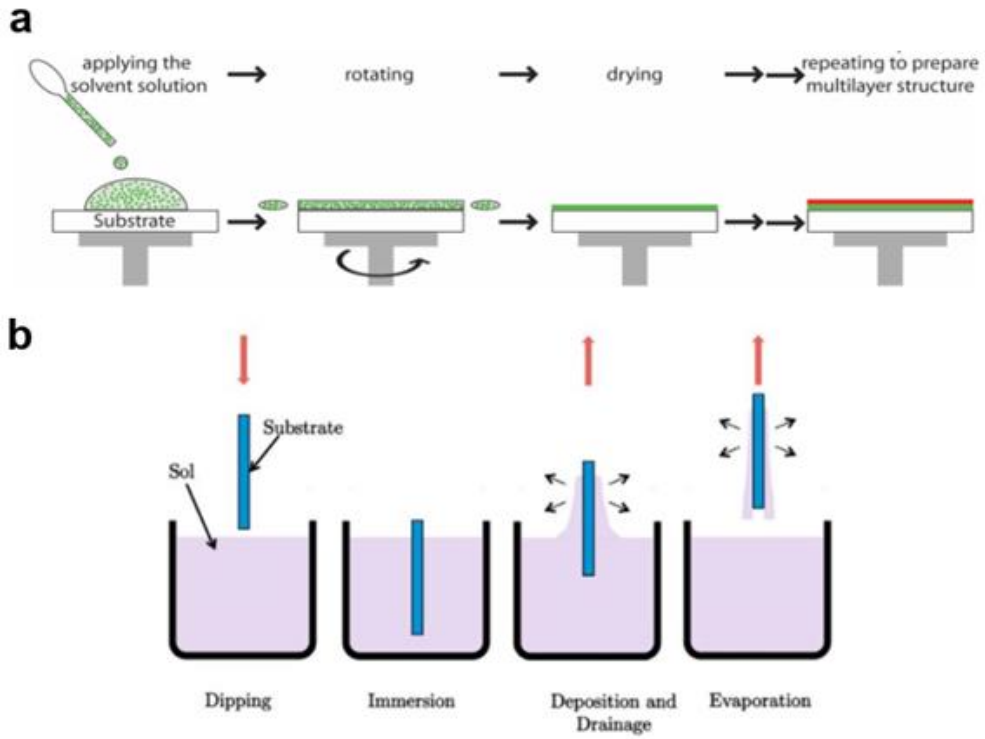

Figure I.1. Schematic diagram of **(a)** sol gel process by spin-coating route, reprinted from Ref. **[64]**, **(b)** dip-coating route, reprinted from Ref. **[65]**.

The mixing of reagents and precursors leads to the formation of a sol by either hydrolysis or polymerization reactions. The adding of polymers converts the sol to gel after thermal treatments. The gel can be deposited onto substrates and calcined to obtain the final material as thin films with different forms such as nanospheres, nanorods, nanoflakes, nanotubes, nanoribbons, nanospheres and nanofibers. The following section summarizes the various precursors, solvents and additives used in the preparation of CZO thin films and deposited onto substrates by sol-gel method **[66]**:

i. ***Zinc and copper precursors*:**

Zinc acetate dehydrate (ZAD; $Zn(CH_3COO)_2 \cdot 2H_2O$) is the most often used zinc precursors **[21, 28, 32, 42-46, 48, 50, 51, 53]** and, less favorable, the zinc acetate anhydrous (ZA; $Zn(CH_3COO)_2$) **[47, 49]** for ZnO thin films elaboration. For Cu dopant, several copper precursors have been additionally used for CZO thin films elaboration such as copper acetate (CA; $Cu(CH_3COO)_2$) **[51]**, copper nitrate (CN; $Cu(NO_3)_2$), copper nitrate tetrahydrate (CNT; $(CuNO_3)_2\,3H_2O$) **[32, 42]**, copper acetate

monohydrate (CAM; Cu $(CH_3COO)_2 \cdot H_2O$) **[53]**, copper acetate dihydrate (CAD; Cu $(CH_3COO)_2 \cdot 2H_2O$) copper acetate tetrahydrate (CAT; Cu $(CH_3COO)_2 \cdot 2H_2O$), copper nitrate hexahydrate (CNH; $CuH_{12}N_2O_{12}$) and copper chloride(CC; $CuCl_2$) **[43, 52]**.

ii. ***Solvents***

Different types of alcohols which are used as solvents, i.e. ethanol (EtOH; C_2H_5OH), methanol (MeOH; CH_3OH), 1-propanol (1-PrOH; C_3H_7OH), isopropanol [IPA; $C H_3 CH(OH)-CH_3$], 2-methoxyethanol [2-ME; $CH_3O(CH_2)_2OH$] and 2-propanol [2-PrOH; IPA; $(CH_3)_2CHOH$]. Ethanol and 2-methoxyethanol the are the most used solvents **[35, 52-54]**.

iii. ***Additives*****:**

To facilitate the complete dissolution precursors-alcoholic media and the formation of a stable sol, additives are used **[56]**. In addition to the most often used, i.e. monoethanolamine [MEA; $(HOCH_2CH_2)NH_2$], there are other additives used in the CZO thin films elaboration, namely, diethanolamine [DEA; $(HOCH_2CH_2)_2NH$], triethanolamine [TEA; $(HOCH_2CH_2)_3N$], acetic Acid (Ac. Ac.; CH_3COOH) and lactic Acid (Lactic Ac.; $CH_3CHOHCOOH$). Sometimes, it is preferable to use an additive instead of other in certain circumstance for better dissolution of the mixture. Moreover, most of the studies on CZO thin films are restricted to low Cu doping concentrations. This might be attributed to the limited solubility of Cu in ZnO host lattice or the appearance of other phase like CuO or Cu_2O lattices **[28, 67]**.

iv. ***Substrate*****:**

Preparation of CZO thin film by sol-ge are mostly deposited on glass substrate **[21, 32, 42-44, 46, 47, 49]**. Later, the heat treatment (below 100 °C) on sample still producing a clear and homogenous solution **[32, 46]**. Due the the nucleation at the film/substrate interface, two mechanisms were proposed for the orientation of the films on the glass substrates. The first is favored on smooth surfaces with the tendency of nuclei to develop a minimum free energy configuration. The second results from survival of nuclei having an energetically unstable plane parallel to the substrate [16]**.** Spin and dip coating methods also enable CZO thin film deposition on a variety of

specific types of substrate including quartz **[28, 50]**, silicon **[54]** soda lime **[51, 53]**, ITO **[45]** and borosilicate **[48]**.

v. ***Heat treatment***:

The synthesis of CZO thin film needs two heat treatment normally applied for pre-heat treatment which removes the solvent leaving behind a dry solid film, and annealing by which nanoparticles aggregate to agglomerates. Pre-heat treatment depends on additives and solvent, but it should be higher than the boiling point of them **[68]**. Some additives-solvent combinations, like monoethanolamine-2-methoxyethanol (MEA-2-ME), need a higher temperature (~250-500 °C) while a low temperature (~70-150 °C) is sufficient for some other combinations, like diethanolamine-2-propanol (DEA-2-PrOH), during evaporation and removal of the organic compounds, to grow (002) oriented films. The annealing temperature, which generally varies within a range of 400-700 °C, is an important factor governing the orientation of the crystallites and the well-crystallization of the films **[25, 68]**. The formation of CuO phase is possibly observed if the temperature acceding 700 °C, **[28].**

I.1.3. Structural properties of CZO thin films

Structural analysis by X-ray diffraction (XRD) is an analytical technique primarily used for providing information on the structure and phase of a crystal and can also confirm the incorporation of defects in each host lattice. Various parameters within the crystal such as the lattice parameters, crystallite size and number of phases, stress and strain, which were deduced from the diffraction peaks of XRD analysis, are then presented and discussed in this section. Copper (Cu) as an element of group IB will presume a valence of either 1 or 2 based on its chemical structure. Thus, cuprous oxide (Cu_2O) and cupric oxide (CuO) are the two stable types of copper oxide. The radii of Cu^+ (98 pm) and Cu^{2+} (80 pm) ions are similar to that of Zn^{2+} ion (83pm), which makes Cu a potential doping candidate for ZnO **[67]**.

XRD techniques are powerful, non-destructive tool for material characterization. It provides the first information about the structural properties of the materials, before any other characterization can be done. For thin films deposited on to the substrate, the X-ray beam enters with a small angle of incidence (0.5–2), known as grazing incidence X-ray diffraction GIXRD (**Figure 2**) **[69]**, which has been used to characterize CZO thin films **[26, 70]**. In this case, the incidence angle is fixed, and the crystallites are randomly oriented which limits the X-ray

penetration into the thin films. One of the most critical conditions for XRD analysis of samples is proper sample preparation. Since peak broadening is negligible for larger particles, XRD is generally useful for nanoscale crystallites with diameters below 200 nm. For very small particles with a diameter below 2–3 nm, the peak width cannot be reliably measured or even observed. Furthermore, since the Scherrer equation ignores internal particle strain and defects, which can cause peak broadening, the particle size determined by XRD should not be regarded as absolute measure of crystallite size **[71].**

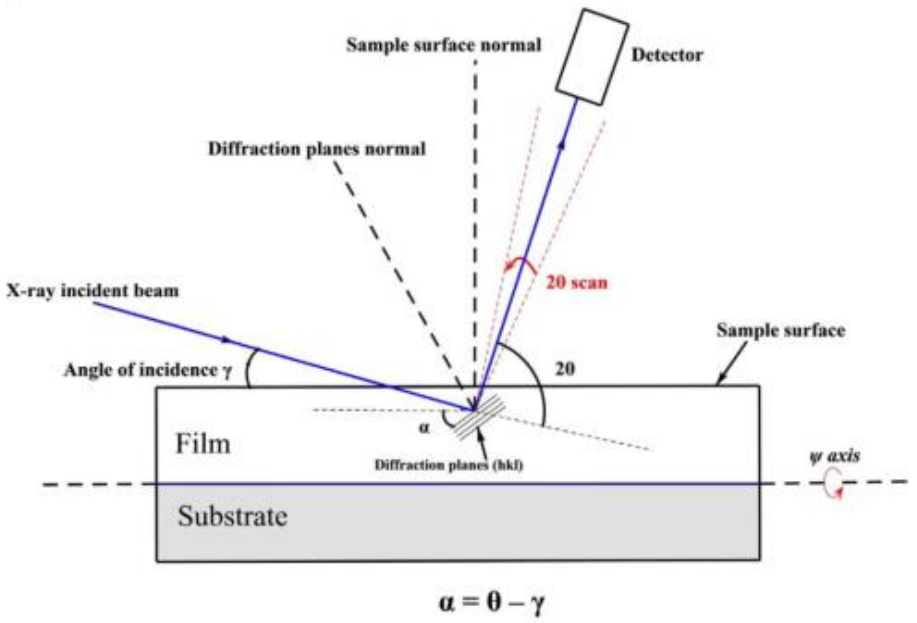

Figure I.2. Schematic diagram of grazing incidence X-ray diffractometry **[69].**

XRD spectra of pure ZnO thin films generally show a peak at the Bragg angle of ~34.5°, which is assigned to (002) plane **[54, 72]**. Moreover, (100) peak at ~31.9° and (101) peak at ~36.4° can also be observed in some cases **[28, 73]**. The incorporation of Cu with lower concentration into ZnO host lattice does not exhibit any additional secondary phase (CuO or CuO_2) and conserves its wurtzite structure. This is due to incorporation of Cu into ZnO host lattice where the ionic radius of Cu^{2+}(0.73A˚) is close to that of Zn^{2+} (0.74A˚)**[28]**. In such circumstances, CZO prefers (002) plane as a dominant orientation among several planes corresponding to (100), (002), (101), (102), (110), (103) and (112) peak of the ZnO presented in XRD spectra (P63mc space group; JCPDS card 36-1451) **[21, 67, 74]**. This asserts that CZO thin films possess a polycrystalline nature. However, CuO phase can appear by increasing content of Cu dopant, **3** mol.% **[75]** and 10 at.% **[28]**, with emerging a (111) new peak. The

intensity of (002) peak is generally reduced, especially at high Cu concentration, leading to the degradation of the (002) preferential orientation of CZO thin films with the enhancement ofother orientations like (100) and (101) **[27, 28, 42, 45, 46, 76]**. This was affected to heterogeneous nucleation process **[42]**.

The variation occurred in intensity and position of different peaks of XRD pattern by Cu doping were presented in the literature as a function of diffraction angle for ZnO and CZO samples **[28, 54, 72, 73]**. A slight shift in the peak position towards higher diffraction angles is obtained with the increase of Cu concentration. The observed shift is attributed to the substitution of Cu atom at Zn atom site where the ionic size of Cu^{2+} is slightly smaller than Zn^{2+} **[49]**. This can also explain the change occurred in other related parameters, such as lattice constants, crystallite size and strain and stress **[28]**. On the other hand, the diffraction peaks of XRD analysis can give other information within crystal such as the lattice parameters, crystallite size and number of phases, and that is through famous formulas and appearing and/or disappearing of some peaks in the XRD pattern of CZO thin films **[24]**.

The increasing level of Cu content can influence the lattice strain **[22, 27, 28, 77]**. The strain variation is explained by the presence of excess of Cu dopants at grain boundaries **[27, 28].** It is also ascribed to the intrinsic stress due to the impurities and defects in the host lattice **[22, 77]**.

The lattice constants $a = b$ and c can be usually calculated from XRD patterns for pure and CZO thin films**.** It is observed that lattice constants are slightly affected by Cu content. This is mainly due to the strain induced by the incorporation of Cu into ZnO host lattice, which leads to the change in bond angle along c axis between Zn-O planes (120° for hexagonal wurtzite ZnO) **[43]** where the ionic radius of Cu^{2+} (0.73A˚) is slightly smaller than that of Zn^{2+} (0.74A˚) **[24, 78]**.

It is also found that the increasing of Cu doping influences the crystallite size (D). The crystallite size presents an increase with increasing Cu content, especially at lower thickness **[28, 31]**, while an increase followed by a decrease is marked at higher thickness **[26, 78, 79]**. However, a decrease in the crystallite size value is also noticed in the literature **[24, 43, 51]**.

In addition, the preferential orientation and its intensity of CZO films for a given concentration depend on the deposition method **[68, 80]**. Moreover, the increasing level of Cu concentration plays an important role in the change of the preferential orientation from one

direction to another, where the growth mode of grains translates from c-axis growth perpendicular to the substrate to lateral one **[24, 72]**.

The thicknesses of CZO thin films, elaborated by different methods at various experimental conditions were measured by different techniques such as cross sectional SEM 2D-image, Profilometer, envelope method based on transmittance measurement. They exhibit both an increase **[4, 23, 27, 31]** and a decrease **[24, 49, 81]** in the thickness with increasing Cu content. This may be attributted to the growth mode of grains, perpendicular or lateral, which is affected by Cu incorporation as well as the experimental conditions such as substrate type and deposition mode. However, slight variation of thickness is also noticed in the literature, especially at lower Cu concentrations **[26, 35, 51, 52, 72, 78]**.

The shift of the main peaks position and their intensity from the XRD analysis of CZO thin films were intensively investigated for lower **[4, 26, 27, 31, 42, 43, 49, 53, 73]** and somewhat higher **[46, 52, 54, 72, 78, 82, 83]** concentrations. Most of reports exhibited a shift of main peak (002) position towards higher diffraction angle **(2θ)** with the increase of Cu doping concentration whereas few reports **[26, 43, 45, 73, 78]** indicated a shifting towards lower diffraction angle. Moreover, some other reports **[52, 74]** noticed the moving of the (002) peak towards the lower angle followed by a shift towards the higher angle with the increase of Cu doping concentration. This behaviour was explained by taking into account that ZnO host lattice might be doped by either Cu^{+2}, with an ionic radius (0.73 A°) is close to that of Zn^{+2} (0.74A°), or by Cu^{+1} with a slightly larger ionic radius (0.77 A°), which were identified experimentally in the ZnO by XPS spectroscopy **[49]**.

Summary of the main findings from previously cited works, can then be drown as follow,

- **i.** Lower Cu content and preferential orientation: the incorporation of Cu at lower Cu concentration into ZnO host lattice is confirmed by conserving of the wurtzite structure and the usual preferential orientation (002) plane,
- **ii.** Growth mode and increasing Cu content: the growth mode generally translates from c-axis growth to lateral one with the increase of Cu dopant level,
- **iii.** Secondary phase and higher Cu content: the secondary phase, e.g. Cu_2O or CuO, at higher Cu concentration is usually confirmed by the degradation of the (002) preferential orientation, emerging a new peaks in XRD pattern such as (111) peak, and the enhancement of other orientations, such as (100) and (101),

iv. Peak position with Cu dopant: the slight shift in the peak position towards higher diffraction angles is one of the factors indicating the incorporation of Cu dopant in ZnO host lattice and substituting the Zn atoms,

v. Influence of Cu^{+2} or Cu^{+1} ions on the shift of peak: the shift of the (002) peak towards the higher or lower angle with the increase of Cu content may be explained by Cu^{+2} or Cu^{+1} ions doping.

I.1.4. Morphological properties of CZO thin films

To investigate the smallest of internal thin films, results issued from Atomic Force Microscopy (AFM) and Scanning Electron Microscopy (SEM) are shown. The micrographs give further confirmation to results issued from XRD patterns due to the ability to reveal the grain size and the surface roughness of CZO thin films. In the following tow sections, we will summarize the various factors linked to the preparation method and adding materials that influencing the morphological parameters of CZO thin films such as particles agglomeration, grain size and shape, growth mode and roughness.

I.1.4.1. AFM morphology of the CZO thin films

Atomic Force Microscopy (AFM) is based on measuring the forces between a given sample surface and a sharp tip which moves across it and generates three or two dimensional topographic map of the surface (**Figure 3**) **[84].** Depending on the cantilever oscillation, the AFM can be operated in three common modes: contact, non-contact, and tapping. For soft samples, non-contact mode is preferable over contact mode, in which the AFM measurement does not suffer from tip or sample degradation effects. AFM does not request any special treatment during CZO sample preparation such as its coating with a conducting film and vacuum **[85]**.

AFM analysis have been reported in the literature on CZO thin films at various Cu doping levels expressed as atomic percent (limited to low x **[32, 42, 52, 72]** and extended to higher *x* **[23, 26, 28, 43, 78]),** weight percent **[21, 22]** or molar percent **[44, 83]**. Then, two and three-dimensional AFM images **[43, 49]** as well as morphological parameters, such roughness and grain size, are usually extracted from the AFM analysis of the samples. An island-like growth was observed for pure ZnO films which were transformed to a dense columnar surfaces

for CZO films with Cu content of 3 and 5 at.% **[78]**. Pure and CZO thin films with Cu concentration of 0.05 and 0.1 mol%, exhibited a granular morphology for undoped films and larger grains densely packed for Cu doped films **[83]**. Other surface morphologies from previous works are also tabulated in sake of comparison and to give more insights on the influence of various preparation parameters on surface morphology. Some works noticed the increase in the surface roughness with increasing Cu content **[28, 43]** while some others marked its increase at lower *x* followed by a decrease at higher *x* **[23, 26, 78]**. However, a decrease in the surface roughness is also marked in the literature **[21]**. Therefore, it has been demonstrated that the particle shape and size as well as surface morphology were strongly dependent on the synthesis condition as well as on the range of Cu concentration.

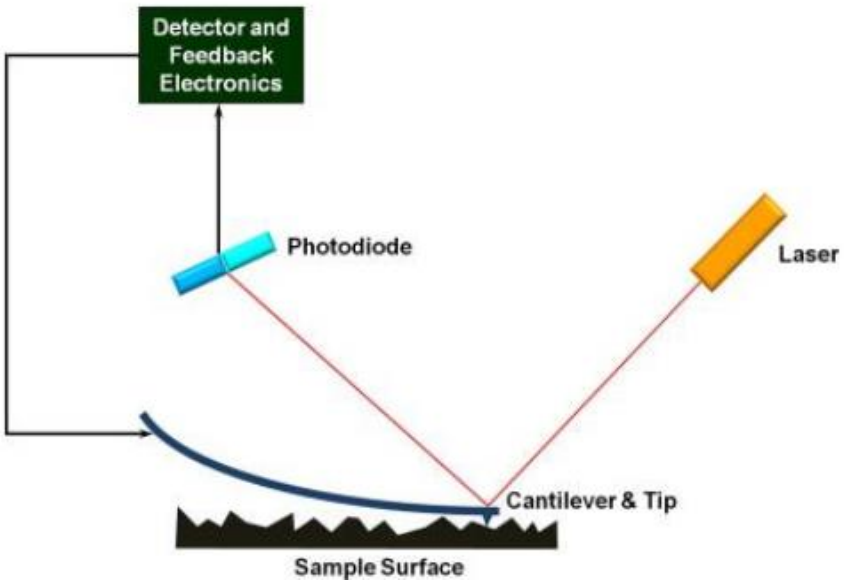

Figure I.3. Schematic diagram of a typical AFM instrument **[84].**

I.1.4.2. SEM morphology of the CZO thin films

Essential information about the surface morphology of the sample can be produced from Scanning Electron Microscopy (SEM) analysis**.** The electron beam of SEM interacts with atoms at different depths within the sample and emits X-rays, backscattered electrons, secondary electrons, and Auger electrons. SEM makes use of the backscattered and the secondary electrons and produces High-resolution images (**Figure 4)**. The obstacle created by the vaporized water in the vacuum, obscures the clarity of the image. So, removal of water is essential **[86]**. Coating of non-conducting or poorly conducting thin films by conductive layer of metal (Typical range of 2–20 nm) is required in SEM to enable or improve the imaging. This

process reduces thermal damage and charging and improves the secondary electron emission **[86, 87]**.

Many reports showed SEM images for CZO films elaborated by different process at various experimental conditions **[22, 28, 32, 42, 43, 83]**. FE-SEM images of CZO thin films with Cu content of 1, 3 and 4 wt.% were shown **[79].** It was observed irregular sized and not dense structures for *x*=1 wt.%, granular structures with compact surface for *x*=3 wt.%, and the decreasing of grain size with lesser overgrown particles for *x*=4 wt.%. Also, the films tend to exhibit better columnar growth perpendicular to the surface for higher Cu concentration.

In their study on the effect of Cu doping, Osali et al. **[22]** presented, via calcination, the change from nanofibres to nanoparticles for CZO thin films at various concentration (*x*= 0, 2, 4, 6 wt.%), which agglomerate with increasing level of Cu dopant. CZO thin films with $0 \leq x \leq 8.5$ at.%) **[27]** exhibited homogeneous grains for low Cu concentration (*x*),which were assembled to form broccoli-like clusters for high *x*. Recent study on CZO thin films at various concentrations of 2, 5, 10, 15 and 20 at.% **[24]** indicated that AFM images present a mixer of spheroid-like and rod-like particles for Cu content < 15 at.% and a cylindrical shape and size for Cu content ≥15 at.%. Moreover, SEM images of CZO thin films with *x* in the range 0–4 at.% exhibited multi-grained with uniform growth and showed no significant variation in surface morphology with increasing of Cu content **[12].**

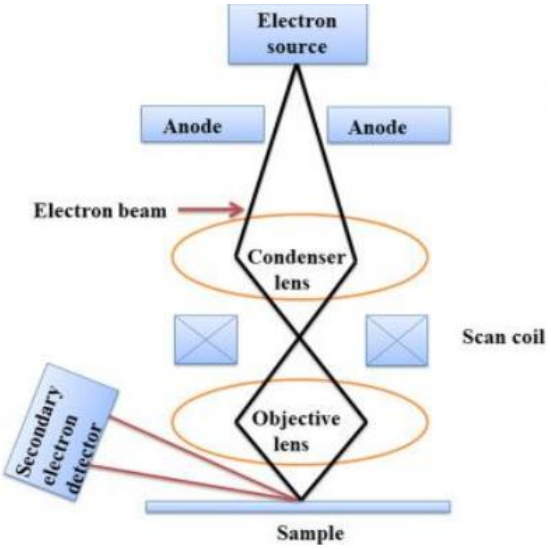

Figure I.4. Schematic diagram of Scanning Electron Microscopy (SEM) **[86]**.

From findings on morphology analysis either by AFM or by SEM microscopy, one can draw the following remarks,

i. Cu doping and particle form: the particle shape and size is more influenced by the increasing level of Cu content,
ii. Cu doping and grains density: incorporating of Cu defect in the ZnO host lattice generally increased the grains density,
iii. Cu doping and roughness: Cu doping can help in producing a smooth surface,
iv. Cu doping and internal structure: high level of Cu concentration can lead to an agglomeration of nanoparticles in the CZO thin films.

I.1.5. Electronic and optical properties of CZO thin films

I.1.5.1. Transmittance and band gap energy

Analysis by Ultraviolet-Visible (UV-Vis) spectroscopy is an important tool used to characterize materials by light in ultraviolet (UV: ~300 -400 nm), visible (Vis: ~400-750 nm), and near infrared ranges (NIR: ~750-3200 nm). The measured spectra of CZO thin films deposited on transparent substrates may be received as transmittance, absorbance or reflectance of radiation and quantitative and qualitative information are then provided. For CZO thin films, the band gap absorption was found to vary in the ultraviolet region while the main optical parameter, i.e. static refractive index, was estimated from the interference fringes of the optical transmission spectrum in the visible and ultraviolet ranges.

Ellipsometry, with non-normal incidence of light, and the spectral reflectance, with the incident light perpendicular to the film surface, are two most common optical measurement types. This latter is generally much simpler and suitable for CZO transparent thin films. UV-Vis spectroscopy has been commonly used as suitable method to characterize the optical and electronic properties of CZO thin films deposited on transparent substrates **[21, 26, 35, 72]** from measurement of transmittance and/or reflectance. Optical energy gap E_g can then be extracted using the well-known Tauc relationship **[88]**. The dispersive refractive index spectrum in photon energy range less than E_g are analyzed by Wemple and DiDomenico according to the single-efiective-oscillator model **[89]**. For basic UV-vis characterization, the CZO thin film sample is placed accordingly with a double-beam UV-Vis spectrophotometer (**Figure 5**) **[90]**. The reference cell often contains the substrate (utilized as a reference) and the other cell

contains the sample (CZO thin film). The spectrum of CZO thin film is then obtained by subtracting the absorbance of the substrate.

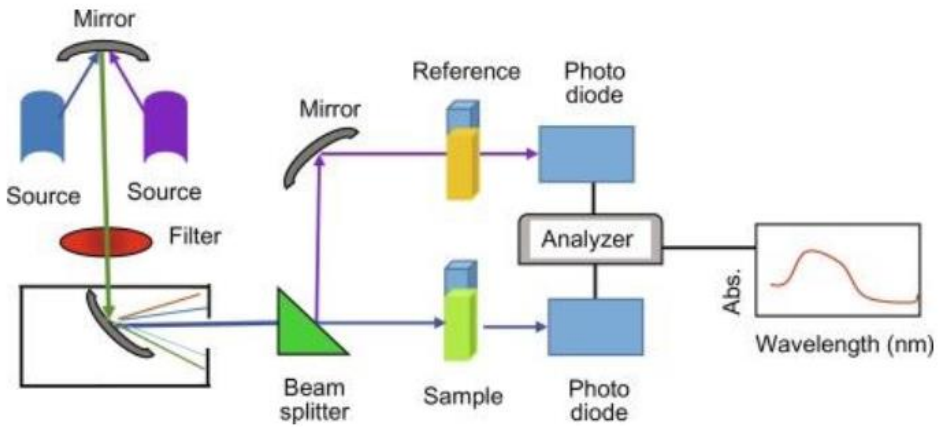

Figure I.5. A schematic diagram of a double-beam UV-Vis spectrophotometer **[90]**.

CZO thin films generally exhibited high optical transmittance in the higher wavelength region ($\lambda \geq 400$ nm) **[21, 26, 35, 72]**. The shift in the absorption edge in the transmittance spectra of CZO thin films towards higher wavelength region are observed with increasing of Cu concentration. For a uniform film, the interference effects give rise to oscillating curves (interference fringes), which are used to estimate the optical parameters, such as refractive index, and the thickness of the films. These interference fringes disappear in the region of strong absorption ($\lambda \leq 400$ nm) and they are not usually observed for films with very low thickness.

The average transmittance in the visible region was found to be influenced by increasing Cu doping **[4, 12, 21-24, 26-28, 32, 35, 43-49, 52-54, 72-74, 78, 81-83]**. Some reports found that average transmittance is increased with increasing Cu content **[21, 32, 48, 49, 72]**, whereas some others recorded that CZO exhibited a low average optical transmittance in the visible region when the concentration of Cu was increased **[22-24, 26, 43, 53, 74, 78, 81, 83]**. To justify these trends, various causes have been given. The slight improvement in the average transmittance for CZO thin films with Cu content of 0.1, 0.3, 0.5, 0.7 and 1 mol% **[49]**, was attributed to the optical scattering. This scattering was decreased by the reducing in the density of grain boundary, which stems from the increased grain size. In other work for pure and CZO thin films with Cu content of 0.05 and 0.1 mol% **[83],** authors explained the slight decrease with Cu content by the creation of oxygen vacancies and scattering at the grain boundaries.

Recent report also indicated that the rough surface scattering or/and grain boundary scattering are behind that trend **[52].**

The band gap (Eg) values of the CZO thin films at different Cu contents was obtained from measured transmittance and/or absorbance **[4, 12, 21-24, 26-28, 32, 35, 43-49, 52-54, 72-74, 78, 81-83].** The observed shift in the absorption edge in the transmittance spectra towards higher wavelength region suggests the shrinking of the band gap energy**.** The broadening of the band gap energy was noticed in few reports **[21, 28, 48, 49]**. To explain the change of the band gap, Xu et al. [52] proposed the Bustan-Moss effect, where Cu^{+1} ion forms an acceptor level in the forbidden band of the ZnO lattice, and then generates a hole and reduces the number of charge carrier concentration by trapping electrons from the conduction band. Similarly, It was indicated for CZO thin films at different Cu content (x = 2, 5, 10, 15 and 20 at%) [24] that when Zn site is occupied by a Cu atom, the strong *d-p* coupling between Cu and O atoms and the impurity bands created by Cu *3d* orbital give rise to a positive (energy of the valence band) and a negative (energy of conduction band) corrections. In the theoretical point of view, the band gap narrowing in CZO material [91] has been interpreted by the shift of conduction band towards the low-energy level and the shift of valence band toward the high-energy level.

Finally, it is worth noting to provide the reader by a summary of the main findings on the transmittance and bandgap for CZO thin films,

a) Shift in absorption edge: all prepared films at different Cu contents presented a sharp falling of absorption edge, which shifts towards higher or lower wavelength region following to shrinking or broadening of bandgap,

b) - Average transmittance trend: the decrease of the average transmittance by Cu doping is due to the optical scattering decreased by the reducing in the density of grain boundary,

c) Shrinking of bandgap: the strong *d-p* coupling between Cu and O atoms is usually proposed to explain the shrinking of bandgap.

I.1.5.2. Photoluminescence (PL) spectra

Photoluminescence (PL) spectra is necessary to explore the levels of defects and their amount in ZnO thin films. The near-band-edge (NBE) emission, generally located within wavelength range of 375-385 nm and, is due to recombination of free excitons between conduction band (CB) and valence band (VB). The PL spectra of CZO thin films display another series of emission peaks. These emissions occurred via transitions among various levels; VB, CB and different created levels of defects such as zinc vacancies (V_{Zn}), zinc antisites (Zn_O), oxygen interstitial (O_i) oxygen vacancies (V_O), zinc interstitials (Zn_i) and oxygen

antisites (O_{Zn}). Photoluminescence spectrometers typically use excitation source in the broad wavelength range from the UV to near-IR region (xenon lamps are usually used). The emitted spectra are collected at either a right angle or front face relative to the incident beam. The photoluminescence technique has been significantly improved, due to the availability of lasers and more advanced detectors, and allows the PL spectra to be measured at various temperatures **[92]**. For CZO thin films, the excited electron in the conduction band relaxes quickly to the band edge and then recombines with the hole, to trapping levels that are created by Cu dopant or defects (V_{Zn}, O_i, V_O, Zn_i, O_{Zn}, Zn_O) and lie in the forbidden band or to another electron or hole **[22, 23, 52, 92]**.

Five peaks were usually recorded within the visible range **[12, 22, 82].** The first peak usually corresponds to NBE emission. Additional peak is appeared for high Cu concentration **[12]**. Some of the appeared peaks are sometimes suppressed by increasing of Cu content **[22],** and their intensity showed a diminishing with Cu doping**.** This trend was attributed to Cu centres in ZnO film which act as traps to the excited electrons **[82].** In a similar case it was observed four peaks for ZnO films while another green emission was recorded only for CZO thin films **[32].** Some other reports observed only tow peaks **[23, 73],** in which it was assumed that Cu as a p-type dopant introduces a deep acceptor level near the conduction band **[23]**. Similarly, tow pronounced peaks were observed for CZO thin films (Cu content of 0-5 at.%) **[73]**. The first peak, located in the visible region, generally exhibited a decrease in its intensity with Cu doping, which was attributed to the decrease in the concentration of defects. The second peak, located in the UV region, presented an increase when Cu content increased from 0.5 to 1 at.%, followed by a decrease for Cu content above 1 at.%. Moreover, for CZO thin films at Cu content of 0.25, 0.98 and 1.06 wt.%, it was recorded only one main emission peak with a slight variation in its intensity **[74].**

Some reports proposed a defect's energy level diagram for CZO thin films from results of PL spectrum (**Figure 6) [22, 23, 52].** Transitions between various levels lead to the formation of different peaks in the PL spectra. It was observed from PL spectra for CZO thin films at Cu content of 0, 2, 4, and 6 wt.% **[22]** that the green emission (at 530 nm) was suppressed due to the doping of Cu into ZnO lattice and reducing of oxygen vacancy (V_o), the blue emission was mainly influenced by the created zinc vacancy (V_{Zn}) and the improvement of PL spectrum for high *x* was due to the occupation of Zn^{+2} sites by Cu^{+2} ions. Report also noticed that Cu doping isn't the origin of any PL emission and only the intensity of PL emission is changed by its incorporation. In recent work on ZnO thin films at various doping Cu concentration of 0, 5.1,

6.2 and 7.5 at%, authors pointed out that Cu introduces a deep acceptor level below the conduction band and the strong violet emission observed for high *x* signifies the variation in V_{Zn} density **[23]**. Besides, the adjusting of electrons to the CB and trapping of holes at V_O were proposed to explain the green emission observed in PL spectrum for CZO thin films doped Cu concentration of 1 at.% **[32].**

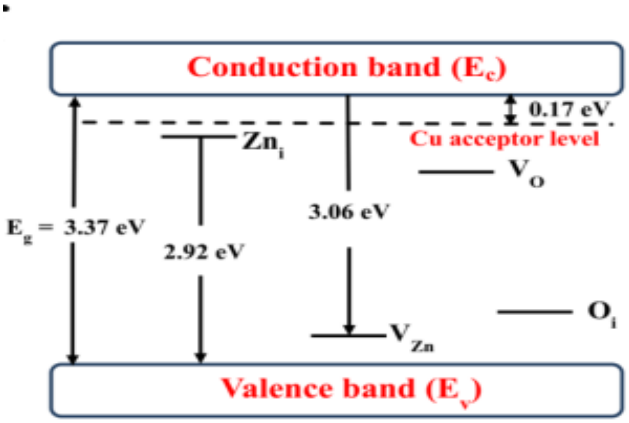

Figure I.6. Defect energy level diagram of CZO thin films at Cu content of 0, 5.1, 6.2 and 7.5 at.% **[23]**.

A comprehensive review on PL spectra and defect energy level diagram can conduct us to draw the following notes,

i. Peaks and allowed transitions: the number of emission peaks appeared in the PL spectra of CZO thin films depends on the different allowed transitions among various levels of VB, CB and created defects (V_O, V_{Zn}, Cu_{Zn}–Z_{ni}),

ii. Peaks position: the position of the appeared peaks in the PL spectra of CZO thin films, is strongly affected by the concentration of the defects which in their turn depend on the preparation conditions as well as on the Cu dopant,

iii. Additional peaks: the increasing level of Cu doping into ZnO lattice can lead to the suppression or appearing of certain peaks in the PL spectra,

iv. Defects and peak intensity: the amount of defects, acting as traps to the excited electrons, can influence the peak intensity.

I.1.5.3. Raman spectroscopic studies on CZO thin films

A Raman spectrum contains a number of peaks, including the wavelength position and intensity of the scattered light (Typical Raman spectrum covers a range of 4000–10 cm^{-1}).

Many works have been done on CZO thin films by using Raman spectroscopy to explorer the specific group of chemical bonds attributed to different vibrational modes. These modes,

corresponding to various peaks, are related to the various type of ions and defects involved in the ZnO host lattice such as Zn^{2+}, O^{-2} ions, Cu dopant, V_O and Zn_i defects. In the theoretical point of view, the ZnO wurtzite structure (C_{6v}^4 symmetry) has 12 phonon branches with the irreducible representations $\Gamma = 2A_1 + 2B_1 + 2E_1 + 2E_2$, which are divided into 9 optical and 3 acoustic branches. The A_1 and E_1 active modes are polar and the B_1 (inactive) and E_2 (active) are defined non-polar modes. Among these branches, there are 4 Raman active phonons at the centre of the Brillouin zone. Cu^{2+} ions can replace Zn^{2+} ions, generate minimal distortion in the host lattice, and modify the absorption spectrum**.** The Raman spectra leads then to estimate the degree of structural disorder manifesting in the E_2 mode.

Raman spectroscopy is generally based on measuring the shift in the energy of the scattered photon after striking the sample. Various peaks are appeared in Raman spectra corresponding to different vibrational theoretical modes (**Figure 7**) **[93],** some of them for characteristic of ZnO wurtzite structure **[94]**. The appearing or suppression of other peaks is an indicator of presence of doping elements or formation of another phase. To explore the induced change caused by the incorporation of Cu atoms, Raman spectra of CZO films at various Cu content (*x*), are reported from different sources in various ranges of wave number; $0 \leq x \leq 8.5$ at.% (200–800 cm^{-1}) **[27]**, *x*= 3, 7 and 10 at.% (150–900 cm^{-1}) **[28]**, *x*= 0, 1, 2 and 3 at.% (200–800 cm^{-1}) **[4]**, *x*= 0.5, 1, 3 and 5 at.% (300–2000 cm^{-1}) **[33],** *x*= 0, 1, 3 and 5 at.% (100–800 cm^{-1}) **[95]**, x=0, 0.5, 1, 2 and 5 at.% (200–800 cm^{-1}) **[73]**. The reason for this diversity of the studying range for the wave number is related to the region in which a given vibrational mode has appeared, i.e., the vibrational modes linked to the formation of a new phase, the characteristic vibrational modes of ZnO, the vibrational modes related to the presence of impurities.

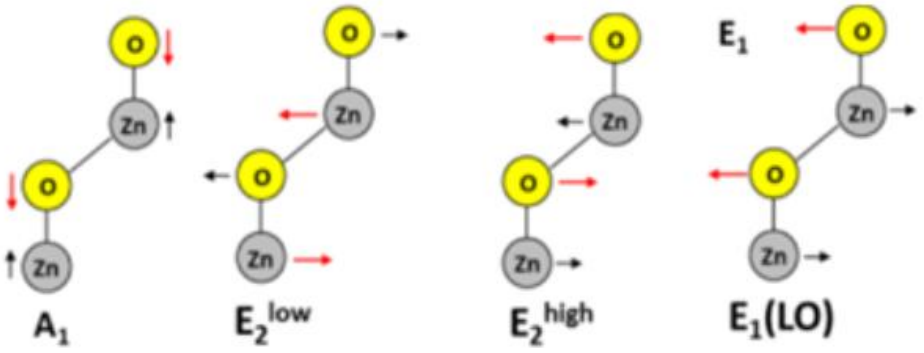

Figure I.7. Raman active modes with their corresponding vibrations of the ions in the ZnO wurtzite structure: A_1 and E_1 (LO) are polar modes, E_{2L} **and** E_{2H} (non-polar modes) are dominated by the vibrations of the Zn and O sub-lattices, respectively **[93]**.

Raman spectra of CZO thin films at various content of 0.5, 1, 3 and 5 at.% **[33]** exhibited four Raman peaks at 433, 574, 1153, and 1729 cm^{-1}, which were affected to the E_{2H} mode and the first-order to third-order A_1*(LO)* modes of ZnO, respectively. Report noticed that no other peak was observed by Cu doping, which indicated that Cu ions were dissolved into ZnO host lattice. The intensity of E_{2H} mode was found to be decreased, while the A_1*(LO)* mode presented a broadening. This was attributed to V_O defects.

For CZO thin films, prepared by sol-gel spin coating method and deposited on Si substrate **[28]**, the Raman spectra displayed various peaks at 438, 380, 333 cm^{-1}, which were assigned by the authors to vibrational modes E_{2H}, A_1(TO) and $2E_2$(M), respectively, in addition to other modes of Si substrate (520 cm^{-1}). It was also noticed the suppression of E_{2H}, attributed to oxygen vacancies, and the appearing of another mode at ~634 cm^{-1}, attributed to CuO phase formation, for higher doping of Cu.

Raman analysis on CZO thin films at various Cu content (x=0, 0.5, 1, 2 and 5 at.%) **[73]** revealed five peaks for the Raman spectra located at 336, 387, 438, 541 and 580 cm^{-1}, which were affected to the second order acoustic mode and the vibration A_1 (TO) mode, the E_{2H} (high) mode, the A_1 (LO) mode, and the E_1 (LO) mode, respectively. It was also observed the decreasing of the intensity of the E_{2H} mode and the vanishing of the A_1 (LO) vibration peak by Cu doping. This latter was affected to the formation of Zn_i states and V_O.

Higher oxygen vacancies in the CZO film films at various Cu contents of 0, 1, 2 and 3 at.% **[4]** caused a small shifting in the position of various peaks observed in the Raman spectra with increasing level of Cu doping in the wave number range of 200–800 cm^{-1}. In other study

on CZO thin films in the region of 200–800 cm^{-1} with Cu content ranging from 0 to 8.5 at.% **[27],** it was indicated that all films showed tow peaks located at 344 cm^{-1} (E_{2H}-E_{2L} mode) and

at 596 cm^{-1} (E_1(LO) mode). The E_1(LO) peak has found to be intensified and the position of both E_1(LO) and E_{2H}-E_{2L} exhibited a blue-shift with increasing amount of V_O with Cu doping. This findings are found to be in agreement with other reports **[4, 28, 33, 73].**

CZO thin films at various Cu contents (0, 1, 3 and 5 at.%) were prepared by the sol-gel doctor blade technique **[95].** Four peaks located at 97.4 cm^{-1} (E_{2L} mode), 340 cm^{-1} (E_{2H}-E_{2L} mode) and 437 and 581 cm^{-1} (A_1 mode) were observed, they are characteristic of ZnO wurtzite structure. It was also observed the widening and decreasing of E_{2L} peak (~99 cm^{-1}) and E_{2H} peak (~437 cm^{-1}) in the case of CZO thin films, which were attributed to the formation of nancomposites due to the incorporation of Cu^{2+} into the host lattice. The formation of a ZnO-CuO heterojunction was also assigned to two other peaks located at 298 (A_{1g} mode) and 614 cm^{-1} (B_{2g} mode).

As a summary for this part, some notes can be issued from the overview on the Raman spectra,

- **i.** Phase shift: the incorporation of Cu dopant in the ZnO host lattice can lead to the formation of new phase (CuO) and then the appearing of its corresponding modes (A_{1g} and B_{2g}),
- **ii.** Suppression of modes: the increasing level of Cu doping can lead to the decreasing amount of V_O and then to the suppression of a certain modes (E_{2L} and E_{2H} peaks),
- **iii.** Characteristic peaks: four peaks corresponding to E_{2L}, E_{2H}-E_{2L} and A_1 vibrational modes, are characteristic of ZnO wurtzite structure,
- **iv.** Additional peaks: the number of peaks observed in Raman spectra depends on the elemental composition of the CZO films as well as the substrate.

I.1.5.4. Fourier transform infrared spectroscopy on CZO thin films

The Fourier transform infrared spectroscopy (FTIR) spectroscopy is usually used among other techniques such as Raman spectroscopy to obtaining information about chemical bonding in CZO thin films and identifying their elemental constituents,. This is done by exploring the presence or absence of the various bands in FTIR spectra. The different modes of a given chemical group are then expected in specific regions of vibrational frequencies or band (400-

4000 cm^{-1}), which depend on the chemical bonds involved in various type of atoms. Many works have been done on CZO nanopowders by using FTIR spectroscopy, but those of CZO thin films was few. This is attributed to the limited solubility of Cu in ZnO host

lattice, usually did not exceed 10 at. %, or the formation of other phase such as CuO lattice. Various experimental methods are available in infrared spectrophotometry (vibrational spectroscopy), and their appropriate use depends on the sample and the analytical objective. This is done by either transmission or reflection in the mid-infrared region (400-4000 cm^{-1}). The traditional transmission FTIR spectroscopy has been commonly used as the easiest method to analyze CZO thin films deposited on transparent substrates **[4, 46, 83, 96]**. The transparency of substrates makes the transversal or longitudinal optical vibrational modes clearly observed. The attenuated total reflection Fourier transform infrared (ATR FTIR) spectroscopy is another modern technique used to measure the infrared spectra of thick films. In addition to its depth profiling within a thickness of about 1 μm, the ATR FTIR technique takes advantages of reflection at interface **[97]**. This spectroscopy has been used to localize the amount of Cu on the surface of stearate-ZnO particles. Besides, diffuse reflectance infrared Fourier transform spectroscopy (DRIFTS) has also been used for the analysis of CZO but only in the fine powder form **[98].**

CZO thin films with Cu contents of 0, 0.05 and 0.1 mol% **[83]** recorded various bands for FTIR spectra. The absorption band (400-1200 cm^{-1}), or the first band, was attributed to the oxygen-metal linkages. In this band an absorption peak was observed at 535 cm^{-1} only for pure ZnO and a second peak at 1072 cm^{-1} was assigned to Si-O-Si bonds due to the silicon wafer. Report also indicated that the vibrations of the organic residuals and the water incorporation caused the second band (1200-4000 cm^{-1}). The absorption peak of CZO thin films, corresponding to Zn-O bond, was observed at 675 cm^{-1} and other weak peak, attributed to stretching vibration of ZnO, was located at 800 cm^{-1}.

Report on pure and CZO thin films with Cu content of 8 at.% **[46]**, exhibited five pronounced bands which were attributed to various vibration modes; 1740 cm^{-1} (H-O-H bending), 1371 cm^{-1} (asymmetric vibration of CH_2), 1210 cm^{-1} (O-H stretching vibration of H_2O), and 931 and 825 cm^{-1} (microstructural change induced by the incorporation of Cu into ZnO host lattice). In a later work for CZO thin films with Cu content of 1, 2 and 3 mol.% **[96],** FTIR spectra showed different peaks located at various positions; 2925 and 2830 cm^{-1} (C-H bond stretching and bending), 1573 and 1403 cm^{-1}, (symmetrical and asymmetrical stretching of carboxylic acetate), and two other peaks at 1050 and 780 cm^{-1}, which are specific to ZnO

vibrations. In addition to these peaks, the formation of rod shape was assigned to stretch of bandat 666 cm^{-1}. It was also noticed that the absence of a peak corresponding to O-H bond vibration is an indicator of non existence of absorbed water on the surface.

FTIR spectra of pure and CZO thin films showed several peaks **[99]**. Some of these peaks (490, 526, 664, 840, 1009 and 2368 cm^{-1}) were characteristic of various vibrations of bonds in the substrate (DD3-clay) and molecules absorbed by the surface (1649 cm^{-1}). Two peaks located at 420 and 480 cm^{-1} were assigned to Zn-O vibration bond in ZnO thin films. It was also observed tow other peaks (470 and 508 cm^{-1}) in the case of CZO thin films, which were attributed to Cu-O vibration. Report indicated that the using of other substrate (DD3-clay+ 38% of ZrO_2) did not change significantly the FTIR spectra. In this case, a slight difference was observed within confined area (400 and 1250 cm^{-1}) compared to the first case (DD3-clay).

CZO thin films at various Cu contents (1, 2 and 3 at.%) were recently prepared by the sol-gel spin coating technique **[4]**, it was observed various peaks, which were attributed to the vibration of different bonds. The peak at 3444 cm^{-1} (stretching of O-H vibration) indicated the presence of water molecules. The peak ranged from 2952 to 2856 cm^{-1} was due to stretching of C-H asymmetric. The presence of CO_2 molecules (peak at around 2342 cm^{-1}) and residual organic impurities (peak at around 1533 cm^{-1}) was also revealed. The band around 904-469 cm^{-1} (stretching of Zn-O bond) was due to the substitution of Cu into the ZnO host lattice. The change in the bond length caused by the substitutional doping of Cu with Zn was assigned to the small shift in the position of absorption peak.

All these findings on FTIR spectra of CZO thin films with various Cu contents confirm the following notes,

i. Significant peaks: two peaks in the medium band of vibrational frequencies (~ 904-469 cm^{-1}) are assigned to the incorporation of Cu in ZnO host lattice whose Zn-O vibration bond are usually described by other two peaks in the band ranges from 420 to 480 cm^{-1},

ii. Number and intensity of peaks: the number of the observed peaks and their corresponding intensity are found to be influenced by the elemental constituents of the thin films, which are issued from substrate, organic residuals during the elaboration as well as by the experimental conditions,

iii. Shift in peak position: the small shift observed in the peak position of absorption peak is attributed to the change in the bond length due to the substitutional doping Cu with Zn,

iv. Absorption of species on the surface: observation of various bands in CZO films might be due to the modification induced by the presence of different specious on the surface.

I.1.6. X-ray photoelectron spectroscopy characterization on Cu-doped-ZnO

One of powerful surface analysis method is X-ray photoelectron spectroscopy (XPS). It can provide the chemical state and electronic properties of materials **[100]**. This tool is widely used and immensely popular in the characterization of CZO thin films as it can give the detail of structural information and chemical environment (defects and chemical states). The surface or interface properties of thin films are well known to play an important role for devices application such as chemical reaction between electrode and electrolyte in batteries, supercapacitors, fuel cells, solar cells, and active region in p-n junction of semiconductor. Therefore, the characterization of Cu doped ZnO thin films using XPS are crucial for both fundamental and application interests. In principles, the electrons will be emitted when the X-ray photon energy absorbed by core or valence electrons is greater than binding energy of electrons (photoelectric effect). Then, the binding energy of core or valence electrons and chemical shift determined from XPS spectra is useful for the surface characterization of materials **[101]**. Since the depth of surface analysis is ~ 10 nm, sample preparation for CZO thin film generally requires careful protection. However, handling of thin film is easier that other type of samples. Commonly samples with dimension ~1x1 cm^2 and thickness less than 1 cm is suitable for most XPS machine. The sample handling for XPS is covered in detail elsewhere **[102].** The uniqueness of binding energy and particular element can be found on the surface is used by XPS to identify the elements present on the surface of the analyzed material, then the result is plotted by binding energy (eV) vs. intensity (count per second). General scans start from a range of 0 to 1200 eV for CZO material, for analysis specific range for Zn (1000-1050 eV), O (500-530 eV) and Cu (900-960 eV) are the focus.

XPS spectra revealed that the Cu doped ZnO thin films synthesized using sol gel method are in high quality films with survey spectra show no extra peaks from the other elements were detected **[4, 49, 52]**. Therefore, the composition of Zn, O, C and Cu close to the expected chemical compositions were confirmed to be presented in Cu doped ZnO thin films, where the

substitution of Cu for Zn sites was considered **[4, 52]**. In this case, difficult to identify the type of Cu as a dopant, whether it is substitution at Zn sites or become interstitial in ZnO lattice. Further XPS analysis was carried out using curve/peak fitting to determine the present of Cu^{+} and Cu^{2+} states and defects (Oxygen vacancy and interstitial) in Cu doped ZnO thin films **[103]**. The mixed Cu^{+} and Cu^{2+} states were reported to exist in most of Cu doped ZnO thin films with the different chemical state composition depends on Cu concentration and synthesis condition (pH and temperature) **[103, 104].**

The other possible defect created in Cu doped ZnO thin films has also been discussed, the peak fitting revealed that the peak at around 531.4 eV is attributed to Oxygen vacancy **[52, 103]**. The additional information on the interaction between Zn, Cu and O ions, interstitial region, and adsorbed species (O_2, H_2O and -CO_3) on surface have been elucidated **[4, 105]**. On the other side, to avoid the analysis error in Cu doped ZnO thin films due to the contamination effect at surface, the XPS approach with different angle of thin films (surface, sub-surface and bulk) and ultrahigh vacuum (UHV) treatment were used **[106]**. This gives a better understanding on the effect of surface contaminated in Cu doped ZnO thin films.

The characterization on surface of Cu doped ZnO thin films using XPS method are typically based on:

i. The peak positions of XPS spectra: provide information on core or valence electron for chemical environment of Cu doped ZnO films.

ii. Curve/peak fitting of XPS spectra: demonstrate the correlation of curve/peak positions with chemical state of Cu^{+} and Cu^{2+}, oxygen vacancy and possible interstitial.

I.1.7. Magnetic properties of Cu doped zinc oxide thin films

Various magnetic parameters such as saturation magnetization, coercive magnetic field, remanent magnetization, magnetic moment and Curie temperature (*TC*), can be extracted from Magnetic field dependent magnetization (*M–H*) hysteresis loop. In recent years, nonmagnetic ZnO based diluted magnetic semiconductors have attracted extensive attention for their possibility to exhibit room-temperature ferromagnetism. Many reports on CZO system mostly analyse and discuss about the mechanism of its ferromagnetism and to solve the controversial issue such as control, origin and improvement of ferromagnetism **[33, 34, 50, 75]**.

Most of the magnetization properties were presented as a function of applied field (*M–H*) hysteresis curves at different Cu contents of the CZO films (**Figure 8**) **[33, 34, 75]**. The saturation magnetization (MS) was found to be influenced by increasing Cu dopingconcentrations. Few reports on MS measurement at room temperature showed the increasing of MS with Cu content **[33, 34]**, but it exhibited a deceasing after 2% of Cu doping **[34]**. Others reported that CZO exhibited a low value of MS when the concentration of Cu was increased **[50, 75]**, in such works the films become nonmagnetic or negligibly ferromagnetic at room temperature **[50]** or even at 10 K **[75]**. In the latter case, CZO films exhibited only paramagnetic behaviour at lower Cu concentrations (0.5 and 0.75 mol.%) **[75]**. Even after a long discussion on the evolution of MS with Cu doping and temperature, the issue is still left open. In the following paragraphs, the discussion of the effect of Cu doping concentration and temperature on the MS of CZO thin films are summarized.

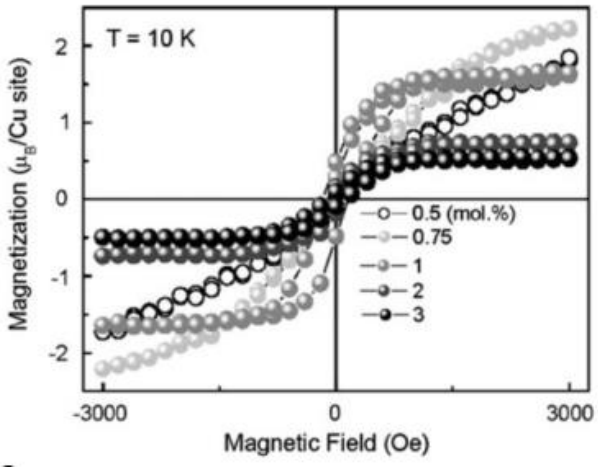

Figure 8. Magnetic hysteresis loops of CZO thin films with Cu content of 0.5, 0.75, 1, 2 and 3 mol.% **[75]**.

ZnO thin films doped with Cu content of 0.5, 0.75, 1, 2 and 3 mol.% produced high values of the saturation magnetization at Cu content of 1 mol.% by the increasing of hole carriers, which improves the ferromagnetic spin-ordering **[75]**. The decrease of MS at Cu content greater than 2 mol.% was then attributed to the increase in anti-ferromagnetic interactions due to the formation of CuO and Cu clusters. A similar decreasing was also observed for CZO thin films synthesized by sol-gel technique with Cu concentration of 1, 2, 3 and 4 at.% **[50]**, where the authors attributed the decreasing in the saturation magnetization to the enhanced anti-ferromagnetic coupling between Cu-Cu cations which overcomes ferromagnetic coupling. In a later work for CZO at low Cu concentrations (0.5, 1, 3 and 5 at.%),

it was indicated an obvious room-temperature ferromagnetism behaviour in all the prepared samples and a decrease of MS and coercive field with increasing level of Cu doping **[33]**. In a recent work for CZO thin films with Cu concentration of 0, 0.05, 0.1, 0.5, 1, 2, 2.5, 5 and

at.% **[34]**, it was found that *TC* is well above the room temperature, undoped ZnO thin films are diamagnetic, and ferromagnetic order is independent on temperature. This ferromagnetism in CZO thin films was then explained by the overlapping of bound magnetic polarons, due to exchange interaction between ion spin of the localized hole and the spin of Cu^{2+}, and **MS** of ~1.87 and ~1.72 $\mu B/Cu^{2+}$ were indicated in CZO thin films for Cu content of 0.05 and 0.1%, respectively **[34].**

Overview on magnetic properties of CZO thin films, reported from recent advances, can lead to the following notes,

- **i.** Control of ferromagnetic ordering: ferromagnetism in CZO thin films is controlled by the heating temperature, formation of CuO and Cu clusters, and the concentration of defects,
- **ii.** Ferromagnetic improvement: Cu doping can improve the ferromagnetic ordering of ZnO thin films, which is usually diamagnetic,
- **iii.** Origin of ferromagnetism: the overlapping of bound magnetic polarons and the spin of Cu^{2+} may be the origin of ferromagnetism in CZO.

I.1.8. Conclusion and prospectus/future/outlook

Various studies have been carried out on the investigation of CZO thin films in view of various applications. A summary of structural, electronic and optical parameters of CZO thin films was investigated in order to understand their evolution by increasing level of Cu content under variety of experimental conditions. It was found that each combination solvent-precursors-additive under various experimental conditions as well as the elaboration method strongly affects the various properties of elaborated CZO thin films. **T**he crystallite size, lattice constants, lattice strain, diffraction peaks, band gap, transmittance, surface morphology, FTIR spectroscopy, Raman spectroscopy, and magnetic properties were found to be influenced by increasing Cu doping. Moreover, various experiments with the same Cu content led to results possessing a contradictory evolution. This confirmed the effect of the involved experimental parameters on the growth and structure of CZO thin films.

Best knowledge on the combined effects of the preparation method and conditions as well as adding material, i.e. Cu, help in exploring a variety of new potential applications for CZO thin films**.** So, further researches are required to produce homogenous incorporation of Cu dopant into ZnO host lattice and to gain more insights into the CZO preparation-property-application relationship. We hope to provide support in the area of elaboration process, characterization and properties of metal oxides thin films and our review can open the door to researchers working on CZO thin films elaboration to improve their performance for the typical applications, like gas sensing and optoelectronic devices technology, or even to exploring new applications in technological devices.

I.2. A review on DFT+U calculations for properties of copper doped ZnO wurtzite

I.2.1. Introduction

Zinc oxide (ZnO) doped with transition metal (TM) has exhibited a increasing interest due to its recognized potential in many technological devices **[40].** Copper (Cu) with an ionic radii close to that of the Zn, can easily substitute it as dopant in ZnO host lattice **[107-109]**. This economical option, i.e. Cu dopant, has been selected to enhance the conductivity and photocatalytic activity of ZnO host lattice **[35, 95]**.

The development of efficient model based on theoretical and computational methods for dealing with many body problems is therefore essential to the research in the condensed matter theory. To predict the electronic ground states, the plane-wave pseudopotential (PWPP) density functional theory (DFT) has been successfully used. Moreover, the traditional theory DFT does not well describe the localization of strongly correlated *d* and *f* electrons of the metal oxides, leading to underestimating their band gap **[110]**. Thus, to improve such calculations, DFT–LDA+U approach becomes a necessity **[110-113]**. Many theoretical studies on Cu-doped ZnO have been available in the literatures **[91, 114-124]**. However, the experimental band gap value of CZO was found more underestimated by the calculated band gap. As a result, additional calculations with convenient Hubbard U values are still justified in order to improve the band gap. In this section we review the progress of first-principles calculation within DFT + U method of CZO materials.

I.2.2. A summary of the structural configurations and the convergence criteria for geometry optimization

The optimized ZnO primitive cell and substitutional method are usually used to derive ZnO supercell model (**Figure 9a and b**), which were widely used in first principles calculation to achieve the considered doping or defects architecture with a space group and lattice parameters (**Figure 9c**). Many defect-host lattice configurations, such as zinc vacancies(V_{Zn}), oxygen interstitial (O_i) oxygen vacancies (V_O), zinc interstitials (Zn_i), oxygen antisites (O_{Zn}) and zinc antisites (Zn_O), have been reported **[125-129]**. There have been several theoretical studies on Cu-doped ZnO **[5, 91, 114, 115, 117-120, 122, 124, 130-133]**, which have been performed by different modern computational package, such as CASTEP, VASP and SCIESTA, in order to investigating the effect of Cu doping on the properties of ZnO. Several convergence threshold criteria are needed to obtain precise calculations such as the maximum allowable stress (MS), maximum atomic displacement (MD), maximum force (MF) and energy change (EC) **[5, 91, 114, 115, 117, 119, 120, 122, 124, 130-133]**. Therefore, Zn-$4s^2 3d^{10}$, Cu-$3d^{10}4s^1$, and O-$2s^2 2p^4$ are considered as valence electron configuration in most of calculations on CZO structures **[5, 114, 115, 117, 118, 122, 130]**. Most of the calculation have been done using Perdew–Burke–Ernzerh of scheme (PBE) as exchange–correlation functional **[5, 91, 114, 115, 117, 119, 120, 122, 124, 130-133]**. Few other works have used Perdew–Wang 91 scheme (PW91) **[118, 133]**. Energy cut-off (E_{cut}) is ranging from 340 to 550 eV and depends on the pseudopotential type such as Ultrasoft pseudopotential (USP), Norm-conserving (NC), Projector augmented wave (PAW) pseudo-potentials. The Brillouin zone is sampled by k-point meshes (K-P-K) which depends on the supercell volume.

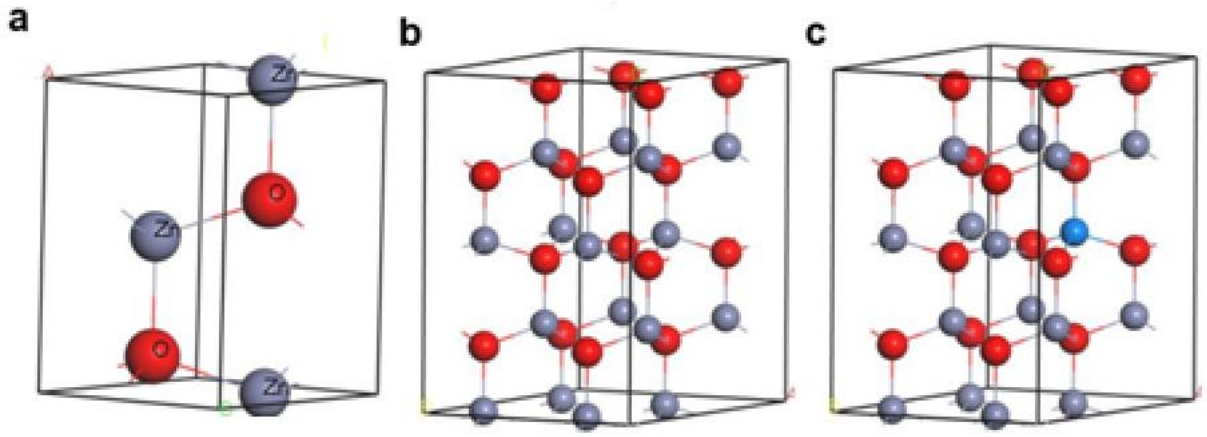

Figure I.9. (a) ZnO wurtzite primive cell, **(b)** 2x2x2 supercell structure of ZnO wurtzite, **(c)** supercell structure of Cu (blue) doped ZnO. Cells were constructed using the Materials Visualizer within the Materials Studio environment.

Calculated band gap of CZO was found to be more overestimated by the experimental band gap value, although some studies have used the DFT + U approach **[5, 91, 114, 115, 118-120, 124, 131-133]** (**Table 1**). So, further calculations with convenient Hubbard U values are still required to enhance the band gap. The incorporation of U*d,Zn,* U*d,Cu* and U*p,O*,which are also found to be fairly localized **[134]**, has successfully reproduced correct band gap **[5, 114]**. The typical values are around of 5, 8, and 5 eV for U*d,Zn,* U*d,Cu* and U*p,O*, respectively (**Table 1**).

Table I.1: The convergence and input criteria of computer code used in the first-principles calculation for CZO wurtzite structures at various Cu concentration *x* (%) and Hubbard-U values (literature survey from 2010 to 2020).

***x*(%)**	**Hubbard-U (eV)**			**Code/ Magnetic state**	**xc functional/ Basis set**	**Optimization criteria**						**Eg (eV)**	**Ref.**
	d-Zn	**p-O**	**d-Cu**			**EC × 10^{-6}**	**MS (GPa)**	**MD×10^{-4} (nm)**	**MF (eV/nm)**	**E_{cut} (eV)**	**KP**		
0 **2.78** **4.17**	5	8	5	CASTEP/ -	GGA-PBE-U/ USP	0.2	0.10	2	0.05	-	9×9×6 3×3×2 4×2×2	3.373 2.510 -	**[114]**
2.8 **4.2** **5.6** **12.5**	-	-	-	VASP/ FM	GGA-PBE-U/ PAW	-	-	-	-	500	8×8×8 Primitive cell	-	**[131]**
4.2	0	-	1	VASP/ FM	GGA-PBE+U/ PAW	-	-	-	-	500	3×4×2	-	**[124]**
2 **4** **6**	-	-	-	VASP/ FM+AFM	GGA- PBE	0.1	-	-	0.2	400	3×3×3	Decreases with *x*	**[117]**
0 **6.25** **18.75** **12.5** **25**	-	-	-	CASTEP/ -	GGA- PBE/ NC	2	0.1	2	0.5	460	7×7×4 4×4×2 4×4×2 4×4×2 4×4×2	Decreases with *x*	**[122]**
5.6	7.5	-	5	VASP/ FM	GGA-PW91/ PAW	-	-	-	0.1	550	4×4×4	-	[**118**]
12.5	6.5	-	1	VASP/ AFM	GGA-PBE-U/ -	-	-	-	0.1	400	7×7×1	2.36	**[115]**
0 **3.13** **6.25**	5.5	8	6	CASTEP/ FM	GGA-PBE-U/ USP	0.1	0.05	1	0.3	380	4×4×1	3.44 3.25 3.18	**[5]**
6.25	-	-	-	CASTEP/ -	GGA- PBE/ -	0.2	0.05	2	0.1	480	6×6×3	0.42	**[132]**
3.12	10.5	7	4.5	CASTEP/ -	GGA-U/ -	0.1	0.05	1	0.3	400	3×3×2	-	**[133]**
0 **10** **20** **30**	-	-	-	SCIESTA/ -	GGA-PBE/ LCAO	-	-	-	-	400	15×15×9	2.78 2.56 2.44 2.31	**[120]**
0 **3.12**	-	-	-	CASTEP/ -	GGA- PBE/ -	0.1	0.10	2	0.5	340	4x4x2	0.80 0.48	**[119]**
0 **3.1**	-	-	-	CASTEP/ -	GGA- PBE/ USP	0.1	1	2	0.3	380	4×4×2	0.741 0.295	**[91]**

I.2.3. Structural properties of CZO

The optimized lattice parameters determined by LDA usually underestimates the experimental value (a = 3.250 Å, c/a = 1.6021) by approximately–2% [15,31,36] whereas GGA overestimates the experimental lattice constant by approximately of 2% **[111, 135]**. The implementation of Hubbard-U parameter in the optimization work has a slight influence on the lattice constant. By increasing U(Zn-*3d*) parameter from 5.5 to 10.5 eV in GGA, the lattice constant a increases from 3.248 to 3.283 Å at Cu doping of 3.12% (**Table 2**). The Zn-O bond length ranges from 1.900 to 2.014 Å while the Cu-O bond length ranges from 1.890 to 2.026 Å **[5, 91, 115, 124]**. The bond length for both Cu-O and Zn-O exhibit values along c axis greater than those perpendicular to c axis **[5, 91]**. Furthermore, for a given Cu content, the bond lengths of Cu-O parallel and vertical to c-axis are lower than those of Zn-O in pure ZnO structures. This due to the replacement of Zn^{2+} with Cu^{2+}, which has an ionic radii less than that of Zn^{2+}.

Table I.2: Average bond length and lattice constants of CZO wurtzite structures at various Cu concentration *x* (%) and Hubbard-U values (literature survey from2010 to 2020) obtained from first-principles calculation. (//C) indicates length along c axis, (|c) refers to length perpendicular to c axis.

x (%)	Hubbard-U (eV)			Bond length (A°)		Lattice constant (A°)		Ref.
	d-Zn	p-O	d-Cu	Zn-O	Cu-O	*a=b*	*c*	
0						3.249	5.205	
2.78	5	8	5	-	-	3.249	5.205	[**114]**
4.17						3.272	5.284	
4.2	0	-	1	-	2.012	3.253	5.214	**[124]**
0						3.254	5.222	
6.25						-	5.210	
12.5						-	5.190	**[122]**
18.75	-	-	-	-	-	-	5.175	
25						-	-	
2.8	7.5	-	5	-	-	3.195	5.139	**[118]**
5.6								
12.5	6.5	-	1	1.90	1.89	3.29	5.30	**[115]**
0				2.004 (//C), 2.014(|c)	-	3.249	5.205	
3.13	5.5	8	6	-	1.992 (//C), 1.973(|c)	3.248	5.204	**[5]**
6.25				-	1.991 (//C), 1.972(|c)	3.247	5.203	
6.25	-	-	-			3.290	5.290	**[132]**
3.12	10.5	7	4.5			3.283	5.287	**[133]**
0	-	-	-	-	-	3.326	5.420	**[119]**
3.12						3.326	5.417	
0	-	-	-	2.009 (//C), 2.001(|c)	-	-	-	**[91]**
3.1				-	2.026 (//), 2.005 (|c)			

I.2.4. Electronic and optical properties of CZO

I.2.4.1. Band gap energy and band structure

The energy band structure and its corresponding density of states (DOS) are generally calculated to reflect the electronic behaviour of CZO structures, which is useful in the device design. A direct-type band gap located at the centre of the k-point grid (*Γ*) was revealed by the typical calculated energy band structure of pure ZnO structure (**Figure 10**) using Hubbard correction **[114]** or CZO structure without including Hubbard correction **[132]**. In many reports, the calculated energy band gap of CZO does not exceed 1 eV, which is severely underestimated by the experimental findings **[91, 117, 119, 132]** and tends to be decreased with Cu doping. These are caused by the deficient of using GGA that underestimate the binding energy in *d*-state **[135, 136]**. Previous studies have found that adding U*d,Zn* and/or U*d,Cu* alone slightly improved the calculated band gap, but the result still underestimated the experimental band gap **[115, 118, 124]**. Furthermore, including U*p,O* improved significantly the calculated band gap **[5, 114, 133]**.

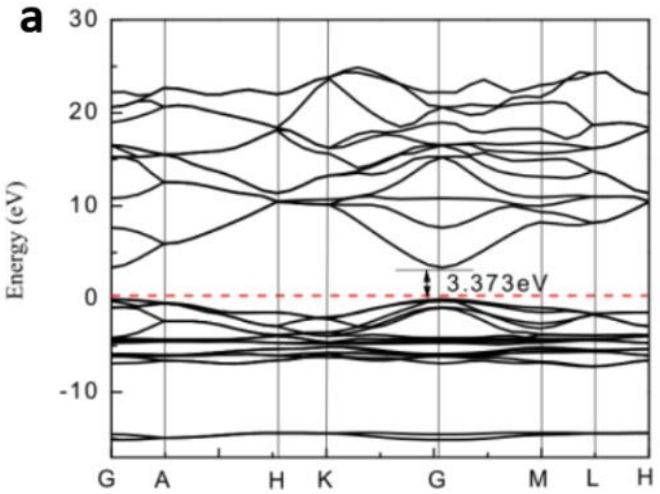

Figure I.10. Band structure of pure ZnO (UZn-3d=5, UO-2p=8) reprinted from Ref. **[114]**.

I.2.4.2. Electronic density of states

The contribution of the partial density of states (PDOS) from various valence states to the total density of states (TDOS) are tabulated (**Table 3).** This helps to understanding of electronic properties of the system under study. The valence band of CZO structures is generally divided

into three regions. The deep region is mainly generated from the O-2s states with a part from Cu-2s in the case of doping. The intermediate region is primarily derived from the Zn-3d, Zn-4s states and Cu-3d and a some contribution from the O-2p states. Cu 3d states contribute a lot to the shallow region (the upper VB) and overshoot the Fermi level by introducing an acceptor states **[119]**. A partial contribution is also marked for the O-2p states in this region. The conduction band is derived from Zn-*4s* and O-*2p* states. In this band, Cu causes localized density peaks in the minority spin near the Fermi level **[114, 124, 131]**. Report also indicated that the unoccupied Cu 3d states generate impurity levels at 1.62 eV in the band gap **[133]**.

To study the effect of the Hubaard parameter U on the relaxed electronic structure, total density of states (TDOS) and partial density of states (PDOS) for the relaxed $Cu_{0.042}Zn_{0.958}$ O compound with and without including Hubaard correction U, were investigated **[131].** By including Hubbard correction, it was observed that in the majority spin region, the states are pushed up near the Fermi level while the states become less localized in the minority spin region near and above the Fermi level. This makes CZO structure nearly half-metallic using GGA. This was confirmed in other previous work **[117]**, in which the incorporation of Cu atoms influences the bandgap and makes ZnO system half-metallic, with total spin-down polarization at Fermi level.

Table I.3: PDOS Contribution to TDOS of CZO wurtzite structures at various Cu concentration *x* (%) and Hubbard-U values obtained from first-principles calculation (literature survey from 2010 to 2020). VB; valence band, CB; conduction band, SC; semiconductor, FL; Fermi level.

***x* (%)**	**Hubbard-U (eV)**			**Valence band peaks**	**Conduction band peak**	**Ref.**
	d-Zn	**p-O**	**d-Cu**			
0 **2.78** **4.17**	5	8	5	-From −4 to 0 eV is mainly originated from Cu-3d and a part of O-2p and Zn-3d. -From −8 to −4 eV is mainly derived from Zn-4s and a part of O-2p.	-Dominated by Cu-3d state and a part of O-2p and Zn-4s states. - Cu causes localized density peaks near FL	**[114]**
2.8 **4.2** **5.6** **12.5**	-	-	-	-From −3 to 0 eV is mainly derived from Zn-3d and some contribution from O-2p and Cu-3d states.	-Dominated by state of Cu-3d and a part of O-2p states. - Cu is just above the upper VB, -ZnO becomes a p-type SC.	**[131]**
4.2	0	-	1	-Below and near the FL, in the minority spin, 2 peaks belong to 3d-Cu and 2p-O states are shown.	-Above and near FL, in the minority spin, one peak (t2-Cu) state is shown.. -Localized (holes) d states are shown above VBM (Fermi level).	**[124]**
2 **4** **6**	-	-	-	-The Cu-atom constitutes the VB maximum.	-The Cu-atom constitutes the CB minimum.	**[117]**
0 **6.25** **12.5** **18.75** **25**	-	-	-	- O-2s bond to Cu-2s causes the peak located between –18 and –16 eV. - From -7 to –4.5 eV is dominated by Zn-3d. - Cu 3d states contribute a lot to the upper VB and overshoot the FL. -From -6.9 to 0 eV is predominant by O-2p.	-CB is primarily derived from O 2p and Zn 4s states.	**[122]**
2.8 **5.6**	7.5	-	5	-From −5.5 to −5.8 eV is mainly derived from O-2p states. -The unoccupied Cu 3d states are found to be located in the band gap. -From −5 to 0 eV is mainly originated from O-2p and a part of Cu-3d.states.	It is dominated by state of Cu-3d and a part of O-2p states.	**[118]**
3.13 **9.37**	5.5	8	6	- From 5.5 to -7.5 eV is primarily derived from Cu-3d, O-2p and Zn 4s states -Cu 3d states contribute a lot to the upper VB. - Partial contribution of O-2p in -4.5 - 0 eV.	-Localized Cu-3d states are shown above VBM (FL). - -CB is primarily derived from O 2p and Zn 4s states.	**[5]**
6.25	-	-	-	-From −18.1 to −16 eV is mainly originated from O-2s states. -From −7.5 to -5 eV is mainly originated from Zn-3d and a part of O-2p states. -From −5 to 0 eV is mainly originated from O-2p and a part of Cu-3d states.	-It is dominated by state of Zn-4s. -The impurity level up-shifting toward VB maximum (FL push in the VB at 0.105 eV)	**[132]**
3.12	10.5	7	4.5	-From −20 to −18 eV is mainly originated from O-2s states. -From −10 to −4.9 eV is mainly originated from Zn-3d and O-2p states. -From −2.5 to −1 eV is mainly originated from O-2p states and a part of Cu-3d states.	-It is dominated by Zn-4s states. -The unoccupied Cu 3d states generate impurity levels at 1.62 eV in the band gap.	**[133]**
3.12	-	-	-	-From −6 to 0 eV is mainly originated from Zn-3d and a part of O-2p states. -The Cu doping can introduce the acceptor states.	-It is dominated by Zn-4s and a part of Zn-3p states. -The FL is composed of Cu-3d states.	**[119]**

I.2.4.3. Mulliken population

Mulliken analysis from frst-principles calculations are required to investigate the nature of chemical bonding and bond populations of CZO system. The bond population values for both Cu-O and Zn-O along c axis was found to be greater than those perpendicular to c axis **[5, 91]**. Besides, in order to investigate the interactions and bonding among adjacent atoms, electron density differences at (0 0 2) plan for pure ZnO and CZO structures (x=3.13 and 6.25%) were shown (**Figure 11**) **[5]**. The extent of overlapping among the neighbouring electronic clouds for Zn-O bonds in pure ZnO structure becomes noticeable indicating that the covalent bonds weaken while the extent of overlapping weakens with increasing Cu-doping content for Cu-O and Zn-O, which means that the ionic bonds strengthen. This due to the difference in electronegativity for Zn (1.65) and Cu (1.8).

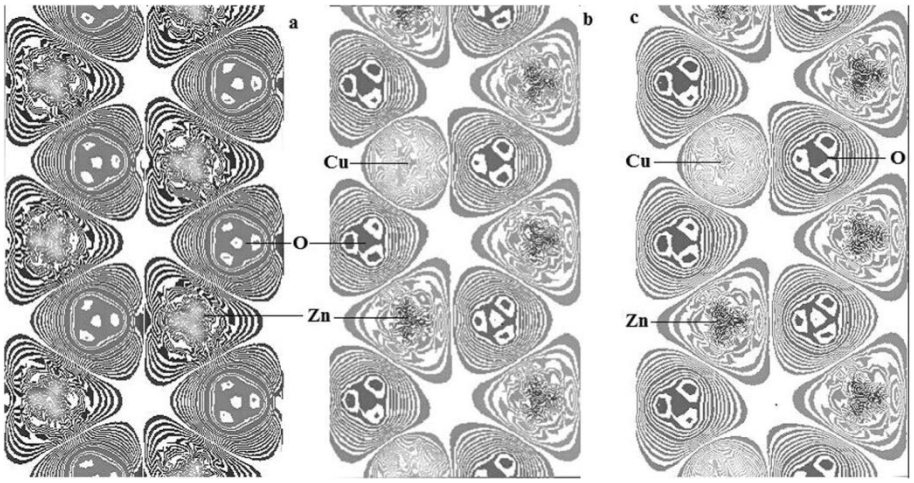

Figure I.11. Electron density differences in (0 0 2) plan for (a) undoped ZnO, (b) $Zn_{0.9687}Cu_{0.0313}O$, and (C) $Zn_{0.9375}Cu_{0.0625}O$ structures, reprinted from Ref. **[5]**.

I.2.4.4. Optical absorption

The dielectric function is an essential parameter to describe the behaviour of matter subjected to the effect of an external electromagnetic excitation (light). It represent the ratio of the permittivity of a substance to the permittivity of the vacuum and is defined as **[137]**:

$$\varepsilon(\omega) = \varepsilon_1(\omega) + i\varepsilon_2(\omega)$$

where $\varepsilon_1(\omega)$ and $\varepsilon_2(\omega)$ is the real and imaginary part of the dielectric function. Other optical properties, such as extinction coefficient, refractive index, reflectivity, loss function, absorption

coefficient, optical conductivity, static and high-frequency dielectric constants can then be deduced from calculation of the dielectric function.

There are three main peaks that usually constitutes the basic imaginary plot of the dielectric function **[115, 122, 132, 133]** located at different values of the incident photon energy (**Table 4**). It can be seen that the values of Ud,Zn, Ud,Cu and Up,O exhibit an obvious effect on the location of each peak. This is expected, where the states included in a given peak from the transition between conduction and valence bands, are down warded or up warded by the influence of the Hubbard values (U).

Electron excitation of O-*2p* state from valence band to Zn-*4s* state from conduction band, is generally responsible for emission at the first peak, which is shifted toward low energies by Cu doping **[115]**. Furthermore, Cu doping can produce a new peak at about 2.8 eV. The second peak results from electron excitation of Zn-*3d* occupied states at lower-energy of valence band to O-*2p* unoccupied states of conduction band. Report indicated that this peak shows a blue shift by Cu doping **[122]**. The excitation of Zn-*3d* state to unoccupied conduction state O-*2p* (or sometimes O-2s) state is referred to the third peak. Cu doping can also induce a blue shift to this peak **[122].** A forth peak is sometimes observed in the imaginary plot of the dielectric function **[132, 133]**. The position of these peaks, which may vary with the various Hubbard values U, is based on the joint DOS of states within the conduction and valence bands included in the corresponding transition.

Table I.4: Peaks and their origin in the imaginary part of dielectric function of CZO wurtzite structures at various Cu concentration *x* (%) reported from first-principles calculation in literature.

***x* (%)**	**Hubbard-U (eV)**			**Peak and origin**				**Ref.**
	d-Zn	**p-O**	**d-Cu**	**First**	**Second**	**Third**	**Forth**	
0 **6.25** **12.5** **18.75** **25**	-	-	-	At 1.13 eV is caused by transition from O-*2p* (VB) to Zn-*4s* (CB). -It shifts toward low energy by Cu doping.	At 5.99 eV is caused by transition from Zn-*3d* (VB) to O-*2p* (CB). - It shows a blue shift by Cu doping.	At 10.6 eV is caused by transition from Zn-*3d* (VB) to O-*2p* (CB). -It shows a blue shift by Cu doping.	-	**[122]**
12.5	6.5	-	1	-New peak appears at about 2.8 eV by Cu doping.	-Peak at 4.4 eV decreases gradually with Cu doping.	-	--	**[115]**
6.25	-	-	-	-At 4.4 eV; is due to transition from O-2p (VB) to Zn-4s (CB). -It shifted toward the lower energy.	At 8.9 eV is due to transition from O-2p (VB) to Zn-4s (CB)	At 12.5 eV; is due to transition from Zn-3d (VB) to highest Zn-4s (CB).	At 14.8 eV; is due to transition from Zn-3d (VB) to Zn-4s (CB).	**[132]**
3.12	10.5	7	4.5	-At 1.6 eV is due to transition from O-2p (VB) to Zn-4s (CB). -It shifts toward the lower energy.	At 3.4 eV is due to transition from Zn-3d to O-2p states	At 6.4 eV is due to transition from O-2s (VB) to Zn-3d CB).	At 10.6 eV is due to transition from O-2s (VB) to Zn-3d (CB).	**[133]**

I.2.5. Magnetic properties of CZO

Report on the effect of the Hubbard value (U) of Cu-3d and Zn-3d states on the magnetic properties of Cu-doped ZnO structure at concentration of 4.2% **[124]**, noticed that the ground state of system exhibits ferromagnetic (FM) with Ueff < 3 eV but changes to AFM for U>3 eV whereas this system displays an AFM ground state as U for both Cu-3d and Zn-3d are considered. The authors reported that the FM exchange interaction between Cu are suggested to be mediated by the holes induced in p-d hybridization.

Copper atoms were substituted at Zn-site on pristine ZnO system at different Cu concentration (x=1, 2 and 3%) and for different distance between the Cu dopants **[117]**. In order to understand the stability of spin magnetic ordering, the ground state total energy of parallel or

anti-parallel spin ordering have been studied. Calculations revealed that Cu-dopant induces ~1 $\boldsymbol{\mu_B}$ magnetic moment in the host lattice. CZO system behaved like ferromagnetic system for the close Cu-Cu distance (~3.1 Å) whereas it acts like anti-ferromagnetic system at the distance of ~5.1 Å. Again, the system becomes ferromagnetic material when the distance reaches to ~5.8 Å and ~7.9 Å.

Report on Cu-doped ZnO structure (*x*=2.77, 5.55 and 8.33%), found that the FM state is more energetically favourable than nonmagnetic (NM) or antiferromagnetic (AFM) state **[123]**. In other work on Cu-doped ZnO structures (*x*=2.8 and 5.6%), it was showed that the substitution of two Zn sites in the host lattice by two Cu atoms (nearest neighbours in the basal plane with the distance of 3.195 A) with ferromagnetic (FM) phase is the more stable than ant-ferromagnetic (AFM) phase **[118]**. Also, it was demonstrated that the local magnetic moment on the Cu site is 0.72 $\boldsymbol{\mu_B}$ and 0.69 $\boldsymbol{\mu_B}$ for *x*=2.8 and 5.6%, respectivly, when $U_{Cu\text{-}3d}$=5 eV, compared to the value of 0.57 $\boldsymbol{\mu_B}$ in the absence of $U_{Cu\text{-}3d}$ correction.

Density-functional theory calculations have been performed to study the magnetic and optical properties of Cu-doped ZnO nanosheet (NS; *x*=12.5), which was initially cut from a bulk W-ZnO with (001) polar surface **[115]**. Authors indicated that Cu atom prefers to substitute for Zn site inducing a local magnetic moment on the Cu site of 0.58 μB per unit in ZnO NS and anti-ferromagnetic (AFM) ordering was found to be energetically more favourable and Cu dopants tend to form a cluster.

DFT calculations on the ferromagnetic stabilities for CZO structure of 2% Cu doping concentration in different Cu-Cu separation revealed that the system behaves as a collection of isolated magnetic centre instead of long-range ferromagnetically ordered spins when the separation between two doped ions are 8 Å or more **[34]**. However, in case of small separation distance (less than 8 Å) a weak antiferromagnetic coupling was found.

The magnetic properties of Cu-doped ZnO wurtzite structure have been investigated using DFT calculations for six independent doping configurations **[121]**. The obtained results revealed that the substitutional Cu ions are spin polarized and have a tendency to be assembled. The ground state has shown a ferromagnetic phase for all configurations. The FM phase corresponding to the nearest-neighbouring positions of Cu ions is the more stable and exhibits a half-metal character. The ferromagnetic stability was attributed to the strong hybridization between Cu-3d and O-2p states. The local moment at Cu is about 0.53 $\boldsymbol{\mu_B}$ and the rest magnetic moment mainly arises from O ions.

I.2.6. Conclusion and prospectus/future/outlook

In this review, tabulated values and graphs on electronic, structural, optical, and magnetic properties of Cu-doped ZnO wurtzite structure are given to outline the effect of the Hubbard-U scheme on these properties within the framework of the first-principles study. It is found from the literature survey that the implementation of Hubbard U correction for U*d,Zn,* U*d,Cu* and U*p,O* all to gather has marked a slight difference in the lattice constant. Bond lengths parallel to c-axis are generally slightly higher than those vertical to it. Also, by using Hubbard U correction for only Zn-3d and/or Cu-3d states, a slight improvement in energy band gap has been achieved, but still do not represent the experimental one. The incorporation of U*d,Zn,* U*d,Cu* and U*p,O* all to gather has successfully reproduced correct band gap, which tends to be decreased with Cu doping. The magnetic ground state (FM or AFM) of CZO system has found to be influenced by the Hubbard value U for both Cu-3d and Zn-3d. The authors reported that the FM exchange interaction between Cu are suggested to be mediated by the holes induced in p-d hybridization. The local moment at Cu is about 0.53 $\boldsymbol{\mu_B}$ and the rest magnetic moment mainly arises from O ions. The values of U*d,Zn,* U*d,Cu* and U*p,O* has a significant effect on the position and intensity of the main peaks composed the imaginary part of the dielectric function, which are located at different values of the incident photon energy.

References

[1] J.B. Lee, M.-H. Lee, C.-K. Park, J.-S. Park, Effects of lattice mismatches in ZnO/substrate structures on the orientations of ZnO films and characteristics of SAW devices. Thin solid films, 2004, vol. 447, p. 296-301

[2] D. Borah, M.K. Baruah, P.P. Saikia, K.K. Senapoty, M. Barua, R. Singha, Structural characterization and surface environment of ZnO nanoflowers. Journal of Material and Environmental Science, 2016, vol. 7, p. 310-315.

[3] A.M. Díez-Pascual, Biodegradable food packaging nanocomposites based on ZnO-reinforced polyhydroxyalkanoates. Food packaging. Academic Press, 2017. p. 185-221.

[4] A.R. Nimbalkar, M.G. Patil, Synthesis of highly selective and sensitive Cu-doped ZnO thin film sensor for detection of H2S gas. Materials Science in Semiconductor Processing , 2017, vol. 71, p. 332-341.

[5] S. Guo, Q. Hou, C. Zhao, Y.J.C.P.L. Zhang, Study of the effect of Cu heavy doping on band gap and absorption spectrum of ZnO. Chemical Physics Letters, 2014, vol. 614, p. 15-20.

[6] P. Liu, Y. Guo, Q. Xu, F. Wang, Y. Li, K. Shao, Enhanced photocatalytic performance of ZnO/multi-walled carbon nanotube nanocomposites for dye degradation. Ceramics International, 2014, vol. 40, no 4, p. 5629-5633.

[7] H. Yin, P.S. Casey, ZnO nanorod composite with quenched photoactivity for UV protection application, Materials Letters 121 (2014) 8-11.

[8] T. Ootsuka, Z. Liu, M. Osamura, Y. Fukuzawa, R. Kuroda, Y. Suzuki, N. Otogawa, T. Mise, S. Wang, Y. Hoshino, ZnO nanorod composite with quenched photoactivity for UV protection application. Materials Letters, 2014, vol. 121, p. 8-11

[9] C. Jagadish, S.J. Pearton, Zinc oxide bulk, Zinc oxide bulk, thin films and nanostructures: processing, properties, and applications. Elsevier, 2011.

[10] J.M. Szarko, J.K. Song, C.W. Blackledge, I. Swart, S.R. Leone, S. Li, Y. Zhao, Optical injection probing of single ZnO tetrapod lasers. Chemical physics letters , 2005, vol. 404, no 1-3, p. 171-176.

[11] M. Karyaoui, A. Mhamdi, H. Kaouach, A. Labidi, A. Boukhachem, K. Boubaker, M. Amlouk, R. Chtourou, Some physical investigations on silver-doped ZnO sprayed thin films. Materials Science in Semiconductor Processing, 2015, vol. 30, p. 255-262.

[12] N. Narayanan, N.K. Deepak, Enhancement of visible luminescence and photocatalytic activity of ZnO thin films via Cu doping, Optik 158 (2018) 1313-1326.

[13] C.C. Yu, W.H. Lan, K.F. Huang, Enhancement of visible luminescence and photocatalytic activity of ZnO thin films via Cu doping. Optik, 2018, vol. 158, p. 1313-1326.

[14] Y.F. Hsiou, W.K. Hung, C.W. Wang, Fabrication of Sb-doped p-type ZnO thin films by pulsed laser deposition. Atlas Journal of Materials Science, 2015, vol. 2, no 1, p. 60-64

[15] V. Şenay, S. Pat, Ş. Korkmaz, T. Aydoğmuş, S. Elmas, S. Özen, N. Ekem, M.Z. Balbağ, ZnO thin film synthesis by reactive radio frequency magnetron sputtering. Applied surface science, 2014, vol. 318, p. 2-5.

[16] T. Morita, S. Ueno, T. Tokunaga, E. Hosono, Y. Oaki, H. Imai, H. Matsuda, H. Zhou, M. Hagiwara, S. Fujihara, Fabrication of transparent ZnO thick film with unusual orientation by the chemical bath deposition. Crystal Growth & Design , 2015, vol. 15, no 7, p. 3150-3156.

[17] J.-C. Hsiao, C.-H. Chen, H.-J. Yang, C.-L. Wu, C.-M. Fan, C.-F. Huang, C.-C. Lin, P. Yu, J.-C. Hwang, Highly textured ZnO: B films grown by low pressure chemical vapor deposition for efficiency enhancement of heterojunction silicon-based solar cells. Journal of the Taiwan Institute of Chemical Engineers, 2013, vol. 44, no 5, p. 758-761

[18] G. Poongodi, P. Anandan, R.M. Kumar, R. Jayavel, Studies on visible light photocatalytic and antibacterial activities of nanostructured cobalt doped ZnO thin films prepared by sol–gel spin coating method. Spectrochimica Acta Part A: Molecular and Biomolecular Spectroscopy, 2015, vol. 148, p. 237-243.

[19] R. Hussin, H. Yahya, N. Zulkiflee, Deposition of TiO 2 / ZnO Thin Films Using Spin-Coating Method. Int. J. Curr. Res. Sci. Eng. Technol , 2018, vol. 1, p. 226.

[20] D. Akcan, A. Gungor, L. Arda, Structural and optical properties of Na-doped ZnO films. Journal of Molecular structure, 2018, vol. 1161, p. 299-305.

[21] T. Saidani, M. Zaabat, M. Aida, B. Boudine, Effect of copper doping on the photocatalytic activity of ZnO thin films prepared by sol–gel method. Superlattices and Microstructures, 2015, vol. 88, p. 315-322.

[22] S. Osali, H. Esfahani, F. Dabir, P. Tajaslan, Structural and electro-optical properties of electrospun Cu-Doped ZnO thin films. Solid State Sciences , 2019, vol. 98, p. 106038.

[23] A. Sreedhar, J.H. Kwon, J. Yi, J.S. Kim, J.S. Gwag, Enhanced photoluminescence properties of Cu-doped ZnO thin films deposited by simultaneous RF and DC magnetron sputtering. Materials Science in Semiconductor Processing, 2016, vol. 49, p. 8-14

[24] S. Roguai, A. Djelloul, A structural and optical properties of Cu-doped ZnO films prepared by spray pyrolysis. Applied Physics A, 2020, vol. 126, no 2, p. 1-8.

[25] N.H. Hashim, S. Subramani, M. Devarajan, A.R. Ibrahim, A structural and optical properties of Cu-doped ZnO films prepared by spray pyrolysis. Applied Physics A, 2020, vol. 126, no 2, p. 1-8.

[26] G.-J. Chen, S.-R. Jian, J.-Y. Juang, Surface analysis and optical properties of Cu-doped ZnO thin films deposited by radio frequency magnetron sputtering. Coatings , 2018, vol. 8, no 8, p. 266.

[27] J.-H. Lee, K. Oh, K. Jung, K. Wilson, M.-J. Lee, Tuning the morphology and properties of nanostructured Cu-ZnO thin films using a two-step sputtering technique. Metals, 2020, vol. 10, no 4, p. 437.

[28] K. Joshi, M. Rawat, S.K. Gautam, R. Singh, R. Ramola, F. Singh, Band gap widening and narrowing in Cu-doped ZnO thin films. Alloys and Compounds, 2016, vol. 680, p. 252-258.

[29] S. Singhal, J. Kaur, T. Namgyal, R. Sharma, Cu-doped ZnO nanoparticles: synthesis, structural and electrical properties. Physica B: Condensed Matter, 2012, vol. 407, no 8, p. 1223-1226.

[30] B.K. Das, T. Das, K. Parashar, S. Parashar, R. Kumar, H.K. Choudhary, V.B. Khopkar, A. Anupama, B. Sahoo, Investigation of structural, morphological and NTCR behavior of Cu-doped ZnO nanoceramics synthesized by high energy ball milling. Materials Chemistry and Physics , 2019, vol. 221, p. 419-429.

[31] P. Shewale, Y. Yu, UV photodetection properties of pulsed laser deposited Cu-doped ZnO thin film. Ceramics International , 2017, vol. 43, no 5, p. 4175-4182.

[32] F. Dabir, H. Esfahani, F. Bakhtiargonbadi, Z. Khodadadi, Study on microstructural and electro-optical properties of sol – gel derived pure and Al / Cu-doped ZnO thin films. Journal of Sol-Gel Science and Technology , 2020, vol. 96, no 3, p. 529-538.

[33] S.-Y. Zhuo, X.-C. Liu, Z. Xiong, J.-H. Yang, E.-W. Shi, Defects enhanced ferromagnetism in Cu-doped ZnO thin films. Solid state communications, 2012, vol. 152, no 4, p. 257-260.

[34] N. Ali, B. Singh, Z.A. Khan, A. Vijaya, K. Tarafder, S. Ghosh, Z.A.Khan. Origin of ferromagnetism in Cu-doped ZnO. Scientific reports , 2019, vol. 9, no 1, p. 1-7.

[35] H.A. Al-Khanbashi, W. Shirbeeny, A. Al-Ghamdi, L.M. Bronstein, W.E. Mahmoud, Development of highly conductive and transparent copper doped zinc oxide thin films via 2-methoxyethanol modified sol – gel dip-coating technique. Ceramics International , 2014, vol. 40, no 1, p. 1927-1932.

[36] R. Raji, K. Gopchandran, ZnO: Cu nanorods with visible luminescence: copper induced defect levels and its luminescence dynamics. Materials Research Express, 2017, vol. 4, no 2, p. 025002.

[37] J.C. Fan, K.M. Sreekanth, Z. Xie, S.L. Chang, K.V. Rao, p-Type ZnO materials: Theory, growth, properties and devices. Progress in Materials Science, 2013, vol. 58, no 6, p. 874-985.

[38] L. Zhu, W.Zeng, Room-temperature gas sensing of ZnO-based gas sensor: A review. Sensors and Actuators A: Physical, 2017, vol. 267, p. 242-261.

[39] S. Das, V.C.Srivastava, An overview of the synthesis of CuO-ZnO nanocomposite for environmental and other applications. Nanotechnology Reviews, 2018, vol. 7, no 3, p. 267-282.

[40] B.G. Shohany, A.K. Zak, Doped ZnO nanostructures with selected elements-Structural, morphology and optical properties: A review. Ceramics International , 2020, vol. 46, no.5, p. 5507-5520.

[41] S. Prasad, V. Kumar, S. Kirubanandam, A. Barhoum, Engineered nanomaterials: nanofabrication and surface functionalization. In: Emerging Applications of Nanoparticles and Architecture Nanostructures . Elsevier, 2018. p. 305-340.

[42] D.V. Vu, D.H. Le, T.T. Nguyen, T. Van Duong, Q.D. Ngo, T.Q. Trinh, Study on material properties of Sn-and Cu-doped ZnO thin films as n-and p-type thermoelectric materials based on wet solution synthesis. Journal of Materials Science: Materials in Electronics, 2019, vol. 30, no 7, p. 6544-6551.

[43] E. Asikuzun, O. Ozturk, L. Arda, C. Terzioglu, Preparation, growth and characterization of nonvacuum Cu-doped ZnO thin films. Journal of Molecular Structure, 2018, vol. 1165, p. 1-7.

[44] V. Ganesh, G. Salem, I. Yahia, F. Yakuphanoglu, Synthesis, optical and photoluminescence properties of Cu-doped ZnO nano-fibers thin films: nonlinear optics. Journal of Electronic Materials , 2018, vol. 47, no 3, p. 1798-1805.

[45] K. Poornima, K.G. Krishnan, B. Lalitha, M. Raja, CdS quantum dots sensitized Cu doped ZnO nanostructured thin films for solar cell applications. Superlattices and Microstructures , 2015, vol. 83, p. 147-156.

[46] M. Raja, N. Muthukumarasamy, D. Velauthapillai, R. Balasundaraprabhu, Influence of copper on the morphology and properties of one dimensional ZnO nanorod structures. Superlattices and Microstructures , 2014, vol. 72, p. 102-110

[47] K. Ranjith, K. Vanishri, R. Rajendrakumar, Synthesis and catalytic properties of Al and Cu doped ZnO thin films on the photolytic degradation of methylene blue. Synthesis and Reactivity in Inorganic, Metal-Organic, and Nano-Metal Chemistry, 2014, vol. 44, no 9, p. 1316-1322.

[48] K. Chongsri, S. Aunpang, W. Techitdheera, W. Pecharapa, Preparation and characterization of Cu-doped ZnO sol-gel derived optical thin films. In: Advanced Materials Research . Trans Tech Publications Ltd, 2013. p. 124-128.

[49] P. Jongnavakit, P. Amornpitoksuk, S. Suwanboon, N. Ndiege, Preparation and photocatalytic activity of Cu-doped ZnO thin films prepared by the sol–gel method. Applied Surface Science, 2012, vol. 258, no 20, p. 8192-8198.

[50] H. Yang, X. Xu, S. Wu, K. Wu, C. Ai, J. Miao, Y. Jiang, Effects of dopants on magnetic properties of Cu-doped ZnO thin films. Journal of Materials Science , 2012, vol. 47, no 1, p. 530-533.

[51] H. Gómez-Pozos, E.J.L. Arredondo, A. Maldonado Álvarez, R. Biswal, Y. Kudriavtsev, J.V. Pérez, Y.L. Casallas-Moreno, M.D.l.L. Olvera Amador, Cu-Doped ZnO thin films deposited by a sol-gel process using two copper precursors: Gas-sensing performance in a propane atmosphere. Materials , 2016, vol. 9, no 2, p. 87.

[52] L. Xu, F. Xian, G. Zheng, M. Lai, Realization of strong violet and blue emissions from ZnO thin films by incorporation of Cu ions. Materials Research Bulletin, 2018, vol. 99, p. 144-151.

[53] S. Horzum, E. Torun, T. Serin, F. Peeters, Structural, electronic and optical properties of Cu-doped ZnO: experimental and theoretical investigation. Philosophical Magazine, 2016, vol. 96, no 17, p. 1743-1756.

[54] S. Yang, Y. Zhang, D. Mo, Structural, electronic and optical properties of Cu-doped ZnO: experimental and theoretical investigation. Philosophical Magazine, 2016, vol. 96, no 17, p. 1743-1756

[55] A. El Sayed, G. Said, S. Taha, A. Ibrahim, F.J.S. Yakuphanoglu, Influence of copper incorporation on the structural and optical properties of ZnO nanostructured thin films. Superlattices and Microstructures, 2013, vol. 62, p. 47-58.

[56] A.H. Rakhsha, H. Abdizadeh, E. Pourshaban, M.R. Golobostanfard, V.R. Mastelaro, M. Maziar, Ag and Cu doped ZnO nanowires: a pH-Controlled synthesis via chemical bath deposition. Materialia, 2019, vol. 5, p. 100212.

[57] Y.-C. Chang, C.-C. Hsu, S.-H. Wu, K.-W. Chuang, Y.-F.J.A.S.S. Chen, Fabrication of Cu-doped ZnO nanoneedles on different substrate via wet chemical approach: Structural characterization and photocatalytic performance. Applied Surface Science, 2018, vol. 447, p. 213-221.

[58] S.J.V. Aydemir, Effects of withdrawal speed on the microstructural and optical properties of sol–gel grown ZnO: Al thin films. Vacuum, 2015, vol. 120, p. 51-58.

[59] A. Mahroug, R. Amari, A. Boukhari, B. Deghfel, L. Guerbous, N. Selmi, Synthesis, structural, morphological, electronic, optical and luminescence properties of pure and manganese-doped zinc oxide nanostructured thin films: effect of doping. Journal of Nanoelectronics and Optoelectronics, 2018, vol. 13, no 5, p. 732-742.

[60] L.L. Hench, J.K. West, The sol-gel process. Chemical reviews, 1990, vol. 90, no 1, p. 33-72.

[61] N. Al-Dahoudi, Wet chemical deposition of transparent conducting coatings made of redispersable crystalline ITO nanoparticles on glass and polymeric substrates. 2003.

[62] S.D. Ponja, Metal oxide thin films for optoelectronic applications . 2018. Doctoral thesis. UCL (University College London).

[63] D. Wang, J. Zhou, G. Liu, The microstructure and photoluminescence of Cu-doped ZnO nano-crystal thin films prepared by sol – gel method. Journal of Alloys and Compounds , 2009, vol. 487, no 1-2, p. 545-549.

[64] C. Busuioc, S.I. Jinga, E. Andronescu, Filme subtiri pe baza de tantalat de bariu si magneziu obtinute prin procesare sol-gel/barium magnesium tantalate thin films obtained by sol-gel processing. Revista Romana de Materiale, 2012, vol. 42, no 3, p. 299.

[65] M. Aymerich, A.I. Gómez-Varela, E. Álvarez, M.T. Flores-Arias, Study of different sol-gel coatings to enhance the lifetime of PDMS devices: evaluation of their biocompatibility. Materials, 2016, vol. 9, no 9, p. 728.

[66] S. Thiagarajan, A. Sanmugam, D.J.R.A.i.S.-G.S. Vikraman, Facile methodology of sol-gel synthesis for metal oxide nanostructures. recent applications in sol-gel synthesis, 2017, p. 1-17.

[67] M.B. Rahmani, S.-H. Keshmiri, M. Shafiei, K. Latham, W. Wlodarski, J. Du Plessis, K. Kalantar-Zadeh, Transition from n-to p-type of spray pyrolysis deposited Cu doped ZnO thin films for NO2 sensing. Sensor Letters, 2009, vol. 7, no 4, p. 621-628.

[68] L. Znaidi, Sol–gel-deposited ZnO thin films: A review. Materials Science and Engineering: B, 2010, vol. 174, no 1-3, p. 18-30.

[69] Y. Xi, Y. Bai, K. Gao, X. Pang, H. Yang, L. Yan, A.Volinsky, In-situ stress gradient evolution and texture-dependent fracture of brittle ceramic thin films under external load. Ceramics International , 2018, vol. 44, no 7, p. 8176-8183.

[70] A.-I. Istrate, V. Dediu, I. Mihalache, C. Romanitan, O. Tutunaru, structural and opto-electrical analysis of Cu doped ZnO thin films by sol-gel method. In : 2019 International Semiconductor Conference (CAS). IEEE, 2019. p. 233-236.

[71] M. Kaliva, M. Vamvakaki, Chapter 17 - Nanomaterials characterization, R. Narain (Ed.), Polymer Science and Nanotechnology, Elsevier,2020, p. 401-433.

[72] A. Mhamdi, R. Mimouni, A. Amlouk, M. Amlouk, S. Belgacem, Study of copper doping effects on structural, optical and electrical properties of sprayed ZnO thin films. Journal of alloys and compounds, 2014, vol. 610, p. 250-257.

[73] M. Salem, I. Massoudi, S. Akir, Y. Litaiem, M. Gaidi, K. Khirouni, Photoelectrochemical and opto-electronic properties tuning of ZnO films: Effect of Cu doping content. Journal of Alloys and Compounds, 2017, vol. 722, p. 313-320.

[74] Q.A. Drmosh, S.G. Rao, Z.H. Yamani, M.A. Gondal, Crystalline nanostructured Cu doped ZnO thin films grown at room temperature by pulsed laser deposition technique and their characterization. Applied surface science, 2013, vol. 270, p. 104-108.

[75] C.O. Kim, S. Kim, H.T. Oh, S.-H. Choi, Y. Shon, S. Lee, H.N. Hwang, C.-C. Hwang, Effect of electrical conduction properties on magnetic behaviors of Cu-doped ZnO thin films. Physica B: Condensed Matter , 2010, vol. 405, no 22, p. 4678-4681.

[76] M. Toma, N. Ursulean, D. Marconi, A. Pop, Structural and optical characterization of Cu doped ZnO thin films deposited by RF magnetron sputtering. Journal of Electrical Engineering, 2019, vol. 70, no 7, p. 127-131.

[77] V. Kumar, R. Singh, F. Singh, L. Purohit, Highly transparent and conducting boron doped zinc oxide films for window of Dye Sensitized Solar Cell applications. Journal of alloys and compounds, 2012, vol. 544, p. 120-124.

[78] C. Cai, H. Zhang, J. Xie, L. Ma, The characterization of Cu-doped ZnO thin films prepared by using radio-frequency reactive magnetron sputtering. Journal of the Korean Physical Society, 2017, vol. 70, no 9, p. 856-860.

[79] P. Shewale, V. Patil, S. Shin, J. Kim, M. Uplane, H2S gas sensing properties of nanocrystalline Cu-doped ZnO thin films prepared by advanced spray pyrolysis. Sensors and Actuators B: Chemical , 2013, vol. 186, p. 226-234.

[80] M. Habibi, M.K. Sardashti, Structure and morphology of nanostructured zinc oxide thin films prepared by dip-vs. spin-coating methods. Journal of the Iranian Chemical Society, 2008, vol. 5, no 4, p. 603-609.

[81] A.A. Aboud, M. Shaban, N. Revaprasadu, Effect of Cu, Ni and Pb doping on the photo-electrochemical activity of ZnO thin films. RSC advances, 2019, vol. 9, no 14, p. 7729-7736.

[82] Y. Liu, H. Liu, Y. Yu, Q. Wang, Y. Li, Z. Wang, Structural and optical properties of ZnO thin films with heavy Cu-doping prepared by magnetron co-sputtering. Materials Letters , 2015, vol. 143, p. 319-321.

[83] S. Syed Zahirullah, J. Joseph Prince, P. Fermi Hilbert Inbaraj, Structural and optical properties of Cu-doped ZnO nanorods by silar method. Materials technology, 2017, vol. 32, no 12, p. 755-763.

[84] H. Wang, P.K. Chu, Surface characterization of biomaterials. In : Characterization of biomaterials. Academic Press, 2013. p. 105-174.

[85] G. Qian, Y. Li, A.R.J.S.S.R. Gerson, Applications of surface analytical techniques in Earth Sciences. Surface Science Reports , 2015, vol. 70, no 1, p. 86-133.

[86] D. Titus, E.J.J. Samuel, S.M. Roopan, Nanoparticle characterization techniques. In :Green synthesis, characterization and applications of nanoparticles. Elsevier, 2019. p. 303-319.

[87] A.S.H. Makhlouf, H. Soliman, Effect of nano-additives (Al2O3 and NaF) on the performance of ceramic coatings formed by microarc oxidation on magnesium alloys. In : Handbook of Nanoceramic and Nanocomposite Coatings and Materials. Butterworth-Heinemann, 2015. p. 389-401.

[88] H. Fritzsche, Electronic properties of amorphous semiconductors. In : Amorphous and Liquid Semiconductors. Springer, Boston, MA, 1974. p. 221-312 **.**

[89] S. Wemple, M. DiDomenico Jr, Behavior of the electronic dielectric constant in covalent and ionic materials. Physical Review B , 1971, vol. 3, no 4, p. 1338.

[90] J.E. House, Fundamentals of quantum mechanics, Academic Press2017.

[91] C. Xia, F. Wang, C. Hu, Theoretical and experimental studies on electronic structure and optical properties of Cu-doped ZnO. Journal of alloys and compounds, 2014, vol. 589, p. 604-608

[92] D.R. Baer, S. Thevuthasan, BAER, Donald R. et THEVUTHASAN, Suntharampillai. Characterization of thin films and coatings. In : Handbook of Deposition Technologies for Films and Coatings. William Andrew Publishing, 2010. p. 749-864.

[93] V. Russo, M. Ghidelli, P. Gondoni, C.S. Casari, A. Li Bassi, Multi-wavelength Raman scattering of nanostructured Al-doped zinc oxide. Journal of Applied Physics, 2014, vol. 115, no 7, p. 073508.

[94] P. Rostron, S. Gaber, D.Gaber, Raman spectroscopy, review. laser, 2016, vol. 21, p. 24.

[95] W. Vallejo, A. Cantillo, B. Salazar, C. Diaz-Uribe, W. Ramos, E. Romero, M.Hurtado, Comparative Study of ZnO Thin Films Doped with Transition Metals (Cu and Co) for Methylene Blue Photodegradation under Visible Irradiation. Catalysts, 2020, vol. 10, no 5, p. 528

[96] U. Gahlaut, V. Kumar, R. Pandey, Y.J.O. Goswami, Highly luminescent ultra small Cu doped ZnO nanostructures grown by ultrasonicated sol – gel route. Optik , 2016, vol. 127, no 10, p. 4292-4295.

[97] M.A. Sliem, S. Turner, D. Heeskens, S.B. Kalidindi, G. Van Tendeloo, M. Muhler, R.A. Fischer, Preparation, microstructure characterization and catalytic performance of Cu/ZnO and ZnO/Cu composite nanoparticles for liquid phase methanol synthesis. Physical Chemistry Chemical Physics, 2012, vol. 14, no 22, p. 8170-8178.

[98] S.D. Lin, H. Cheng, T.C. Hsiao, In situ DRIFTS study on the methanol oxidation by lattice oxygen over Cu/ZnO catalyst. Journal of Molecular Catalysis A: Chemical, 2011, vol. 342, p. 35-40.

[99] D. Bouras, A. Mecif, R. Barillé, A. Harabi, M. Rasheed, A. Mahdjoub, M. Zaabat, Cu: ZnO deposited on porous ceramic substrates by a simple thermal method for photocatalytic application. Ceramics International, 2018, vol. 44, no 17, p. 21546-21555.

[100] A. Levasseur, P. Vinatier, D. Gonbeau, X-ray photoelectron spectroscopy: A powerful tool for a better characterization of thin film materials. Bulletin of Materials Science, 1999, vol. 22, no 3, p. 607-614.

[101] G.H. Major, N. Fairley, P.M.A. Sherwood, M.R. Linford, J. Terry, V. Fernandez, K. Artyushkova, Practical guide for curve fitting in x-ray photoelectron spectroscopy. Journal of Vacuum Science & Technology A: Vacuum, Surfaces, and Films, 2020, vol. 38, no 6, p. 061203.

[102] F.A. Stevie, R. Garcia, J. Shallenberger, J.G. Newman, C.L. Donley, Sample handling, preparation and mounting for XPS and other surface analytical techniques. Journal of Vacuum Science & Technology A: Vacuum, Surfaces, and Films, 2020, vol. 38, no 6, p. 063202.

[103] P.K. Reddy Boppidi, P. Joshna, D. Som, R. H, P. Biswas, D. Bhattacharyya, S. Kanungo, S. Banerjee, S. Kundu, Understanding the efficacy of Cu in creating oxygen vacancies and temperature dependent electrical transport in solution processed Cu: ZnO thin films. Materials Science in Semiconductor Processing, 2020, vol. 120, p. 105311.

[104] H. Yuan, M. Xu, Q.Z. Huang, Effects of pH of the precursor sol on structural and optical properties of Cu-doped ZnO thin films. Journal of alloys and compounds, 2014, vol. 616, p. 401-407.

[105] M. Caglar, F. Yakuphanoglu, Structural and optical properties of copper doped ZnO films derived by sol – gel. Applied Surface Science , 2012, vol. 258, no.7, p. 3039-3044.

[106] M.h. Guezzoul, M.h. Bouslama, A. Ouerdane, A. Mokadem, B. Kharroubi, M. Bedrouni, M. Abdelkrim, A. Abdellaoui, K.B. Bensassi, A. Baizid, M.S. Halati, Chemical, morphological and optical properties of undoped and Cu-doped ZnO thin films submitted to UHV treatment. Applied Surface Science, 2020, vol. 520, p. 146302

[107] D.R. Miller, S.A. Akbar, P.A. Morris, Nanoscale metal oxide-based heterojunctions for gas sensing: a review. Sensors and Actuators B: Chemical, 2014, vol. 204, p. 250-272.

[108] S. Park, C.-H. Kim, W.-J. Lee, S. Sung, M.-H. Yoon, Sol-gel metal oxide dielectrics for all-solution-processed electronics. Materials Science and Engineering: R: Reports, 2017, vol. 114, p. 1-22.

[109] A.B. Djurišić, Y.H. Leung, A.M.C. Ng, Strategies for improving the efficiency of semiconductor metal oxide photocatalysis. Materials Horizons, 2014, vol. 1, no 4, p. 400-410.

[110] V.I. Anisimov, F. Aryasetiawan, A. Lichtenstein, First-principles calculations of the electronic structure and spectra of strongly correlated systems: the LDA+ U method. Journal of Physics: Condensed Matter, 1997, vol. 9, no 4, p. 767.

[111] M. Yaakob, N. Hussin, M. Taib, T. Kudin, O. Hassan, A. Ali, M. Yahya, First principles LDA+ U calculations for ZnO materials. Integrated Ferroelectrics, 2014, vol. 155, no 1, p. 15-22.

[112] J.-Q. Wen, J.-M. Zhang, Z.-G. Qiu, X. Yang, Z.-Q. Li, The investigation of Ce doped ZnO crystal: the electronic, optical and magnetic properties. Physica B: Condensed Matter , 2018, vol. 534, p. 44-50.

[113] Q. Hou, D. Xi, W. Li, X. Jia, Z. Xu, First-principles research on the optical and electrical properties and mechanisms of In-doped ZnO. Physica B: Condensed Matter, 2018, vol. 537, p. 258-266.

[114] Z. Ma, F. Ren, X. Ming, Y. Long, A.A. Volinsky, Cu-doped ZnO electronic structure and optical properties studied by first-principles calculations and experiments. Materials, 2019, vol. 12, no 1, p. 196.

[115] F. Li, C. Zhang, M. Zhao, Magnetic and optical properties of Cu-doped ZnO nanosheet: First-principles calculations. Physica E: Low-dimensional Systems and Nanostructures, 2013, vol. 53, p. 101-105.

[116] L. Chen, S. Li, Y. Cui, Z. Xiong, H. Luo, Y. Gao, Manipulating the electronic and magnetic properties of ZnO monolayer by noble metal adsorption: a first-principles calculations. Applied Surface Science, 2019, vol. 479, p. 440-448.

[117] A.K. Nayek, H. Luitel, B. Haldar, D. Sanyal, M. Chakrabarti, Ferromagnetic property of copper doped ZnO: A first-principles study. Computational Condensed Matter, 2020, vol. 23, p. e00455

[118] D. Fang, A. De Sarkar, R. Zhang, First-principles study on the origin of ferromagnetism in n-type Cu-doped ZnO. Solid state communications, 2012, vol. 152, no 12, p. 1057-1060.

[119] C. Feng, Z. Chen, W. Li, F. Zhang, X. Li, L. Xu, M. Sun, First-principle calculation of the electronic structures and optical properties of the metallic and nonmetallic elements-doped ZnO on the basis of photocatalysis. Physica B: Condensed Matter, 2019, vol. 555, p. 53-60.

[120] S. Sriram, K. Lalithambika, A. Thayumanavan, Experimental and theoretical investigations of photocatalytic activity of Cu doped ZnO nanoparticles. Optik, 2017, vol. 139, p. 299-308.

[121] Q. Wang, J. Wang, X. Zhong, Q. Tan, Y. Zhou, The magnetic phase transition in Cu-doped ZnO: From bulk to nanocluster. Solid state communications, 2012, vol. 152, no 1, p. 50-52.

[122] Z. Long, L. Peng-Fei, Y. Zhong-Yuan, L. Yu-Min, W. Dong-Lin, Y. Han, First-principles study of electronic and optical properties in wurtzite Zn1–xCuxO. Chinese Physics B, 2010, vol. 19, no 5, p. 056104.

[123] B.-S. Kang, K.-S. Kim, S.-C. Yu, H. Chae, First-principles study for ferromagnetism of Cu-doped ZnO with carrier doping. Journal of Solid State Chemistry , 2013, vol. 198, p. 120-124.

[124] V. Mendoza-Estrada, A. González-García, D. Barragán-Yani, W. López-Pérez, J. Rivera-Julio, R. González-Hernández, Ferromagnetic orderings in CoxCuyZn1−(x+ y) O by GGA and GGA+ U formalisms within density functional theory. Computational Materials Science, 2017, vol. 126, p. 344-350.

[125] P. Erhart, A. Klein, K. Albe, First-principles study of the structure and stability of oxygen defects in zinc oxide. Physical Review B, 2005, vol. 72, no 8, p. 085213.

[126] S. Clark, J. Robertson, S. Lany, A. Zunger, Intrinsic defects in ZnO calculated by screened exchange and hybrid density functionals. Physical Review B, 2010, vol. 81, no 11, p. 115311.

[127] F. Oba, M. Choi, A. Togo, I.Tanaka , Point defects in ZnO: an approach from first principles. Science and Technology of Advanced Materials, 2011.

[128] G. Qin, X. Wang, J. Zheng, C. Kong, B.J.C.m.s. Zeng, First-principles investigation of the electronic and magnetic properties of ZnO nanosheet with intrinsic defects. Computational materials science , 2014, vol. 81, p. 259-263.

[129] A. Boukhari, B. Deghfel, A. Mahroug, R. Amari, N. Selmi, S. Kheawhom, A.A. Mohamad, Thickness effect on the properties of Mn-doped ZnO thin films synthesis by sol-gel and comparison to first-principles calculations. Ceramics International, 2021, vol. 47, no 12, p. 17276-17285.

[130] M. Xu, H. Zhao, K. Ostrikov, M. Duan, L.X.Xu, Effect of doping with Co and/or Cu on electronic structure and optical properties of ZnO. Journal of Applied Physics, 2009, vol. 105, no 4, p. 043708.

[131] V. Mendoza-Estrada, W. López-Pérez, R. González-Hernández, A.González-García, Electronic structure and magnetic order in CuxZn (1− x) O: A study GGA and GGA+ U. Physica B: Condensed Matter, 2019, vol. 557, p. 74-81.

[132] M.N.H. Liton, A.K.M.F.U. Islam, M. Kamruzzaman, M.K.R. Khan, M. Al Helal, M.M. Rahman, Dual acceptor (N, Cu) doping effects on the electronic and optical properties of ZnO. Materials Chemistry and Physics, 2020, vol. 242, p. 122463.

[133] J. Dai, Z. Suo, Z. Li, S. Gao, Effect of Cu/Al doping on electronic structure and optical properties of ZnO. Results in Physics, 2019, vol. 15, p. 102649.

[134] X.Y. Deng, G.H. Liu, X.P. Jing, G.S. Tian, On-site correlation of p-electron in d10 semiconductor zinc oxide. International Journal of Quantum Chemistry, 2014, vol. 114, no 7, p. 468-472.

[135] K. Harun, N.A. Salleh, B. Deghfel, M.K. Yaakob, A.A.J.R.i.P. Mohamad, DFT+ U calculations for electronic, structural, and optical properties of ZnO wurtzite structure: A review. Results in Physics, 2020, vol. 16, p. 102829..

[136] X. Ma, Y. Wu, Y. Lv, Y. Zhu, Correlation effects on lattice relaxation and electronic structure of ZnO within the GGA+ U formalism. The Journal of Physical Chemistry C, 2013, vol. 117, no 49, p. 26029-26039.

[137] P. Nozieres, D. Pines, Electron interaction in solids. Characteristic energy loss spectrum. Physical Review, 1959, vol. 113, no 5, p. 1254.

CHAPTER II:

Experimental background

II.1. Metal oxides nanomaterials

II.1.1. Introduction

Thin film technology is both an ancient art and a relatively new science. The use of thin films extends back to the metal ages of antiquity **[1]**. In recent years, many researchers have focused on studying the properties of thin films due to the easy and versatility of their manufacturing methods, especially the chemical ones, as well as their various potential applications in many technological devices.

II.1.2. Thin film definition

A thin layer of a given substance is the material deposited on a substrate, one of its dimensions, called thickness, is greatly reduced so that it is expressed in nanometer and becomes quasi-two-dimensional material. This affects the majority of the physical properties of thin films, for which, on the contrary for a bulk, one can not neglect the effect of the boundary surfaces of materials. It's worth noting that the thinner the layer, the stronger the two-dimensional effect **[2]**.

II.1.3. Thin film growth mechanisms

According to the observations of films evaporating **[3]**, film growth can be divided into steps: : **(i)** nucleation, where a small nuclei are formed which are statistically distributed over the substrate surface, **(ii)** growth of the nuclei and formation of larger islands, which often have the shape of small crystals (crystallites), **(iii)** coalescence of the islands (crystallites) and formation of a more or less connected network containing empty channels, **(iv)** filling of the channels **[4]**.

II.1.4. Thin film growth modes

Both experiment and theory of deposition at different stages of growth, have shown that three distinguishable modes of growth and nucleation can occur: **(i)** Volmer– Weber model, **(ii)** Frank–Van der Merwe model and **(iii)** Stranski–Krastanov **[5]**.

II.1.4.1. The Frank-Van der Merve mode

Frank–Van der Merwe growth (FM), or also known as 'layer-by-layer growth' is the preferred growth model for obtaining smooth films **[6]**, which grow epitaxially at a surface or interface of crystal. In FM two-dimensional (2D) growth mode, interaction between film atoms and substrate surface is greater than between neighbouring film atoms.

II.1.4.2. The Volmer-Weber mode

When the atoms of a depositing films are more tightly coupled to each other than to the substrate, the Volmer-Weber growth mode (VW) occurs. In this situation, three-dimensional (3D) islands nucleate and grow directly on the surface of the substrate **[7]**.

II.1.4.3. The Stranski-Krastanov mode

Stranski-Krastanov growth mode (SK growth mode) is an intermediate case between the preceding two modes (FM and VW), it is also called "the layer-plus-island growth mode". In this last mechanism, after the formed the two-dimensional layer, growth continues, forming 3D islands. **Figure II.1** shows the mechanism of these three growth modes.

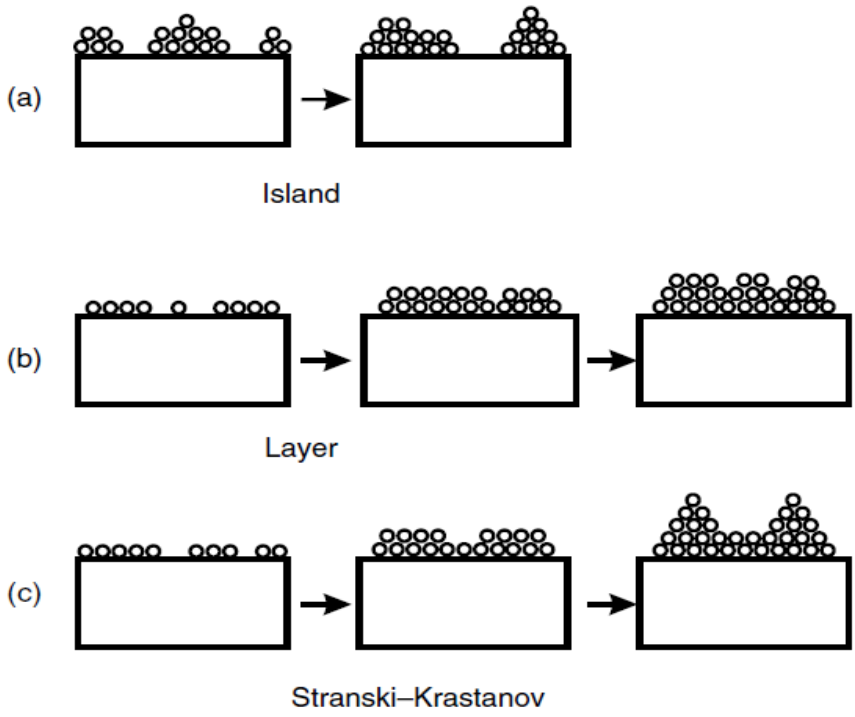

Figure II.1. Growth modes of film; **(a)** Volmer–Weber island growth **(b)** Frank–Vander Merwe layer growth and **(c)** Stranski-Krastanov layer plus island growth **[5]**.

II.1.5. Nanotechnology and nanostructured thin films

Nanotechnology is a field of innovation and development interested with the design, manufacture, and application of structures and devices by controlling their shape and size at a nanoscale as well as the fundamental understanding of the effect of material dimensions on physical properties or phenomena. Nanomaterials are of interest because they exhibit unique optical, magnetic, electrical, and other properties at such a small scale **[8]**. Nanoscale brings about giving rise to quantum phenomena that give materials new properties.

II.1.5.1. Quantum confinement

The most common effect in the nanoworld is known as quantum confinement. In this effect, the atomic structure changes due to the reduction of the nanometric scale. The quantum confinement effect produces an increase in the excitonic transition energy and a blue shift in the absorption and luminescence band gap energy as the particle size approaches the Bohr exciton radius **(Figure II.2) [9].**

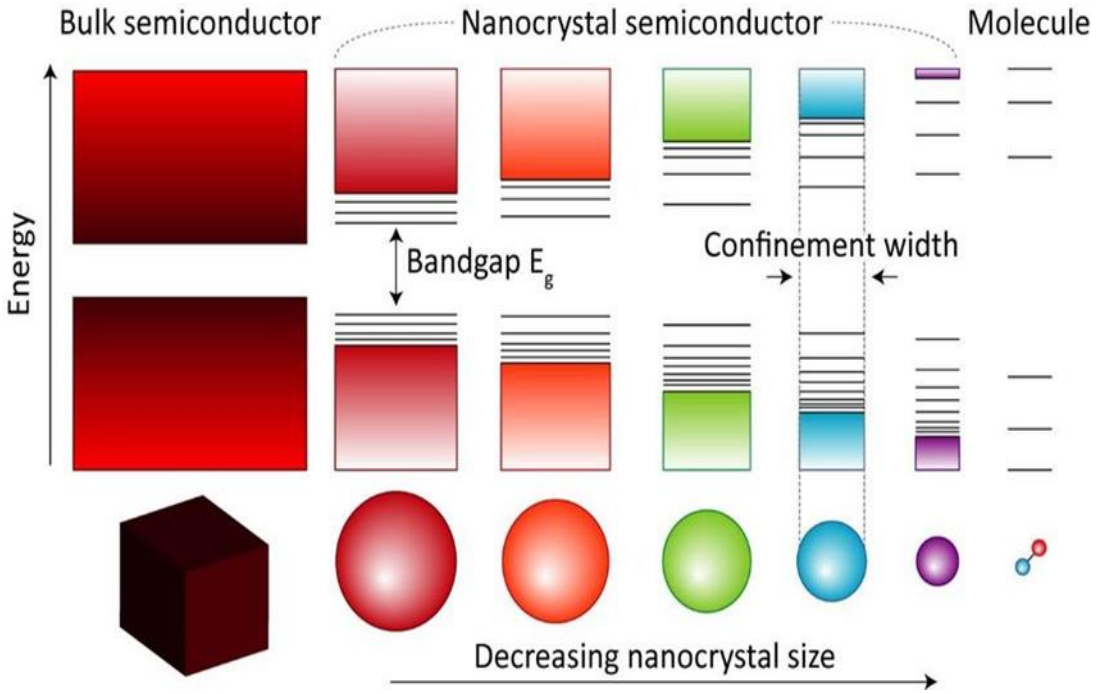

Figure II.2. Quantum confinement effect. Comparison of bulk, nanocrystals and molecules**[10] .**

II.1.5.2. Spatial confinement

Spatial confinement reflects the fact that the probability of having a defect inside a particle decreases sharply when the size becomes less than the average distance between two defects in the bulk material. In silicon, a pair of electron-hole can de-excite in two ways, either radiatively by emitting a photon of energy corresponding to the gap of the material, or non-radiatively on a crystal defect. Even for pure silicon, the second process dominates because the radius of capture of the defects is enormous (~ μm) **[2].**

II.1.5.3. Surface effects

When the particle size significantly decreases, the surface -volume ratio increases. As an example, we refer to the materials used in applications in catalysis and detection, for which a very large specific surface area is exhibited. In the case of doped materials, increasing the surface area- volume ratio greatly increases the probability of finding the dopant on the surface. This significantly increases the efficiency of doping **[2]**.

II.1.6. General properties of zinc oxide

ZnO has three main crystalline structures, hexagonal wurtzite, cubic zincblende and rocksalt (**Figure II.3**). The wurtzite structure is the most thermodynamically stable phase. Thus, the wurtzite structure type is obtained by alternate stacking along the c direction (c-axis) of two interpenetrating hexagonal-closed-pack (HCP) sub lattices. The until cell of sub lattices forms a tetrahedron structure which consists of 5 atoms; one atom belongs to zinc (cation) and is surrounded by 4 oxygen atoms(anions) and vice versa. Moreover, the ZnO wurtzite phase has a polar hexagonal axis known as the c-axis (0002) that is parallel to the z-axis and the other is the nonpolar plane and includes $(11\bar{2}0)$ and the $(10\bar{1}0)$. The nonpolar surface has a higher surface energy compared to the polar surface. At room temperature (RT), the lattice parameters of ZnO wurtzite structure are found to be around of $a = b = 3.2496$ Å, $c = 5.2042$ Å and $\beta = 120°$, with a ratio of $c/a = 1.601$ which is close to that of an ideal compact hexagonal structure (c/a =1.633), The point group is C6v (6 mm) and the space group is P63mc in Schoenflies notation and in Hermann–Mauguin notation **[11]**.

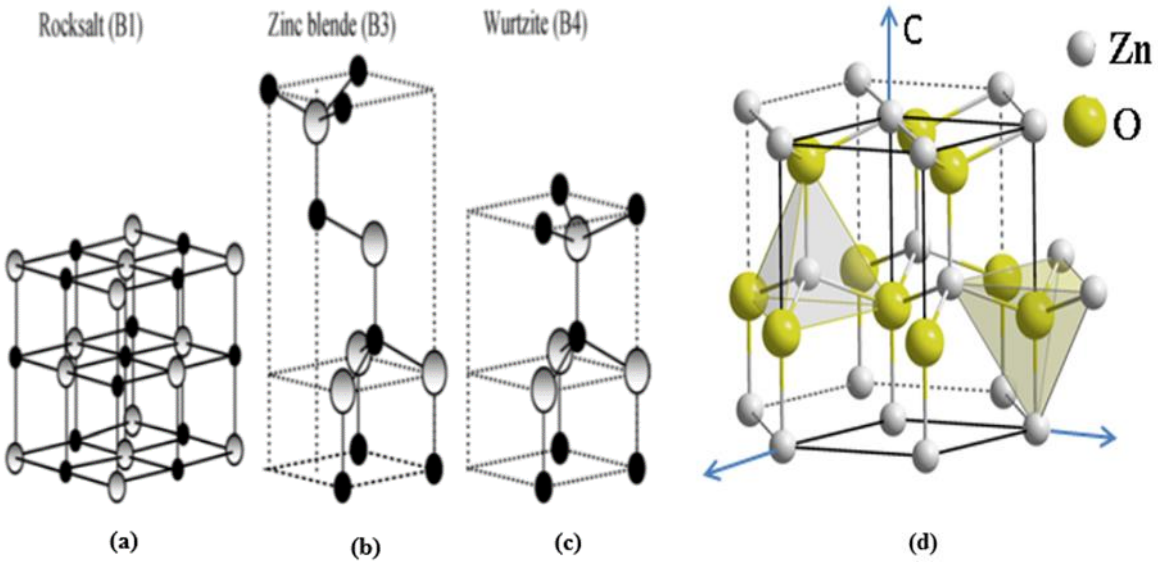

Figure II.3. Stick-and-ball representation of ZnO crystal structures: **(a)** cubic rocksalt, **(b)** cubic zinc blende, and **(c)** hexagonal wurtzite. Shaded grey and black spheres denote Zn and O atoms, respectively and **(d)** The hexagonal wurtzite structure (HCP-type) of the ZnO semiconductor **[2]**.

II.2. Sol gel technique

II.2.1 Introduction

Figure II.4 displays the schematic illustration of different routes in the sol-gel process providing various types of substances. By evaporating the liquid phase from the gel phase, xerogels are generated, while aerogels are created by solvent extraction under supercritical conditions. The films are prepared by a coating of the precursor solution on the substrates by means of dipping, spinning, or spraying. The solvent is eliminated during the deposition and subsequent drying process, resulting in densification of the films. Heat treatment is substantial to realize the target oxide composition and structural features.

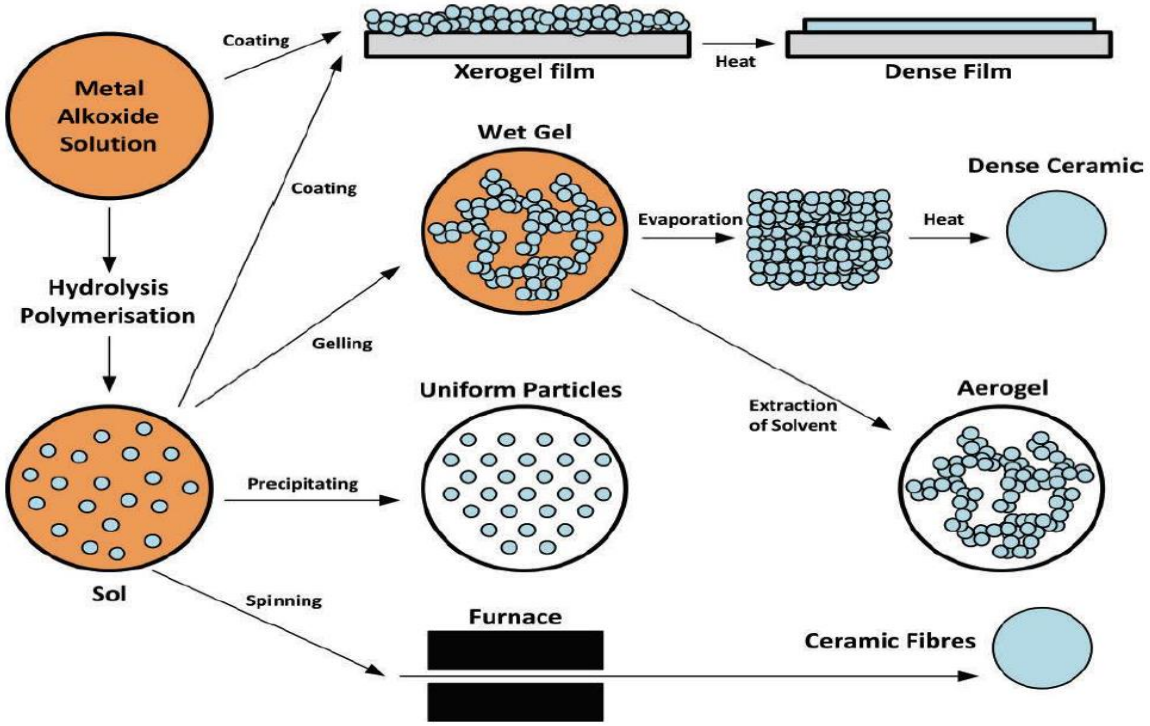

Figure II.4. Synthesis of various forms of materials by the sol-gel process **[12]**.

In the solution state, the main goal is to obtain strong homogeneity in the precursor mixture, which has significant advantages for producing a pure-phase product and can also result in lower synthesis temperatures **[13]**.The main steps of thin film preparation by the sol-gel process involve the elaboration of the precursor solution, deposition of the prepared sol on the substrate by the selected technique, and the heat treatments of the deposited films. In general, numerous parameters affect the preparation of thin films like the nature, molarty, and concentration of the chosen precursor, the choice of solvent and additives, the coating technique and deposition parameters, the nature of the substrate, and the heat treatment conditions.

Generally, the metal alkoxides of the general formulas $M(OR)_n$ are the precursors most often used in the sol-gel process, where **M** denotes a metal of valence n and R is an alkyl chain of type ($-C_nH_{2n+1}$). They can have high solubility and very high purity in a wide range of organic solvents. The synthesis, the reaction behavior, and the physical properties of the alkoxides have been extensively studied **[14,15]**, therefore, only the main characteristics necessary for understanding the reactions of alkoxides in solution will be recalled.

II.2.2. Chemical reactions

From a chemical point of view, the formation of oxide is the result of a complex succession of interconnected reactions. The basis of the synthesis is the two fundamental reactions regulating the entire sol-gel process, namely hydrolysis of the metal precursor and condensation to form the oxide network.

II.2.2.1. Hydrolysis

It is a reaction between a molecule of water and an alkoxide, allowing the releasing of a molecule of alcohol in three steps illustrated in **figure II.5**:

In order to condense the alkoxides at room temperature, the hydrolysis of the **-OR** groups must begin the reaction process. This step is necessary to give rise to the hydroxyl groups **-OH**:

- The fixing of a molecule of water on the metal atom M.
- Transfer of proton from the water molecule.
- The departure of an R-OH groups carried out by a balanced reaction process.

In a neutral condition, the reaction is written as **[16 ,17]** :

M-(OR)n+ H2O → OH-M-(OR)n-1 + R-OH

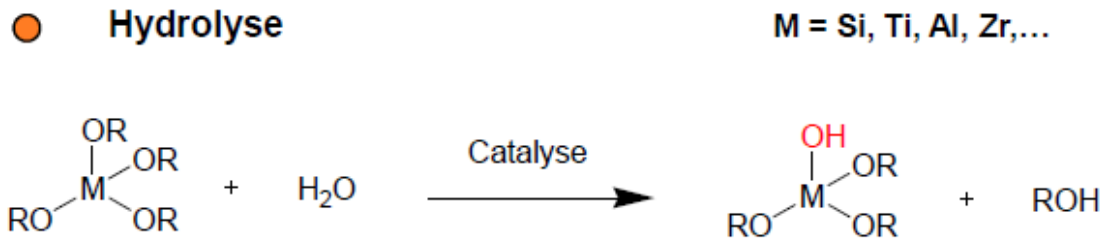

Figure II.5. Hydrolysis Mechanism of alkoxides M-$(OR)_n$ **[17]**.

This reaction can be influenced by the following parameters:

- The catalyst is acidic or basic.
- The nature of the solvent.
- The amount of water relative to the alkoxide ([H2O] / [alkoxide]).
- The temperature.

II.2.2.2. Condensation

The condensation reactions begin after the appearance of the hydroxyl groups and lead to the formation of bonds or metalloxane bridge "M-O-M". The condensation mechanism reaction may take place between the different groups. The reaction of the groups (OH-M- $(OR)_{n-1}$) gives a water molecule (the oxolation) as:

$$\mathbf{OH\text{-}M\text{-}(OR)_{n-1} + OH\text{-}M\text{-}(OR)_{n-1} \rightarrow (OR)_{n-1}\text{-}M\text{-}O\text{-}M\text{-}(OR)_{n-1} + H2O}$$

The reaction of the groups (OH-M- (OR) n-1) with remaining non-hydrolyzed groups MOR give a molecule of alcohol R-OH (the alkoxolation) as follows:

$$\mathbf{OH\text{-}M\text{-}(OR)_{n-1} + M\text{-}(OR)_{n} \rightarrow (OR)_{n-1}\text{-}M\text{-}O\text{-}M\text{-}(OR)_{n-1} + R\text{-}OH}$$

The condensation reaction mechanism is concerning to the hydrolysis reaction. Therefore, the hydrolysis parameters are also affecting the mechanism and kinetics of the reaction of condensation and, consequently, the characteristics of the obtained gel**[18]**.

II.2.3. The sol-gel transition

Growing polymer chains that agglomerate by condensation and form clusters are the most common gelation scheme. During the progression of the hydrolysis and condensation reactions, polymeric clumps, the size of which grows with time, are formed. When one of these clusters achieves an infinite size, the viscosity also becomes infinite: this is the sol-gel transition point. From this point, the infinite cluster known as the "gel fraction" expands by incorporating smaller polymeric groups. The gel is created after all of the bonds have been used **[19] .**

The evolution of a sol's viscosity and Coulomb modulus as a function of time are presented schematically in **figure II.6**. When the gel is completely formed, the viscosity becomes infinite, while the elastic constant tends to its maximum value. The solid cluster created by the base solution can then be viewed as the interleaving of polymeric chains forming a disordered solid structure. There are still trapped liquid masses in this structure. Evaporation is used to remove them**[20].**

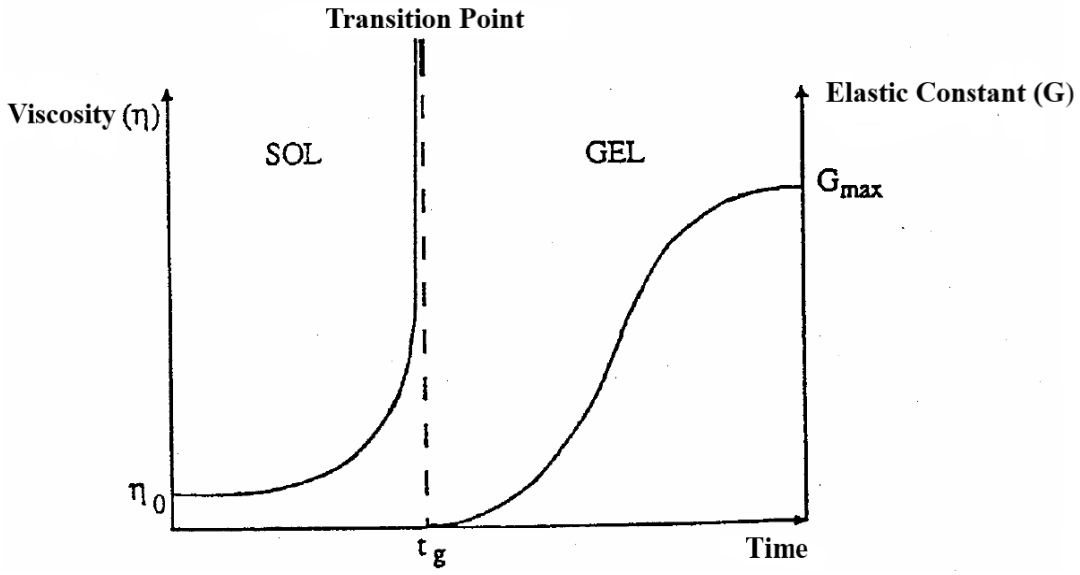

Figure II.6. Evolution of the viscosity of the solution and the elastic constant of the gel. The point **tg** corresponds to the time at the end of which the transition sol gel is reached **[19]**.

Besides, like all chemical reactions, the sol-gel transition is sensitive to its environment, such as temperature or humidity, which can thus, depending on its nature, modify the kinetics of the reactions.

II.2.4. Sol pH (Choice of catalyst)

Because of the mechanisms involved in gelation, the pH will play a significant role in the evolution of reactions. Indeed, the $\mathbf{OH^-}$ and $\mathbf{H_3O^+}$ions do not have the same influence on the reactions (hydrolysis and condensation). The $\mathbf{H_3O^+}$ cation, attracted by oxygen, facilitates the substitution of the **OR** groups and thus hydrolysis, whereas the $\mathbf{OH^-}$anion, attracted by the electronegative metal **M**, favours the formation of **M-O-M** bonds by condensation. So, a basic medium accelerates condensation, while an acidic medium promotes hydrolysis (**Figure II.7) [21]**. Catalysis thus acts directly on the shape of the substance developed. This factor will also significantly influence the porosity of the final substance, hence, which partially condition the physical properties.

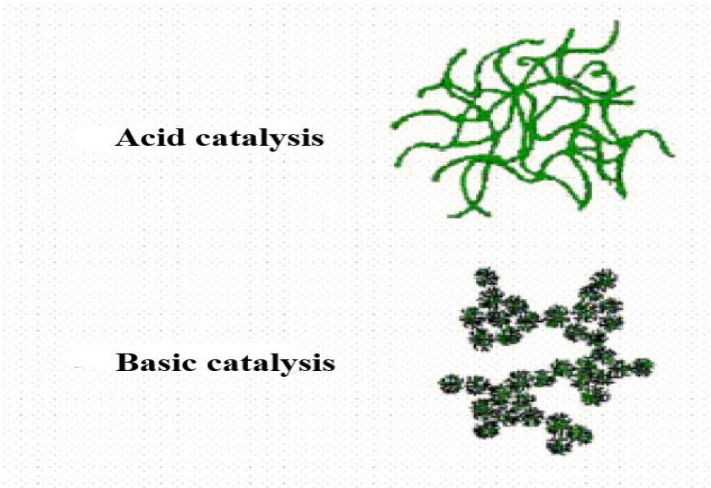

Figure II.7. Acid catalysis promotes hydrolysis and leads to the formation of longitudinal fibres. An increase in condensation generated by basic catalysis leads to clusters,characterized by a spherical shape **[22]**.

II.3. Elaboration of copper doped zinc oxide thin films

II.3.1. Sol-gel spin-coating process

The sol-gel spin-coating technique has been usually used to synthesis copper doped zinc oxide thin films with high purity and homogeneity. **Figure II.8** shows schematically the preparation steps of pure ZnO and Cu doped ZnO thin films by sol-gel-spin coating method. This technique includes several steps:

- Preparation of substrates.
- Chemical preparation of the solution to acquire the liquid (Sol).
- Deposition of solution on the substrate.
- Annealed thin films to achieve in the desired crystallized and densified material.

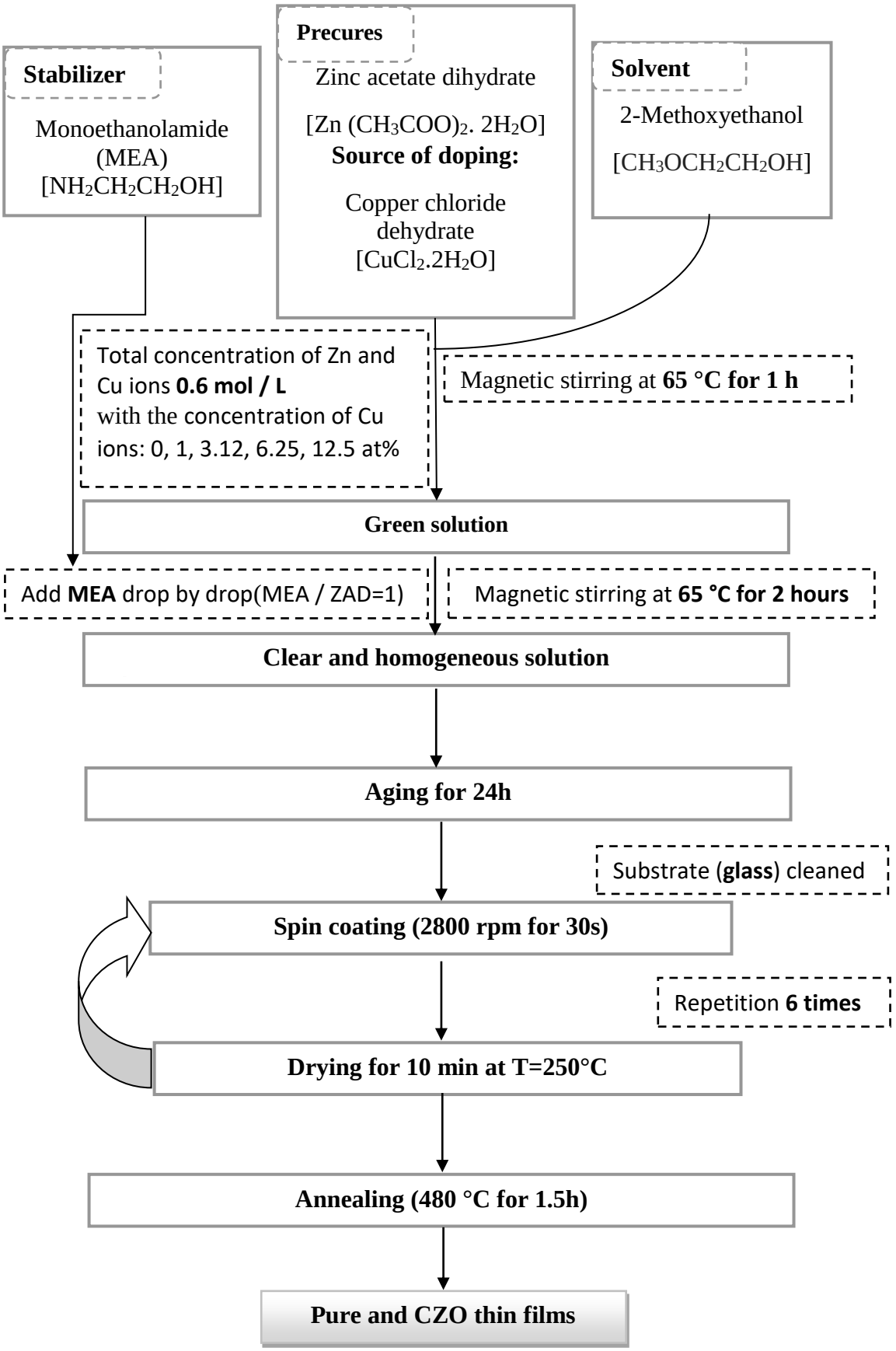

Figure II.8. Preparation steps of pure and Cu doped ZnO(CZO) thin films by sol-gel-spin.

II.3.2. The chemical elements used in the preparation of the solution

In order to prepare starting solutions, several chemical components are used. The most important chemical and physical properties of such components are summarized in the following section:

a) Zinc acetate dihydrate: as a precursor.

Formula**: [Zn ($CH_3COO)_2$. $2H_2O$]**.

Form**:** Solid.

Color**:** White.

Melting point**:** 237 °C.

Molar mass**:** 219.49 g/mol.

Density at 20 °C**:** 1.74 g/cm³.

Solubility in water at 20 °C**:** 430 g/l.

b) Copper chloride dihydrate: as a copper dopant source.

Formula**: [$CuCl_2$.$2H_2O$].**

Form**:** Solid.

Color**:** light blue.

Melting point**:** 895 °C.

Molar mass**:** 84.075 g/mol.

Density at 20 °C: 3.082 g/cm³.

Solubility in water at 20 °C**:** 484 g/l.

c) 2-Methoxyethanol: Alcohol as a solvent.

Formula**: $CH_3OCH_2CH_2OH$.**

Form**:** Liquid.

Color**:** Colorless.

Molar mass**:** 76.09 g/mol.

Density**:** 0.965 g/cm³.

Boiling point**:** 124 to 125 °C.

d) 2-Monoethanolamine -MEA: as a stabilizer or additive.
Formula**:** **$NH_2CH_2CH_2OH$.**

Form**:** Liquid.

Color**:** Colorless to yellow.

Molar mass**:** 61.08 g/mol.

Density**:** 1.01 g/cm³.

Boiling point**:** 170 °C.

II.3.3. Preparation of solutions

In the present work, solution **(sol)** with a molar concentration of 0.6 mol/l were prepared by dissolving zinc acetate dihydrate [Zn $(CH_3COO)_2$. $2H_2O$] in the solvent of 2-Methoxyethanol. After 30 minutes of magnetic stirring, the monoethanolamine-MEA, with a molar ratio (MEA / ZAD=1) was added. This stabilizer increases the solubility of zinc acetate in the solvent and leads to a transparent solution. The obtained solution is then brought to magnetic stirring again at 65 °C for 2 hours to becomes clear and homogeneous. Finally, it was then aged at room temperature for a day **[23, 27].**

For synthesis Cu doped ZnO solutions with different concentrations of dopant (x= 1%, 3.12%, 6.25%, 12.5 at%), we followed the same process as for the preparation of the pure solution. Copper (II) chloride [$CuCl_2.2H_2O$], Zinc acetate dihydrate [Zn $(CH3COO)_2$. $2H_2O$], MEA and 2-Methoxyethanol were used as a dopant source, starting material stabilizer and solvent, respectively. The concentration of metal ions was fixed at 0.6 M and the molar ratio of the solvent (Monoethanolamine-MEA) to metal ions was 1.0. After stirring at 65 °C for 2h, the solution was then aged at room temperature for 24 h.

To ensure the deposition of CZO thin films on clean glass substrates, these latter were cleaned in ethanol and acetone for 10 min each by using an ultrasonic cleaner and then washed with deionized water and dried.

II.4. Conclusion

This chapter gives the various modes for thin film growth, presents a general description of the sol-gel process and describes the experimental spin coating technique used to prepare thin films. It also discuss the elaboration protocol of undoped ZnO and Cu doped ZnO thin films at different concentrations.

References

[1] H. S. Nalwa, Nanostructured materials and nanotechnology: concise edition. Elsevier, 2001.

[2] A. Mahroug, "Etude des couches minces d'Oxyde de Zinc dopé Aluminium et Cobalt élaborées par la technique sol gel-spin coating.," 2015.

[3] L. Znaidi, Sol–gel-deposited ZnO thin films: A review, Mater. Sci. Eng. B, vol. 174, no. 1–3, p. 18–30, 2010.

[4] S. Abdullahi, RF Sputtered Zinc Oxide (ZnO) Thin Films: A Review. *East African Scholars Multidiscip. Bull.*, 2019, vol. 2, p. 75-82.

[5] K. S. Harsha, Principles of vapor deposition of thin films. Elsevier, 2005.

[**6]** E. Alfonso, J. Olaya, and G. Cubillos, Thin film growth through sputtering technique and its applications. Crystallization-Science and technology, 2012, vol. 23, p. 11-12.

[**7]** C. I. Fornari, G. Fornari, H. D. O. Paulo, E. Abramof, and J. D. S. Travelho, Monte Carlo Simulation of Epitaxial Growth. *Epitaxy*, 2018, p.113.

[8] A. Sarkar, S. Roy, C. K. Ghosh, and C. K. Sarkar, Nanoscience with Graphene, in Nanotechnology. CRC Press, 2017, p. 241–258.

[9] V. Arivazhagan, Investgation of Quantum Confinement Effect in pbse znse multiple Quantum Well Structures Prepared by Thermal Evaporation technique, 2013.

[10] J. McKittrick and L. E. Shea-Rohwer, down conversion materials for solid-state lighting. Journal of the American Ceramic Society, 2014, vol. 97.5, p. 1327-1352.

[11] C. Jagadish and S. J. Pearton, Zinc oxide bulk, thin films and nanostructures: processing, properties, and applications. Elsevier, 2011.

[12] C. J. Brinker and G. W. Scherer, Sol-gel science: the physics and chemistry of sol-gel processing. Academic press, 2013.

[13] A. E. Danks, S. R. Hall, and Z. Schnepp, The evolution of 'sol–gel' chemistry as a technique for materials synthesis. *Materials Horizons*, 2016, vol. 3.2, p. 91-112

[14] G. E. Coates, "Metal Alkoxides: by DC Bradley, RC Mehrotra and DP Gaur, Academic Press, London, New York, San Francisco, 1978, Elsevier, 1979.

[15] R. C. Mehrotra, Synthesis and reactions of metal alkoxides. Journal of Non-Crystalline Solids, 1988, vol. 100,n.1-3, p.1-15.

[16] F. Collignon, Cahier technologique sol-gel. Edité par Certech, 2008, p.0-140.

[17] T. Schneller, R. Waser, M. Kosec, and D. Payne, Chemical solution deposition of functional oxide thin films. Springer, 2013.

[18] A. Noua and R. Guemini, Preparation and characterization of thin films nanostructures based on ZnO and other oxides, 2019.

[19] S. Rabaste, Microcavités optiques élaborées par voie sol-gel: applications aux ions terre rare d'Eu3+ et aux nanocristaux semiconducteurs de CdSe. Université Claude Bernard-Lyon I, 2003.

[20] T. Gacoin, L. Malier, and J.-P. Boilot, Sol–gel transition in CdS colloids. Journal of Materials Chemistry, 1997, vol. 7.6, p.859-860.

[21] D. Gallagher and T. Ring, Sol--Gel Processing of Ceramic Films. Chimia, 1989, vol. 43.10, p. 298-304.

[22] F. Collignon, Cahier technologique Sol-Gel, Cent. ressources Technol. en Chim 2008.

[23] A. Boukhari, B. Deghfel, A. Mahroug, R. Amari, N. Selmi, A.A. Mohamad, Thickness Effect on the Properties of 4% Mn-Doped ZnO Thin Films Grown by Sol-Gel Spin Coating Deposition. In: Macromolecular Symposia. 2021, p. 2000235

[24] E. Benrezgua, B. Deghfel, A. Mahroug, M.K. Yaakob, A. Boukhari, R. Amari, S. Kheawhom, A.A.Mohamad, Experimental and theoretical studies on structural, morphological, electronic, optical and magnetic properties of Zn1-xCuxO thin films (0≤ x≤ 0.125). Materials Science in Semiconductor Processing, 2021, vol. 134, p. 106012

[25] A. MAHROUG, B. Mari, M. Mollar, I. Boudjadar, L. Guerbous, A. Henni, N. Selmi, Studies on structural, surface morphological, optical, luminescence and Uv photodetection properties of sol–gel Mg-doped ZnO thin films. Surface Review and Letters, 2019, vol. 26.03, p. 1850167.

[26] B. Deghfel, A. Mahroug, R. Amari, A. Boukhari, A. Bentabet, EXPERIMENTAL AND FIRST PRINCIPLES STUDY OF STRUCTURAL, ELECTRONIC AND OPTICAL PROPERTIES OF ZN 0.875 MN 0.125 O THIN FILM, International Conference on Advanced Materials and Systems (ICAMS), The National Research & Development Institute for Textiles and Leather-INCDTP, 2018, p. 185-188.

[27] A. Mahroug, R. Amari, A. Boukhari, B. Deghfel, E.Ben Rezgua, STUDIES ON STRUCTURAL, SURFACE MORPHOLOGICAL, OPTICAL, LUMINESCENCE AND UV PHOTODETECTION PROPERTIES OF SOL GEL OXIDES THIN FILMS, International Conference on Advanced Materials and Systems (ICAMS), The National Research & Development Institute for Textiles and Leather-INCDTP, 2018, p. 199-204.

CHAPTER III

Theory and computational method

III.1 Introduction

In practice, there are many diversity of physical phenomena due to the large variety of the system formation. The common way to studying a particular phenomenon is to build empirical or semi-empirical models for the well studied experimentally phenomenon or extending them to other phenomena. Consequently, the condensed matter physics from theoretical and/or computational point of view can become a difficult task to do. This makes the realization of accurate model severely limited due to the complexity of such systems.

The first principles approximation starts from what we know about condensed matter, which are made of atoms. The interactions between these atoms, made of nucleus with a positive charge and a negatively charged electrons, are determined by the interactions of their constituents. So, accurate knowledge on these basic interactions lead to improving the calculated physical and chemical properties of the system under study. The development of efficient model based on theoretical and computational methods for dealing with many body problems is therefore essential to the research in the condensed matter theory.

III.2 The many-body problem

A condensed matter system usually involves many interacting particles, i.e. nucleus and electrons. The many-body time independent Schrodinger equation describing their interaction can be written as:

$$\hat{H}\emptyset(\boldsymbol{r}_1, \boldsymbol{r}_2, \dots \boldsymbol{r}_N,\ \boldsymbol{R}_1, \boldsymbol{R}_2, \dots \boldsymbol{R}_M) = E\emptyset(\boldsymbol{r}_1, \boldsymbol{r}_2, \dots \boldsymbol{r}_N,\ \boldsymbol{R}_1, \boldsymbol{R}_2, \dots \boldsymbol{R}_M) \qquad \textbf{(III.1)}$$

where E and $\hat{H}$ is the total energy and the Hamiltonian operator of the system of N electrons and M nuclei, respectively, and $\emptyset(\boldsymbol{r}_1, \boldsymbol{r}_2, \dots \boldsymbol{r}_N,\ \boldsymbol{R}_1, \boldsymbol{R}_2, \dots \boldsymbol{R}_M)$ is the many-body wave function, which contains the quantum probability amplitude for every possible configuration of electrons and nuclei **[1]**. This latter is dependent on the coordinates of all electrons, with position $\boldsymbol{r}_i$, and nuclei, with position $\boldsymbol{R}_I$ and charge Z_I for spinless system **[2]**. In atomic units and without accounting for relativistic effects, the Hamiltonian $\hat{H}$ is then given by;

$$\hat{H} = -\frac{1}{2}\sum_{i=1}^{N}\nabla_{\boldsymbol{r}_i}^2 - \frac{1}{2}\sum_{I=1}^{M}\nabla_{\boldsymbol{R}_I}^2 + \frac{1}{2}\sum_{i=1}^{N}\sum_{j\neq i}^{N}\frac{1}{|\boldsymbol{r}_i - \boldsymbol{r}_j|} + \frac{1}{2}\sum_{I=1}^{M}\sum_{J\neq I}^{M}\frac{Z_I Z_J}{|\boldsymbol{R}_I - \boldsymbol{R}_J|} - \sum_{i=1}^{N}\sum_{I=1}^{M}\frac{Z_I}{|\boldsymbol{r}_i - \boldsymbol{R}_I|} \qquad \textbf{(III.2)}$$

where $\nabla^2_{\boldsymbol{r}_i}$ and $\nabla^2_{\boldsymbol{R}_I}$ is the Laplacian operator for the spatial coordinates of the *i*-th electron and *I*-th nucleus, respectively. The first term is the kinetic energy of *N* electrons with masses m_e and the second term is that of *M* nuclei with masses M_I, the third and fourth term is the electrostatic repulsion between electrons and the electrostatic repulsion between nuclei, respectively, and the last term is the Colombian attraction between electrons and nuclei.

Based on the fact that the nuclei are much heavier than the electrons and at lower temperatures (0 *K*), Born and Oppenheimer (1927) considered that the motion of nuclei can be neglected compared to that of the electrons, and the nuclei can then be considered stationary or fixed in space and the electrons remain in their ground state. This approximation is known as adiabatic approximation **[3]**. The many-body problem is therefore reduced to the system of electrons moving in some external potential due to the nuclei. Therefore, the second tem disappears and the fourth term, total nuclear energy (E_{ion}), reduces to a constant and is included in the total energy as:

$$E_{tot} = E + E_{ion} = E + \sum_{I=1}^{M} \sum_{J>I}^{M} \frac{Z_I Z_J}{|\boldsymbol{R}_I - \boldsymbol{R}_J|} \qquad \textbf{(III.3)}$$

Where E is the total electronic energy, which equals to the sum of the energies of all electrons; $E = \varepsilon_1 + \varepsilon_2 \ldots \varepsilon_N$. Furthermore, the total nuclear energy can be disregarded from Hamiltonian and it will be taken into account when needed.

In this case, the wave function can then be written as a product of an electronic wave function $\Psi(\boldsymbol{r}_1, \boldsymbol{r}_2, \ldots \boldsymbol{r}_N)$ and a nuclear wave function $\varphi(\boldsymbol{R}_1, \boldsymbol{R}_2, \ldots \boldsymbol{R}_M)$;

$$\emptyset = \Psi(\boldsymbol{r}_1, \boldsymbol{r}_2, \ldots \boldsymbol{r}_N)\, \varphi(\boldsymbol{R}_1, \boldsymbol{R}_2, \ldots \boldsymbol{R}_M) \qquad \textbf{(III.4)}$$

The Schrodinger equation for the many-electron wave function $\Psi(\boldsymbol{r}_1, \boldsymbol{r}_2, \ldots \boldsymbol{r}_N)$ in the presence of nuclei fixed, is then

$$\left(-\frac{1}{2} \sum_{i=1}^{N} \nabla^2_{\boldsymbol{r}_i} + \frac{1}{2} \sum_{i=1}^{N} \sum_{j \neq i}^{N} \frac{1}{|\boldsymbol{r}_i - \boldsymbol{r}_j|} - \sum_{i=1}^{N} \sum_{I=1}^{M} \frac{Z_I}{|\boldsymbol{r}_i - \boldsymbol{R}_I|} \right) \Psi(\boldsymbol{r}_1, \boldsymbol{r}_2, \ldots \boldsymbol{r}_N) = E\ \Psi(\boldsymbol{r}_1, \boldsymbol{r}_2, \ldots \boldsymbol{r}_N)$$

(III.5)

The measured energy, E, will be an upper bound to the ground state energy E_0 corresponding to the ground state Ψ_0 , *i.e.* $E[\Psi] \geq E_0$. This latter is obtained by the minimization of the functional $E[\Psi]$ with respect to all allowed *N*-electron wave functions which correspond to eigenvalues of the Hamiltonian $\hat{H}$ **[4, 5]**. The many-electron wave function $\Psi(\boldsymbol{r}_1, \boldsymbol{r}_2, \ldots \boldsymbol{r}_N)$ must be normalised,

$$\int d\boldsymbol{r}_1 \int d\boldsymbol{r}_2 \ldots . \int d\boldsymbol{r}_N \, \Psi^*(\boldsymbol{r}_1, \boldsymbol{r}_2, \ldots \boldsymbol{r}_N)\Psi \;\; (\boldsymbol{r}_1, \boldsymbol{r}_2, \ldots \boldsymbol{r}_N) = 1, \qquad \textbf{(III.6)}$$

and anti-symmetric under exchange of any two Fermions (electrons) coordinates, which are indistinguishable from one another,

$$\Psi \;\; (\boldsymbol{r}_1, \boldsymbol{r}_2, \ldots \boldsymbol{r}_N) = -\Psi \;\; (\boldsymbol{r}_2, \boldsymbol{r}_1, \ldots \boldsymbol{r}_N) \qquad \textbf{(III.7)}$$

Since the many-electron wave function has 3*N* degrees of freedom, the solution of Schrodinger equation is nearly impossible for realistic problem ($N \geq 3$). So, further approximations are required for making this problem tractable.

III.3 Wave function

To solve the Schrodinger equation for the many-electron wave function $\Psi(\boldsymbol{r}_1, \boldsymbol{r}_2, \ldots \boldsymbol{r}_N)$ (Eq. III.5), Hartree assumed that $\Psi(\boldsymbol{r}_1, \boldsymbol{r}_2, \ldots \boldsymbol{r}_N)$ can be written as a product of single electron wave functions, $\psi_i(\boldsymbol{r}_i)$ **[6]**,

$$\Psi(\boldsymbol{r}_1, \boldsymbol{r}_2, \ldots \boldsymbol{r}_N) = \prod_{i=1}^{N} \psi_i(\boldsymbol{r}_i) \qquad \textbf{(III.8)}$$

This is called ' Hartree approximation' made to the many-electron wave function.

The energy of the system can then be written from Eq. III.1 as

$$E = \langle \Psi | \hat{H} | \Psi \rangle \qquad \textbf{(III.9)}$$

Substitution of the obtained wave function into the above equation leads to **[2, 7]**;

$$E = -\frac{1}{2}\sum_{i=1}^{N} \langle \psi_i | \nabla^2 | \psi_i \rangle + \frac{1}{2}\sum_{i=1}^{N}\sum_{j\neq i}^{N} \left\langle \psi_i \psi_j \left| \frac{1}{|\boldsymbol{r}_i - \boldsymbol{r}_j|} \right| \psi_i \psi_j \right\rangle -$$

$$\sum_{i=1}^{N}\sum_{I=1}^{M} \left\langle \psi_i \left| \frac{Z_I}{|\boldsymbol{r}_i - \boldsymbol{R}_I|} \right| \psi_i \right\rangle \qquad \textbf{(III.10)}$$

Applying the variational principle on equation Eq.III.10, one can then obtain the *N* coupled one-electron Schrodinger equations,

$$\left(-\frac{1}{2}\nabla^2 - \sum_{I=1}^{M} \frac{Z_I}{|\boldsymbol{r} \;\; -\boldsymbol{R}_I|} + \sum_{j=1, j\neq i}^{N} \int \frac{|\psi_j(\boldsymbol{r}')|^2}{|\boldsymbol{r} - \boldsymbol{r}'|} d\boldsymbol{r}' \right) \psi_i(\boldsymbol{r}) = \varepsilon_i \psi_i(\boldsymbol{r}) \qquad \textbf{(III.11)}$$

where ε_i is Lagrange multiplier, which refers to the energy of *i*-th electron **[4, 8, 9]**. The last term in Eq. III.11 denotes the electrostatic repulsion between electrons, for which the fact that

the electron feels the electric fields of all the other electrons with a smooth charge density $\rho(\boldsymbol{r}) = \sum_{i=1}^{N} |\psi_i(\boldsymbol{r})|^2$, is adopted,

$$V_{e-e}(\boldsymbol{r}) \approx \sum_{j=1, j\neq i}^{N} V^H(\boldsymbol{r_j}) = \sum_{j=1, j\neq i}^{N} \int \frac{\rho(\boldsymbol{r'})}{|\boldsymbol{r}-\boldsymbol{r'}|} d\boldsymbol{r'} \qquad \textbf{(III.12)}$$

Where V^H is known as the Hartree potential or mean field approximation. The total wave function as a simple product is not antisymmetric and does not respect the Pauli's exclusion principle with respect to the exchange of electrons, which allowing to go beyond Hartree method **[9]**.

The one-electron Schrodinger equation (Eq. III.11) can be solved for each wave function $\psi_i(\boldsymbol{r})$ by using the self-consistent method which requires an initial choice of the other wave functions $\psi_j(\boldsymbol{r})$ **(Figure III.1)**. The self-consistency cycle is stopped when some convergence criterion is reached. These criteria are based on the difference of a given calculated parameter (energy, force, displacement, stress) from two successive iterations (i and i+1), i.e., $f_{i+1} - f_i$ is less than the user defined tolerance. On the other hand, if the criteria are not fulfilled, the self-consistency cycle restarts with a new density (mixing output density with the input density).

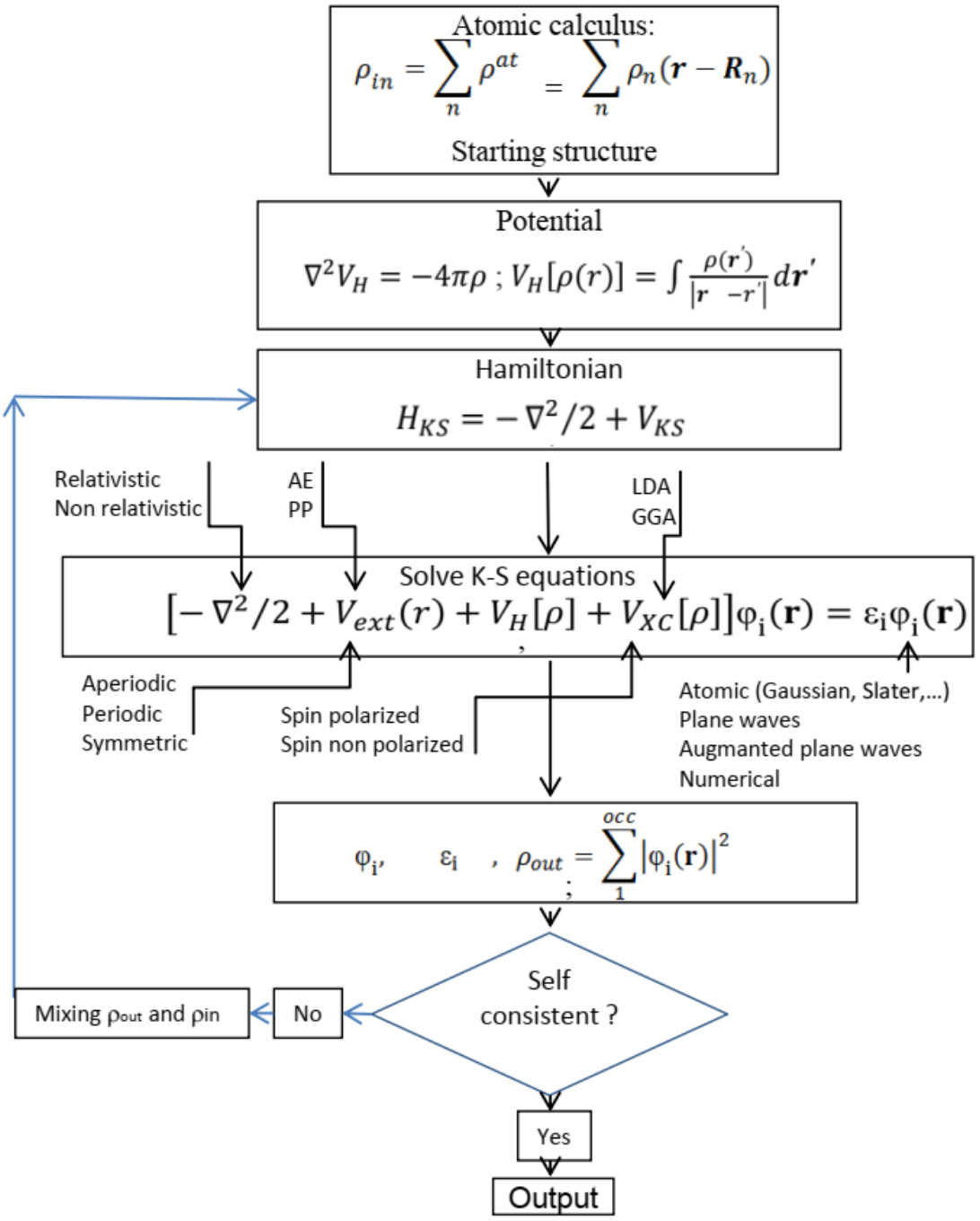

Figure III.1. Self-consistent resolution of the Kohn-Sham equations and the main existing choices of their various terms.

To make the wave function anti-symmetric with respect to the exchange of electrons, Fock **[10]** improved the Hartree model by adding and subtracting all possible permutations of the Hartree product (Eq.III.8), where the wave function is given by the Slater determinant as,

$$\Psi(\boldsymbol{r}_1, \boldsymbol{r}_2, \ldots \boldsymbol{r}_N) = \frac{1}{\sqrt{N!}} \begin{vmatrix} \psi_1(\boldsymbol{r_1}) & \psi_1(\boldsymbol{r_2}) & \cdots & \psi_1(\boldsymbol{r_N}) \\ \psi_2(\boldsymbol{r_1}) & \psi_2(\boldsymbol{r_2}) & \cdots & \psi_2(\boldsymbol{r_N}) \\ \vdots & \vdots & \ddots & \vdots \\ \psi_N(\boldsymbol{r_1}) & \psi_N(\boldsymbol{r_2}) & \cdots & \psi_N(\boldsymbol{r_N}) \end{vmatrix} \quad \textbf{(III.13)}$$

The interchange of two columns leads to changing the sign of the determinant which ensures the anti-symmetry property of the wave function **[6]**.

The last form of the wave function (Eq. III.13) gives rise to *N* one-electron Schrodinger equations, known as the Hartree-Fock (HF) equations,

$$\left(-\frac{1}{2}\nabla^2 - \sum_{I=1}^{M} \frac{Z_I}{|\boldsymbol{r} - \boldsymbol{R}_I|} + \int \frac{\rho(\boldsymbol{r}')}{|\boldsymbol{r}-\boldsymbol{r}'|} d\boldsymbol{r}'\right)\psi_i(\boldsymbol{r}) - \sum_{j=1}^{N} \int d\boldsymbol{r}' \frac{\psi_j^*(\boldsymbol{r}')\psi_j(\boldsymbol{r})}{|\boldsymbol{r}-\boldsymbol{r}'|}\psi_i(\boldsymbol{r}') = \varepsilon_i \psi_i(\boldsymbol{r})$$

(III.14)

Which is similar to that of the Hartree approximation (Eq. III.11), where the last term in the left side is the exchange term. This term is due to the anti-symmetry of the wave function under exchange of particle position, and it can be written as;

$$V_x \psi_i(\boldsymbol{r}) = -\iint d\boldsymbol{r}' \frac{|\rho(\boldsymbol{r}', \boldsymbol{r})|^2}{|\boldsymbol{r}-\boldsymbol{r}'|}\psi_i(\boldsymbol{r}') \quad \textbf{(III.15)}$$

where $\rho(\boldsymbol{r}, \boldsymbol{r}') = \sum_{i=1}^{N} \psi_i^*(\boldsymbol{r})\psi_i(\boldsymbol{r}')$ is the one-body density matrix of the electrons.

Then, the Hartree-Fock total energy is given as;

$$E_{HF} = T + E_{ext} + E_H + E_X \quad \textbf{(III.16)}$$

where T, E_H, E_X and E_{ext} is the kinetic energy, the Hartree potential energy, the exchange energy and the electron-ion potential energy, respectively, which are given by;

$$T = \sum_{i=1}^{N} \int \psi_i(\boldsymbol{r}) \nabla^2 \psi_i(\boldsymbol{r})\, d\boldsymbol{r} \quad \textbf{(III.17)}$$

$$E_{ext} = -\int d\boldsymbol{r} \sum_{I=1}^{M} \frac{Z_I \rho(\boldsymbol{r})}{|\boldsymbol{r}-\boldsymbol{R}_I|} \quad \textbf{(III.18)}$$

$$E_H = \frac{1}{2}\iint \frac{\rho(\boldsymbol{r})\rho(\boldsymbol{r}')}{|\boldsymbol{r}-\boldsymbol{r}'|} d\boldsymbol{r} d\boldsymbol{r}' \quad \textbf{(III.19)}$$

$$E_X = -\frac{1}{2}\iint \frac{\left[\rho(\boldsymbol{r}, \boldsymbol{r}')\right]^2}{|\boldsymbol{r}-\boldsymbol{r}'|} d\boldsymbol{r} d\boldsymbol{r}' \quad \textbf{(III.20)}$$

The internal potential energy is given as;

$$E_{int} = E_X + E_H \quad \textbf{(III.21)}$$

The Hartree-Fock equations can be written as a function of operators corresponding to various kinds of energy;

$$(\hat{T}(\boldsymbol{r}) + \hat{V}_{ext}(\boldsymbol{r}) + \hat{V}_H(\boldsymbol{r}) + \hat{V}_X(\boldsymbol{r}))\psi_i(\boldsymbol{r}) = \varepsilon_i\psi_i(\boldsymbol{r}) \quad \textbf{(III.22)}$$

Due to non-locality of the exchange term (E_X), these equations are more difficult to solve. This leads us to a search for a more practical method.

III.4 Density functional theory (DFT)

Density Functional Theory (DFT) is introduced in this section as a means of circumventing solution of a large, mathematically complex equations when calculating the ground state energy. DFT based on some appropriate approximations, leads to methods that are computationally feasible for performing first principles calculations on large systems.

III.4.1. The hohenberg-kohn theorems

DFT is then founded on the Hohenberg-Kohn theorems **[11]**. The first theorem states that ground state energy (E_{GS}) of a system of electrons is a unique functional of the ground state electron density, or inversely the external potential is uniquely determined by the ground state density:

$$E_{GS} = E\left[\rho_{GS}(\boldsymbol{r})\right] \quad \textbf{(III.23)}$$

The second theorem states that E_{GS} can be found variationally by optimising an energy functional and the ground state density is that at the minimum of the energy functional. Hence the Hamiltonian can be written as a functional of the density;

$$E_T[\rho(\boldsymbol{r})] = T[\rho(\boldsymbol{r})] + E_{e-e}[\rho(\boldsymbol{r})] + \int d\boldsymbol{r}\hat{V}_{ext}(\boldsymbol{r})\rho(\boldsymbol{r}) + E_{ion} \quad \textbf{(III.24)}$$

For the ground state density, $\rho_0(\boldsymbol{r})$, and another density, $\rho(\boldsymbol{r})$, corresponding to the ground state wave function Ψ_0 and the wave function Ψ_1, respectively, one can write their energies as;

$$E\left[\rho_1(\boldsymbol{r})\right] = \langle \Psi_1 \left|\hat{H}_0\right|\Psi_1 \rangle > E\left[\rho_0(\boldsymbol{r})\right] = \langle \Psi_0 \left|\hat{H}_0\right|\Psi_0 \rangle \quad \textbf{(III.25)}$$

where the unique functional energy is the expectation Hamiltonian $\hat{H}_0$. Then, this theorem provides a method for finding the ground state.

III.4.2. The kohn-sham method

W. Kohn and L.J. Sham **[12]** proposed a replacement of the real system (interacting electrons) by a fictitious one (non-interacting electrons), which generates the same density as the real system, i.e. fictitious auxiliary system **[1, 13]**. The independent *N*-particle Hamiltonian can then be written as the sum of *N* single-particle Hamiltonians;

$$(\hat{T}_S(\boldsymbol{r}) + \hat{V}_{ext}(\boldsymbol{r}) + \hat{V}(\boldsymbol{r}))\phi_i(\boldsymbol{r}) = \varepsilon_i\phi_i(\boldsymbol{r}) \quad \textbf{(III.26)}$$

here ε_i is the Kohn-Sham eigenenergy of the single-particle wave functions $\phi_i(\boldsymbol{r})$, known as the Kohn-Sham orbital, $\hat{V}(\boldsymbol{r})$ is a non-interacting effective potential given as;

$$\hat{V}(\boldsymbol{r}) = \hat{V}_H(\boldsymbol{r}) + \hat{V}_{XC}(\boldsymbol{r}) \quad \textbf{(III.27)}$$

where $\hat{V}_H(\boldsymbol{r})$ is the Hartree potential, Eq.III.12, and the terms $\hat{V}_{XC}(\boldsymbol{r})$ is the exchange-correlation potential defined as:

$$\hat{V}_{XC}(\boldsymbol{r}) = \frac{\delta E_{XC}}{\delta\rho(\boldsymbol{r})} \quad \textbf{(III.28)}$$

whose role is to ensure that the Kohn-Sham auxiliary system has the same density as the interacting system. Then, this method allows to obtain a set of coupled *N* single particle Schrödinger equations from the *N*-electron problem.

The density of the Kohn-Sham system is given by;

$$\rho(\boldsymbol{r}) = \sum_1^N \phi_i^*(\boldsymbol{r})\phi_i(\boldsymbol{r}) \quad \textbf{(III.29)}$$

The kinetic energy operator is given by;

$$\hat{T}_S(\boldsymbol{r})\phi_i(\boldsymbol{r}) = -\frac{1}{2}\nabla^2\phi_i(\boldsymbol{r}) \quad \textbf{(III.30)}$$

and its corresponding kinetic energy is expressed as;

$$T_S|\rho(\boldsymbol{r})| = -\frac{1}{2}\sum_1^N \int \phi_i^*(\boldsymbol{r})\nabla^2\phi_i(\boldsymbol{r})d\boldsymbol{r} \quad \textbf{(III.31)}$$

III.4.3. Exchange-correlation functional

The replacement of the fully interacting system with a non interacting system in the Kohn-Sham equations leads to the same ground state density. The exchange correlation (XC) energy, which contains the difference between the exact and non interacting kinetic energies **[13],** is defined as;

$$\boldsymbol{E_{XC}|\rho(r)|} = \langle\Psi|\hat{\boldsymbol{T}}|\Psi\rangle - \boldsymbol{T_S|\rho(r)|} + \frac{\mathbf{1}}{\mathbf{2}}\sum_{i\neq j}\left\langle\Psi\left|\frac{\mathbf{1}}{|r_i - r_j|}\right|\Psi\right\rangle - \boldsymbol{E_H|\rho(r)|} \quad \textbf{(III.32)}$$

with the Fock exchange integral is given by;

$$\boldsymbol{E_x} = -\frac{\mathbf{1}}{\mathbf{2}}\sum_{i,j}^{N}\iint\frac{\boldsymbol{\phi_i^*(r)\phi_j(r)\phi_j^*(r')\phi_i(r')drdr'}}{|\boldsymbol{r}-\boldsymbol{r}'|} \quad \textbf{(III.33)}$$

The exact form of the $E_{XC}|\rho(\boldsymbol{r})|$ functional is not known but several approximations are available.

The local density approximation (LDA) is one of the most commonly used exchange-correlation functional **[12]**. In LDA, the exchange-correlation energy per electron at a point ***r***, $\in_{XC}(\boldsymbol{r})$, is taken to be the same as the exchange-correlation energy of a homogeneous electron gas (HEG) with the same density as the local density **[14, 15].** Thus, the exchange-correlation energy of the system, $E_{XC}^{LDA}|\rho(\boldsymbol{r})|$, is expressed as:

$$E_{XC}^{LDA}|\rho(\boldsymbol{r})| = \int \in_{XC}^{HEG}(\rho(\boldsymbol{r}))\rho(\boldsymbol{r})d\boldsymbol{r} \quad \textbf{(III.34)}$$

LDA has shown reasonable results compared to available experimental data, but the most major problem of LDA is the well-known underestimation of the band gap (up to 50% for semiconductors).

To overcomes the LDA's shortcomings, the generalized gradient approximation (GGA) was proposed, in which the exchange-correlation functional depends not only on the local electron density but also on its gradient at the position ***r***;

$$E_{XC}^{GGA}|\rho(\boldsymbol{r})| = \int \in_{XC}^{HEG}\big(\rho(\boldsymbol{r})\big)F(\rho(\boldsymbol{r}),|\nabla\rho(\boldsymbol{r})|)\rho(\boldsymbol{r})d\boldsymbol{r} \quad \textbf{(III.35)}$$

where $\rho(\boldsymbol{r})$ is the electron density and $\nabla\rho(\boldsymbol{r})$ is its gradient and $F(\rho(\boldsymbol{r}),|\nabla\rho(\boldsymbol{r})|)$ where $F(\rho(\boldsymbol{r}),|\nabla\rho(\boldsymbol{r})|)$ is the enhancement factor parameterised from a set of homogeneous electron gas calculations. This approximation leads to improve some physical parameters such lattice constants and cohesive energies. However, the band gap underestimation remains unsolved in GGA. Further extension is to include higher order derivatives of the density, known as the meta-GGAs **[16].**

There is another form of the exchange-correlation functional, known as hybrid functionals, which is a mixture between the Fock exchange integral and the local LDA or GGA exchange correlation energy. The Becke three-parameter functional with the Lee-Yang-Parr

correlation functional (B3LYP) and the screened exchange functional (sX) are the most popular hybrid functionals **[17-19]**.

III.4.4. Spin polarized systems

In real systems, each electron can be spin-up (↑) or spin-down (↓), so its orbital $\phi_i(\boldsymbol{r})$ needs to be written with inclusion of a spin index, σ; $\phi_i^{\sigma}(\boldsymbol{r})$. The charge density is then given by;

$$\rho(\boldsymbol{r}) = \sum_{\sigma} \sum_{1}^{N^{\sigma}} \phi_i^{\sigma *}(\boldsymbol{r}) \phi_i^{\sigma}(\boldsymbol{r}) \qquad \textbf{(III.36)}$$

where the total number of electrons is $N = \sum_{\sigma} N^{\sigma}$.

The Kohn-Sham Hamiltonian is given by;

$$\left(-\frac{1}{2} \nabla^2 + \hat{V}_{ext}(\boldsymbol{r}) + \hat{V}_{XC}^{\sigma}\left[\rho^{\uparrow}(\boldsymbol{r}), \rho^{\downarrow}(\boldsymbol{r})\right](\boldsymbol{r}) + \int \frac{\rho(\boldsymbol{r}')}{|\boldsymbol{r}-\boldsymbol{r}'|} d\boldsymbol{r}'\right) \phi_i^{\sigma}(\boldsymbol{r}) = \varepsilon_i^{\sigma} \phi_i^{\sigma}(\boldsymbol{r}) \qquad \textbf{(III.37)}$$

The Fock exchange integral becomes;

$$\hat{V}_X^{\sigma} \phi_i^{\sigma}(\boldsymbol{r}) = -\int \frac{\rho^{\sigma}(\boldsymbol{r}, \boldsymbol{r}')}{|\boldsymbol{r}-\boldsymbol{r}'|} \phi_i^{\sigma}(\boldsymbol{r}') d\boldsymbol{r}' \qquad \textbf{(III.38)}$$

where $\rho^{\sigma}(\boldsymbol{r}, \boldsymbol{r}')$ is the spin polarized reduced density matrix given as;

$$\rho^{\sigma}(\boldsymbol{r}, \boldsymbol{r}') = \sum_{1}^{N^{\sigma}} \phi_i^{\sigma *}(\boldsymbol{r}) \phi_i^{\sigma}(\boldsymbol{r}') \qquad \textbf{(III.39)}$$

where the spins of the electrons are collinear. The application of DFT to non-collinear systems, resulting from the relativistic effects of spin-orbit interaction, is beyond the scope of this thesis.

III.4.5. The LDA+U method

DFT suffers from a notable various of shortcomings. One of them is DFT's failure in predicting the band gap values for insulators and semiconductors. DFT seems to underestimate the band gap by up to 50% **[20, 21]**. This is especially obvious for strongly correlated materials such as transition metal or rare earth ions, containing the strongly localized d or f electrons. There are many ways to remedy the electronic band gap underestimation, such as LDA+U and GW approximation. The Hubbard U correction, known as LDA+U formalism, is taken to shift the LDA *d/f* orbitals and , sometimes, the delocalized s and p electrons. Anisimov et al. **[22]** suggested a smi-local DFT with a correction based on Hubbard model that accounting for the on-site repulsion of the localized electrons while the other are still described via standard DFT.

To describe the interactions between the electrons in the d-orbitals, the Hubbard (*U* value), is added to the energy:

$$E = E_{LDA} - U\frac{N(N-1)}{2} + \frac{1}{2}\sum_{i\neq j} n_i n_j \quad \textbf{(III.40)}$$

where E_{LDA} is the usual LDA term describing the delocalized s and p orbitals, $UN(N-1)/2$ is the Coulomb energy of d-d electrons, which is a function of the total number of d-electrons, *N*, and the third term is the additional Hubbard term depending on the orbital occupancies n_i. The potential of the orbitals, describing the change in charge density, is given by

$$V_i(r) = V_{LDA}(r) - U\left(\frac{1}{2} - n_i\right) \quad \textbf{(III.41)}$$

III.5. Computational methods for crystalline system

III.5.1. Periodic boundary conditions

The systems of interest are crystalline solids. So, the periodic unit cells that form the crystal is arranged in all directions by imposing periodic boundary conditions. This requires the potentials and density to be periodic in space:

$$\hat{V}(\boldsymbol{r} + \boldsymbol{R}) = \hat{V}(\boldsymbol{r}) \quad \textbf{(III.42)}$$

and

$$\rho(\boldsymbol{r} + \boldsymbol{R}) = \rho(\boldsymbol{r}) \quad \textbf{(III.43)}$$

where $\boldsymbol{R}$ is any real lattice vector, defined by:

$$\boldsymbol{R} = l\boldsymbol{a} + m\boldsymbol{b} + n\boldsymbol{c} \quad \textbf{(III.44)}$$

l, m and n are integers value, and $\boldsymbol{a}$, $\boldsymbol{b}$ and $\boldsymbol{c}$ are vectors defining 3 edges of the parallelepiped that forms the *unit cell*. In a similar way to the real lattice vectors, the *reciprocal lattice* vectors are defined by:

$$\boldsymbol{G} = l\boldsymbol{a}^* + m\boldsymbol{b}^* + n\boldsymbol{c}^* \quad \textbf{(III.45)}$$

where $\boldsymbol{a}^* = 2\pi\, \boldsymbol{b}$ x $\boldsymbol{c}/\Omega$, $\boldsymbol{b}^* = 2\pi\, \boldsymbol{c}$ x $\boldsymbol{a}/\Omega$, $\boldsymbol{c}^* = 2\pi\, \boldsymbol{a}$ x $\boldsymbol{b}/\Omega$, $\Omega = \boldsymbol{a}.(\boldsymbol{b}$ x $\boldsymbol{c})$ is the volume of the unit cell and $\boldsymbol{R}.\boldsymbol{G} = 2\pi$.

III.5.2. Bloch's theorem

While the potential and ground state density of a periodic system satisfy periodic boundary conditions, there is no guarantee that the Kohn-Sham orbitals that form the density are periodic. To satisfy the Kohn-Sham equations for a periodic Kohn-Sham potential, we must have:

$$\phi_{j,\boldsymbol{K}}^{\sigma}(\boldsymbol{r}+\boldsymbol{R}) = \phi_{j,\boldsymbol{K}}^{\sigma}(\boldsymbol{r})e^{i\boldsymbol{k}.\boldsymbol{R}} \qquad \textbf{(III.46)}$$

This leads to *Bloch's theorem* **[8]** for Kohn-Sham orbitals:

$$\phi_{j,\boldsymbol{K}}^{\sigma}(\boldsymbol{r}) = u_{j,\boldsymbol{K}}^{\sigma}(\boldsymbol{r})e^{i\boldsymbol{k}.\boldsymbol{r}} \qquad \textbf{(III.47)}$$

with $u_{j,\boldsymbol{K}}^{\sigma}(\boldsymbol{r}) = u_{j,\boldsymbol{K}}^{\sigma}(\boldsymbol{r}+\boldsymbol{R})$ and $\boldsymbol{k}$ is a wave vector that lies within the first Brillouin zone of the reciprocal lattice, such that:

$$\boldsymbol{k} = k_x\boldsymbol{a}^* + k_y\boldsymbol{b}^* + k_z\boldsymbol{c}^* \qquad \textbf{(III.48)}$$

with $-1/2 \leq k_x, k_y, k_z \leq 1/2$.

III.5.3. Basis sets

Since $u_{j,\boldsymbol{K}}^{\sigma}(\boldsymbol{r})$ is a periodic function, it can be expanded as a linear combination of known functions constituting a basis set, which can be atomic orbitals, Gaussians, plane waves among other choices. For the fist choice, each orbital is formed of a series of atomic orbitals issued from solutions to the hydrogen-like atom problem. The second choice is based on the using of an expansion of Gaussians orbitals, which suffers from the difficulty of achieving convergence. In a periodic system, $u_{j,\boldsymbol{K}}^{\sigma}(\boldsymbol{r})$ can be expended using an orthogonal basis set of plane waves (the choice of basis set to be used in this work) as a Fourier series:

$$u_{j,\boldsymbol{K}}^{\sigma}(\boldsymbol{r}) = \frac{1}{\Omega}\sum_{\boldsymbol{G}} c_{j,\boldsymbol{K}}^{\sigma}(\boldsymbol{G})\, e^{i\boldsymbol{G}.\boldsymbol{r}} \qquad \textbf{(III.49)}$$

Thus the orbitals can take the form:

$$\phi_{j,\boldsymbol{K}}^{\sigma}(\boldsymbol{r}) = \frac{1}{\sqrt{\Omega}}\sum_{\boldsymbol{G}} c_{j,\boldsymbol{K}}^{\sigma}(\boldsymbol{G})\, e^{i(\boldsymbol{G}+\boldsymbol{k}).\boldsymbol{r}} \qquad \textbf{(III.50)}$$

There are other basis sets, namely the augmented plane wave (APW) **[23]**, linearized augmented plane waves (LAPW) **[24]** and projector augmented plane waves (PAW) **[25]**. The use of a specific method depends on the orbital type, i.e. localized or delocalized orbital.

III.5.4. Monkhorst-pack grids

In many circumstances, an integration over the Brillouin zone (BZ) has to be performed. Since this integration is computationally expensive, the integral is done over a finite set of *k* points:

$$\int_{BZ} \frac{1}{\Omega_{BZ}} d\boldsymbol{k} \rightarrow \sum_{\boldsymbol{k} \in BZ} \omega_{\boldsymbol{K}} \quad \textbf{(III.51)}$$

This approach is known as Brillouin zone sampling where $\omega_{\boldsymbol{K}}$ is the weight of *k* points and Ω_{BZ} is the volume of the Brillouin zone, which is reduced by exploiting the symmetry in crystalline solids. There are several methods for choosing the *k* points. Among these, the special points method is very efficient in accelerating the convergence with the number of *k* points. The Monkhorst and Pack method **[26]** as implemented in CASTEP is used in this work. This method is represented by the following formula:

$$\boldsymbol{k}_{x,y,z} = \sum_{j=1}^{3} \frac{2n_j - 2 + \delta_j}{2N_j} \boldsymbol{G}_j \quad \textbf{(III.52)}$$

where $\boldsymbol{G}_j$ is a vector from reciprocal lattice, $\delta_j = 0 \; or \; 1$ and $n_j = 1, 2, \ldots N_j$.

III.5.5. Plane wave cut off energies

According to Bloch's theorem, the electronic wave function at each k-point can be extended in terms of a discrete and infinite plane wave basis set. Since the coefficients $c_{j,K}^{\sigma}(\boldsymbol{G}) == 1/\Omega \int \phi_{j,\boldsymbol{K}}^{\sigma}(\boldsymbol{r}) e^{-i(\boldsymbol{G}+\boldsymbol{k}).\boldsymbol{r}} d\boldsymbol{r}$ for plane waves with smaller kinetic energy $|\boldsymbol{k} + \boldsymbol{G}|^2$ are normally more significant than those for plane waves with large kinetic energy. A cut-off energy can be described in a sphere for the reciprocal space by fixing the highest vectors for the infinite basis set $\boldsymbol{G}_{max}$;

$$E_{Cut} = \frac{1}{2} |\boldsymbol{k} + \boldsymbol{G}_{max}|^2 \quad \textbf{(III.53)}$$

The orbitals has then the form;

$$\phi_{j,\boldsymbol{K}}^{\sigma}(\boldsymbol{r}) = \frac{1}{\sqrt{\Omega}} \sum_{|G|=0}^{|\boldsymbol{G}_{max}|} c_{j,\boldsymbol{K}}^{\sigma}(\boldsymbol{G}) e^{i(\boldsymbol{G}+\boldsymbol{k}).\boldsymbol{r}} \quad \textbf{(III.54)}$$

III.5.6. Reciprocal space

If we write an orbital as a sum of plane waves (3.44), the kinetic energy operator can be written as:

$$\hat{T}_S(\boldsymbol{r})\phi^{\sigma}_{j,\boldsymbol{K}}(\boldsymbol{r}) = -\frac{1}{2}\nabla^2\phi^{\sigma}_{j,\boldsymbol{K}}(\boldsymbol{r}) = -\frac{1}{2\sqrt{\Omega}}\sum_{\boldsymbol{G}}|\boldsymbol{k}+\boldsymbol{G}|^2 c^{\sigma}_{j,\boldsymbol{K}}(\boldsymbol{G})\, e^{i(\boldsymbol{G}+\boldsymbol{k}).\boldsymbol{r}} \quad \textbf{(III.55)}$$

The kinetic energy can be written as;

$$T_S = \sum_{\sigma}\frac{1}{N_k}\sum_{i,\boldsymbol{K}}\int \phi^{\sigma*}_{i,\boldsymbol{K}}(\boldsymbol{r})\hat{T}_S\phi^{\sigma}_{i,\boldsymbol{K}}(\boldsymbol{r})d\boldsymbol{r} = -\frac{1}{2N_k}\sum_{\sigma}\sum_{i,\boldsymbol{K}}\sum_{\boldsymbol{G}}|\boldsymbol{k}+\boldsymbol{G}|^2 c^{\sigma}_{i,\boldsymbol{K}}(\boldsymbol{G})\, c^{\sigma*}_{i,\boldsymbol{K}}(\boldsymbol{G}) \quad \textbf{(III.56)}$$

where N_k is the total number of k-points and the division by N_k is due to the sum over *k*-points as well as electrons.

The density can be written as a Fourier transform;

$$\rho(\boldsymbol{G}) = \int d\boldsymbol{r}\rho(\boldsymbol{r})e^{-i\boldsymbol{G}.\boldsymbol{r}} = \sum_{\sigma}\int d\boldsymbol{r}\sum_{i,\boldsymbol{k}}\frac{1}{N_K}\phi^{\sigma}_{i,\boldsymbol{k}}(\boldsymbol{r})\phi^{\sigma*}_{i,\boldsymbol{k}}(\boldsymbol{r})e^{-i\boldsymbol{G}.\boldsymbol{r}}$$

$$= \sum_{\sigma}\sum_{i,\boldsymbol{k}}\frac{1}{N_K}\sum_{\boldsymbol{G}'}c^{\sigma*}_{i,\boldsymbol{K}}(\boldsymbol{G}')\int d\boldsymbol{r}\frac{1}{\sqrt{\Omega}}\phi^{\sigma}_{i,\boldsymbol{k}}(\boldsymbol{r})e^{-i(k+\boldsymbol{G}+\boldsymbol{G}').\boldsymbol{r}}$$

$$= \frac{1}{N_k}\sum_{\sigma}\sum_{i,\boldsymbol{k}}\sum_{\boldsymbol{G}'}c^{\sigma*}_{i,\boldsymbol{k}}(\boldsymbol{G}')c^{\sigma}_{i,\boldsymbol{k}}(\boldsymbol{G}'+\boldsymbol{G}) \quad \textbf{(III.57)}$$

The Hartree potential can be also found as;

$$\hat{V}_H(\boldsymbol{G}) = \int d\boldsymbol{r}\hat{V}_H(\boldsymbol{r})e^{-i\boldsymbol{G}.\boldsymbol{r}} = \iint d\boldsymbol{r}'d\boldsymbol{r}\frac{\rho(\boldsymbol{r}')}{|\boldsymbol{r}-\boldsymbol{r}'|}e^{-i\boldsymbol{G}.\boldsymbol{r}}$$

$$= \frac{1}{\Omega}\int d\boldsymbol{r}\sum_{\boldsymbol{G}'}\rho(\boldsymbol{G}')e^{-i\boldsymbol{G}.\boldsymbol{r}}\int d\boldsymbol{r}'\frac{1}{|\boldsymbol{r}-\boldsymbol{r}'|}e^{i\boldsymbol{G}'.\boldsymbol{r}} = \frac{4\pi}{\Omega}\sum_{\boldsymbol{G}'}\frac{\rho(\boldsymbol{G}')}{|\boldsymbol{G}'|^2}\int d\boldsymbol{r}\, e^{i(\boldsymbol{G}'-\boldsymbol{G}).\boldsymbol{r}}$$

$$= \frac{4\pi}{\Omega}\frac{\rho(\boldsymbol{G})}{|\boldsymbol{G}|^2} \quad \textbf{(III.58)}$$

The Hartree energy ($\hat{V}_H(\boldsymbol{G}) = \delta E_H/\delta\rho(\boldsymbol{G})$) is then given by;

$$E_H = \frac{2\pi}{\Omega}\sum_{\boldsymbol{G}}\frac{|\rho(\boldsymbol{G})|^2}{|\boldsymbol{G}|^2} \quad \textbf{(III.59)}$$

The exchange energy is also given as;

$$E_{\mathcal{X}} = \frac{2\pi}{\Omega}\frac{1}{N_qN_k}\sum_{\sigma}\sum_{i,\boldsymbol{k}}\sum_{j,q}\sum_{\boldsymbol{G}}\sum_{\boldsymbol{G}'}\sum_{\boldsymbol{G}''}c^{\sigma*}_{i,\boldsymbol{k}}(\boldsymbol{G})\frac{c^{\sigma*}_{j,q}(\boldsymbol{G}'+\boldsymbol{G}'')c^{\sigma}_{j,q}(\boldsymbol{G}+\boldsymbol{G}'')}{|\boldsymbol{q}-\boldsymbol{k}+\boldsymbol{G}''|^2}c^{\sigma}_{i,\boldsymbol{k}}(\boldsymbol{G}') \quad \textbf{(III.60)}$$

In reciprocal space, any single-particle quantum operator, $\hat{O}$, can be represented as a matrix, $O(\boldsymbol{G},\boldsymbol{G}')$, which acts on an orbital represented by the coefficients, $c_{i,\boldsymbol{k}}(\boldsymbol{G})$, as follows **[1]**:

$$\hat{O}c_{i,\boldsymbol{k}}(\boldsymbol{G}) = \sum_{\boldsymbol{G}'}O(\boldsymbol{G},\boldsymbol{G}')\, c_{i,\boldsymbol{k}}(\boldsymbol{G}') \quad \textbf{(III.61)}$$

So, the matrix representation of the kinetic energy operator is;

$$T(\boldsymbol{G},\boldsymbol{G}') = \frac{1}{2}\,|\boldsymbol{k}+\boldsymbol{G}|^2\delta_{\boldsymbol{G},\boldsymbol{G}'} \quad \textbf{(III.62)}$$

and that of any local potential operator, such as the Hartree potential, is given as;

$$\mu(\boldsymbol{G},\boldsymbol{G}') = \frac{1}{\Omega}\mu(\boldsymbol{G}-\boldsymbol{G}') \quad \textbf{(III.63)}$$

Using the matrix representations of operators in reciprocal space, the Kohn-Sham equations (**Eqs. III.34**) can be written as;

$$\sum_{\boldsymbol{G}'}\left(\frac{1}{2}|\boldsymbol{k}+\boldsymbol{G}|^2\delta_{\boldsymbol{G},\boldsymbol{G}'} + \hat{V}_{ext}(\boldsymbol{G}-\boldsymbol{G}') + \hat{V}_H(\boldsymbol{G}-\boldsymbol{G}') + \hat{V}_{xc}^{\sigma}(\boldsymbol{G}-\boldsymbol{G}')\right) c_{i,\boldsymbol{k}}^{\sigma}(\boldsymbol{G}') = \varepsilon_i^{\sigma} c_{i,\boldsymbol{k}}^{\sigma}(\boldsymbol{G}) \quad \textbf{(III.64)}$$

which can be solved by using several different techniques.

III.6. Pseudopotentials

The Kohn-Sham equations including the interactions of all the electrons in the material, needs a high cut off energy for the Bloch orbital. To reduce the cut off energy of the orbitals, the electrons in the material must be partitioned into core electrons, which are tightly bound and localised on the lattice sites and not affected by a change in the chemical environment, and valence electrons, which form the bonding orbitals in a solid and are greatly changed by the chemical environment. So, it must first specify the cut-off radius, r_c, and also specify which electrons are to be considered valence, and which are to be considered core. Generally, all the electrons in "closed shells" are considered core, while the remainder are considered valence. The external potential $V_{ext}(\boldsymbol{r})$ is now replaced with the pseudopotential $V_{ps}(\boldsymbol{r})$ and with only valence electrons present. For all points *r* that lie outside the cut-off radius, the resulting pseudo-orbital, $\psi_{ps}(\boldsymbol{r})$ with no radial nodes inside the cut-off radius, must equal the all-electron orbital, $\psi_{AE}(\boldsymbol{r})$, and their corresponding eigenvalues must be equal as well (Figure III.2). Also, the first and second derivatives of each $\psi_{ps}(\boldsymbol{r})$ must equal those of the corresponding $\psi_{AE}(\boldsymbol{r})$ at r_c.

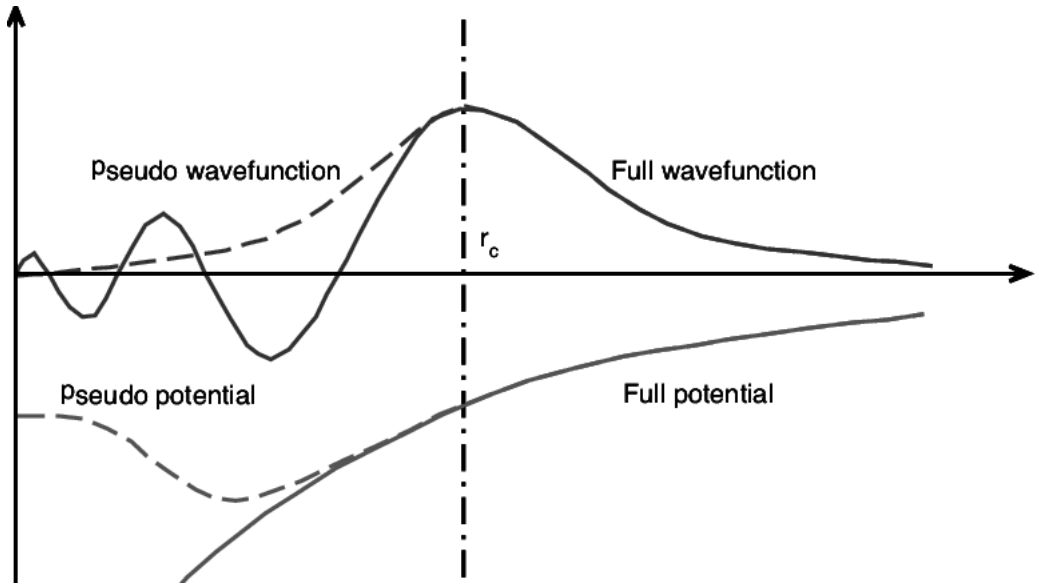

Figure III.2: Pseudopotential and the pseudo-wave function.

Pseudopotentials in which each orbital is normalized to 1 are referred to as normconserving pseudopotentials. An ultrasoft pseudopotentials also exist **[27]**, in which the condition of normalisation is relaxed, allowing a lower plane wave cut-off energy, which will be used in this work.

III.7. Ultrasoft pseudopotentials

Within the ultrasoft approximation, the norm-conserving constraint is relaxed and the cut-off radius can be increased, the kinetic energy is reduced, the valence electrons exhibited a smoother potential with a decrease number of the required plane waves **[27]**.

The increase in r_c decreases the transferability of ultrasofts to some extent, that is less accurate to reproduce realistic features in different environments.

The charge density is given as:

$$\rho(\boldsymbol{r}) = \sum_i \left(\left| \phi_i \ (\boldsymbol{r}) \right|^2 + \sum_{nml} Q^i_{nm}(\boldsymbol{r}) \langle \phi_i | \alpha^l_n \rangle \langle \alpha^l_m | \phi_i \rangle \right) \quad \textbf{(III.65)}$$

where $Q^i_{nm}(\boldsymbol{r})$ are the augmentation functions that are strictly localized in the core regions and $\phi_i(\boldsymbol{r})$ are the wave functions. The ultrasoft potential can be written as

$$V = V_{local}(\boldsymbol{r}) + \sum_{nml} D^l_{nm} \, |\alpha^l_n\rangle\langle\alpha^l_m| \quad \textbf{(III.66)}$$

where the coefficients $D_{nm}^{l}(\boldsymbol{r})$ and the projectors α_{n}^{l} characterize the pseudopotential and differ for different atomic species. The index *l* refers to an atomic site.

III.8. Solving the kohn-sham equations

The Kohn-Sham equations (Eqs.III.63), with the matrix representations of operators in reciprocal space and a finite basis set, is a numerically solvable. However, the direct matrix diagonalisation is very expensive due to the very large number of plane waves used as basis set. Generally, the obtained solution will not be self-consistent, and several iterative cycles are needed in order to minimize the energy. An alternative approach is based on the gradient of the energy with respect to the orbitals $\delta E/\delta c_{i,\boldsymbol{k}}^{*}(\boldsymbol{G})$, which enables to use minimisation algorithms such as steepest descents or conjugate gradients **[28]**.

The principle of the steepest descent algorithm is given by;

$$h^{1} = -\frac{\partial E}{\partial \phi}\Big]_{\phi=\phi^{1}} \qquad \textbf{(III.67)}$$

where h^{1} is the first steepest descent direction. The steepest descent begins with a trial set of Kohn-Sham orbitals, which will remain orthogonal. Iteratively, the algorithm calculates the search direction, ζ_{i}^{p}, for a single orbital, *i*, at iteration *p*;

$$\zeta_{i}^{p} = -(\hat{H} - \langle \phi_{i}^{p} | \hat{H} | \phi_{i}^{p} \rangle)\phi_{i}^{p} \qquad \textbf{(III.68)}$$

Using the Gram-Schmidt scheme, this is accomplished by orthogonalizing the search direction against all the other orbitals **[2]**;

$$\zeta_{i}^{\prime p} = \zeta_{i}^{p} - \sum_{j\neq i} \langle \phi_{j}^{p} | \zeta_{i}^{p} \rangle \, \phi_{j}^{p} \qquad \textbf{(III.69)}$$

The typical procedure for the three point minimisation is shown (**Figure III.3**).

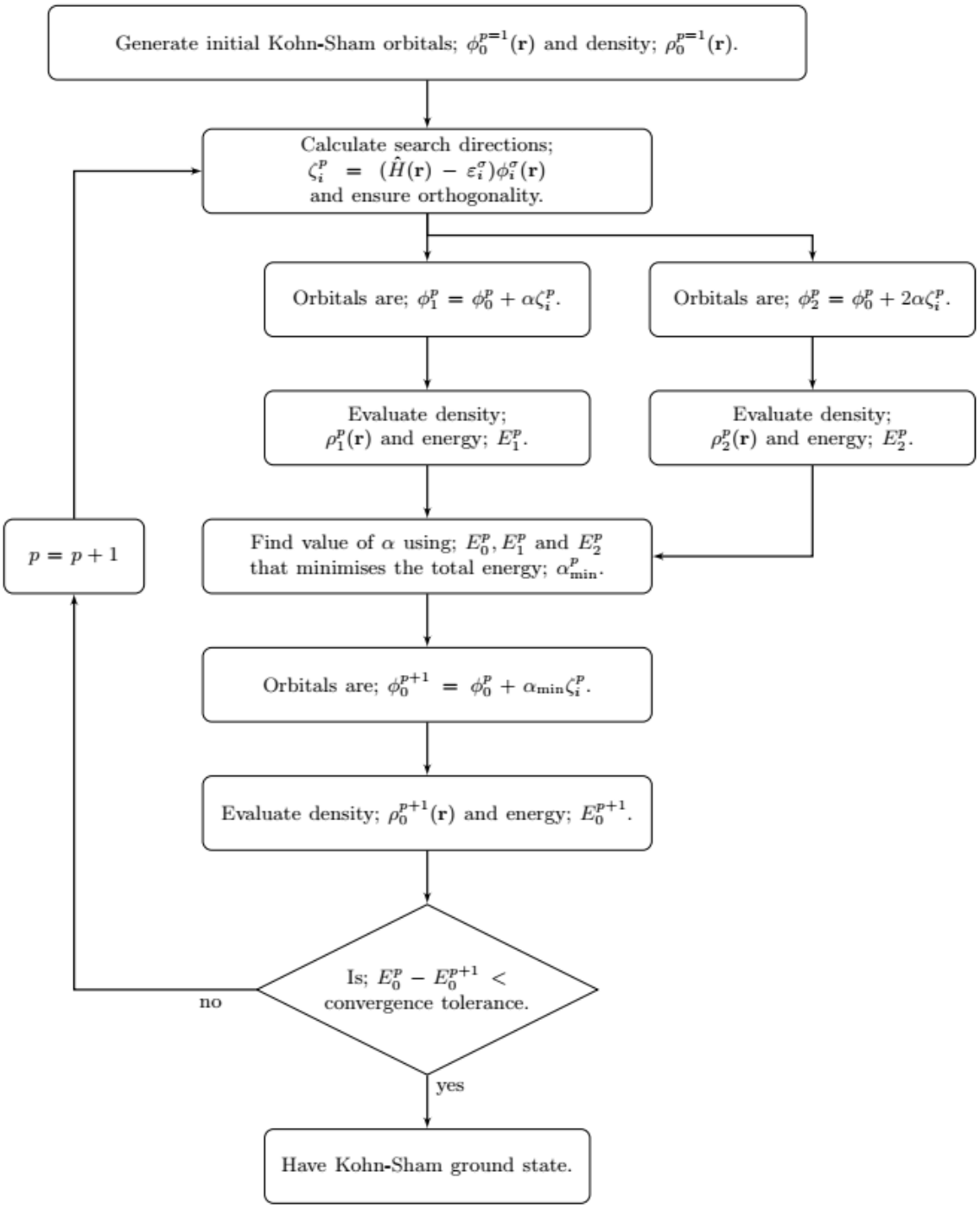

Figure III.3. A steepest descent method and a parabolic line search are used to calculate the total energy of a Kohn-Sham system, reprintet from Ref **[2]**.

The steepest descent method may not guarantee convergence in a finite number of steps. The conjugate gradient method, in which subsequent search direction is conjugate to all previous search directions, usually reduces the number of steps needed to the convergence **[4]**.

III.9. Geometry optimisation

The force $\boldsymbol{F}_I$ on an atom with position $\boldsymbol{R}_I$ is calculated from the total energy of the system, *E*, using the Hellman-Feynman theorem **[29]** as:

$$\boldsymbol{F}_I = \frac{\partial E}{\partial \boldsymbol{R}_I} = \sum_i \left\langle \phi_i \middle| \frac{\partial \hat{H}}{\partial \boldsymbol{R}_I} \middle| \phi_i \right\rangle \qquad \textbf{(III.70)}$$

A minimisation of the total energy can be performed from the calculated forces using a similar methodology as that of the steepest descent algorithm. This is done by varying the ionic positions and unit cell dimensions.

III.10. CASTEP software package

CASTEP (Cambridge Serial Total Energy Package) is a full-featured materials modelling code based on a first-principles quantum mechanical description of electrons and nuclei **[30]**. It uses the robust methods of a plane-wave basis set and pseudopotentials. In this research, both CASTEP 9.0 and the commercial version Biovia Material Studio 2017 are used. The code is written in FORTRAN 90 and includes efficient fast-Fourier transforms (FFTs) for converting quantities between real and reciprocal space. The code is also parallelized to increase calculation speed by distributing tasks across multiple processors. CASTEP also supports shared memory processes, which allow a subgroup of processors in the same G-vector group to share memory for the storage of quantities.

References

[1] M.C. Gibson, Implementation and application of advanced density functionals. 2006. Thèse de doctorat. Durham University.

[2] T.W.Hollins, Local Exchange Potentials in Density Functional Theory, Durham University, 2014.

[3] M. Born, R. Oppenheimer, Zur quantentheorie der molekeln. Annalen der physik, 1927, vol. 389, no 20, p. 457-484.

[4] R.M.A. Khalil, Ab initio studies of the structural, dynamical and thermodynamical properties of graphitic and hydrogenated graphitic materials and their potential for hydrogen storage . University of Salford (United Kingdom), 2014.

[5] P.R .Yang, Density functional theory of atoms and molecules, 1 (1989) 989.

[6] G.Grosso,P.P. Giuseppe, Solid state physics, second printing, British Library Cataloging, UK , 2003.

[7] E. Kaxiras, Atomic and electronic structure of solids . Cambridge University Press, 2003.

[8] W. AshcroftNeil, N.W. Ashcroft, N.D. Mermin, N.D. Mermin, Solid state physics. 1976.

[9] W.A. Harrison, Electronic structure and the properties of solids: the physics of the chemical bond . Courier Corporation, 2012.

[10] V.Fock, Näherungsmethode zur Lösung des quantenme chanischen Mehrkörper problems, Zeitschrift für Physik , 1930, vol. 61, no 1-2, p. 126-148.

[11] P. Hohenberg, W. Kohn, Inhomogeneous electron gas. Physical review, 1964, vol. 136, no 3B, p. B864.

[12] W. Kohn, L.J. Sham, Self-consistent equations including exchange and correlation effects. Physical review, 1965, vol. 140, no 4A, p. A1133.

[13] D.P. Mora Fonz, A Theoretical Study on the Surfaces of Zinc Oxide. 2016. Thèse de doctorat. UCL (University College London).

[14] N.G. Worth, Theoretical studies of compressed xenon oxides, tin selenide thermoelectrics, and defects in graphene. 2018. Thèse de doctorat. University of Cambridge.

[15] H. Li, Density Functional Simulations of Defect Behavior in Oxides for Applications in MOSFET and Resistive Memory. 2018. Thèse de doctorat. University of Cambridge.

[16] J.P. Perdew, S. Kurth, A. Zupan, P. Blaha, Accurate density functional with correct formal properties: A step beyond the generalized gradient approximation. Physical review letters, 1999, vol. 82, no 12, p. 2544.

[17] A.D. Becke, Density-functional thermochemistry. IV. A new dynamical correlation functional and implications for exact-exchange mixing. The Journal of chemical physics, 1996, vol. 104, no 3, p. 1040-1046.

[18] F. Gygi, A. Baldereschi, Self-consistent Hartree-Fock and screened-exchange calculations in solids: Application to silicon. Physical Review B, 1986, vol. 34, no 6, p. 4405.

[19] S.J. Clark, J.Robertson, Screened exchange density functional applied to solids. Physical Review B, 2010, vol. 82, no 8, p. 085208.

[20] T. Qi, First-principles and molecular dynamics studies of ferroelectric oxides: Designing new materials for novel applications. 2011.

[21] M.S. Hybertsen, S.G. Louie, First-principles theory of quasiparticles: calculation of band gaps in semiconductors and insulators. Physical review letters, 1985, vol. 55, no 13, p. 1418.

[22] V.I. Anisimov, J. Zaanen, O.K. Andersen, Band theory and Mott insulators: Hubbard U instead of Stoner I. Physical Review B , 1991, vol. 44, no 3, p. 943.

[23] T.L. Loucks, Augmented plane wave method: a guide to performing electronic structure calculations . WA Benjamin, 1967.

[24] O.K. Andersen, Linear methods in band theory. Physical Review B, 1975, vol. 12, no 8, p. 3060.

[25] P.E. Blöchl, Projector augmented-wave method. Physical review B, 1994, vol. 50, no 24, p. 17953.

[26] H.J. Monkhorst, J.D. Pack, Special points for Brillouin-zone integrations. Physical review B , 1976, vol. 13, no 12, p. 5188.

[27] D. Vanderbilt, Soft self-consistent pseudopotentials in a generalized eigenvalue formalism. Physical review B, 1990, vol. 41, no 11, p. 7892.

[28] D. GEATCHES, Clay minerals and their gallery guests: an ab initio investigation into their interactions. 2011. Thèse de doctorat. Durham University.

[29] R.P. Forces in molecules. Physical review, 1939, vol. 56, no 4, p. 340.

[30] S.J. Clark, M.D. Segall, C.J. Pickard, P.J. Hasnip, M.I. Probert, K. Refson, M.C. Payne, First principles methods using CASTEP. Zeitschrift für Kristallographie-Crystalline Materials , 2005, vol. 220, no 5-6, p. 567-570.

CHAPTER IV

Results and discussions

IV.1. Introduction

Zinc oxide (ZnO) doped with transition metal (TM; i.e., Mn , Fe, Co, Ni, Cu and Ag) **has** gained a increasing interest in the last decade **[1]**. This is due to its recognized potential in many applications. Among the variety of TM, copper (Cu) has been used as dopant **[2-4]**. It exhibits an ionic radii close to that of the Zn and then can easily substitute it in ZnO host lattice. Cu dopant, as an economical option, has been chosen to enhance the properties of ZnO host lattice such as tuning of the green emission, conductivity and photocatalytic activity **[5, 6]**.

Many techniques have been used to fabricate ZnO thin films such as magnetron sputtering **[7]**, sol–gel process **[8, 9]**, chemical vapor deposition **[10]**, spray pyrolysis **[11]**, molecular beam epitaxy **[12]**, pulsed laser deposition (PLD) **[13]** and microwave plasma growth **[14]**. Sol–gel technique attracts much attention because of its advantages including safety, low cost, simple deposition equipment on a large-area films with uniform thickness. Properties of CZO thin films have been frequently investigated **[15-26]**. However, most of the published articles are limited to certain elaboration methods and low Cu-doping.

A theoretical framework is required to gain prior knowledge of the properties of materials. Plane-wave pseudopotential (PWPP) density functional theory (DFT) has been successfully used to predict the electronic ground states. Moreover, the localization of strongly correlated *d* and *f* electrons of the metal oxides are not well described by the traditional theory DFT, which underestimates their band gap [27]. Thus, DFT–LDA+U approach becomes a necessity to significantly improve such calculations **[27-30]**. There have been several theoretical studies on Cu-doped ZnO **[31-43]**, which have provided some new insights into the understanding of the effect of doping on the properties of ZnO. However, the calculated band gap of CZO was found much smaller than the experimental band gap value. So, further calculations with convenient Hubbard U values are still justified in order to enhance the band gap, which is the main motivation for the present thesis.

Several experimental studies on Cu-doped ZnO have been conducted. The majority of these studies, however, are limited to low Cu-doping of ZnO thin films. The present study is devoted to the fabrication of pure ZnO and copper-doped zinc oxide (CZO) thin films with somewhat higher Cu contents (x) (x = 1%, 3.12%, 6,25% and 12.5 at%) and low thickness. The structural, morphological, electronic and optical properties of CZO thin films are then characterized using various techniques, which were to be the subject of the first part of the present work. In order to linking of experimental results with theory, usually separated in the literature, and to enhance the energy band gap, DFT–LDA+U approach was used to predict

the properties of pure and CZO wurtzite structures, which were compared, wherever possible, with their corresponding measured values. These were to be the subject of the remainder of the present work.

IV.2 Experimental part

IV.2.1 Characterization techniques

X-ray diffractometer XRD (Broker advance Solution D8 X-ray diffractometer with Cu-kα radiation λ=1.5406 A°) was used to derive XRD diffractograms from which the Strain, crystallite size, texture coefficient, and lattice parameters are deduced. The surface morphology was studied with Field emission scanning electron microscopy FESEM (Carl Zeiss Aurga) and Atomic Force Microscopy AFM (NanoNavi /SPA 400). These techniques were used to analyze the grain size, elemental analysis, and roughness. The absorption coefficient, complex refractive index, dielectric function, and bandgap were deduced from the transmission and reflectance spectra, which were investigate by Ultraviolet-visible UV-Vis spectrophotometer (VARIAN Carry 50).

IV.2.2 Structural properties

Figure IV.1 shows the XRD diffractograms of ZnO thin films at different Cu concentrations (0%, 1%, 3.12%, 6.25% and 12.5 at%). The XRD pattern confirms the formation of polycrystalline with wurtzite hexagonal phase for pure and CZO thin films (x= 1, 3.12, 6,25 and 12.5 at%). No other phases are observed, indicating that hexagonal wurtzite structure of ZnO films isn't altered by Cu-doping. Unlike the intensity of (002) peak, the intensity of (100) and (101) peaks are generally enhanced, especially at high Cu-doping, which leads to the degradation of the (002) preferential orientation of ZnO thin films.

Similar results have also been reported earlier for CZO in other reports using various techniques; Syed Zahirullah et al. (thin films with x up to 10 %) [15], Saidani et al. (thin films with 1 wt.% $\leq x \leq$ 5 wt.%) [16], Osali et al. (thin films with 0 wt.% $\leq x \leq$ 6 wt.%)[17], Sreedhar et al. (thin films with 0 at.% $\leq x \leq$ 7.5 at.%) [18], Joshi et al. (thin films with 0 at.% $\leq x \leq$ 10 at.%) [19]. However, some other workers found that a CuO phase has been appeared with emerging a (111) new peak at high Cu doping; x= 10 at.% [19], $x \geq$ 15 at.% [20] or even at low Cu doping [21].

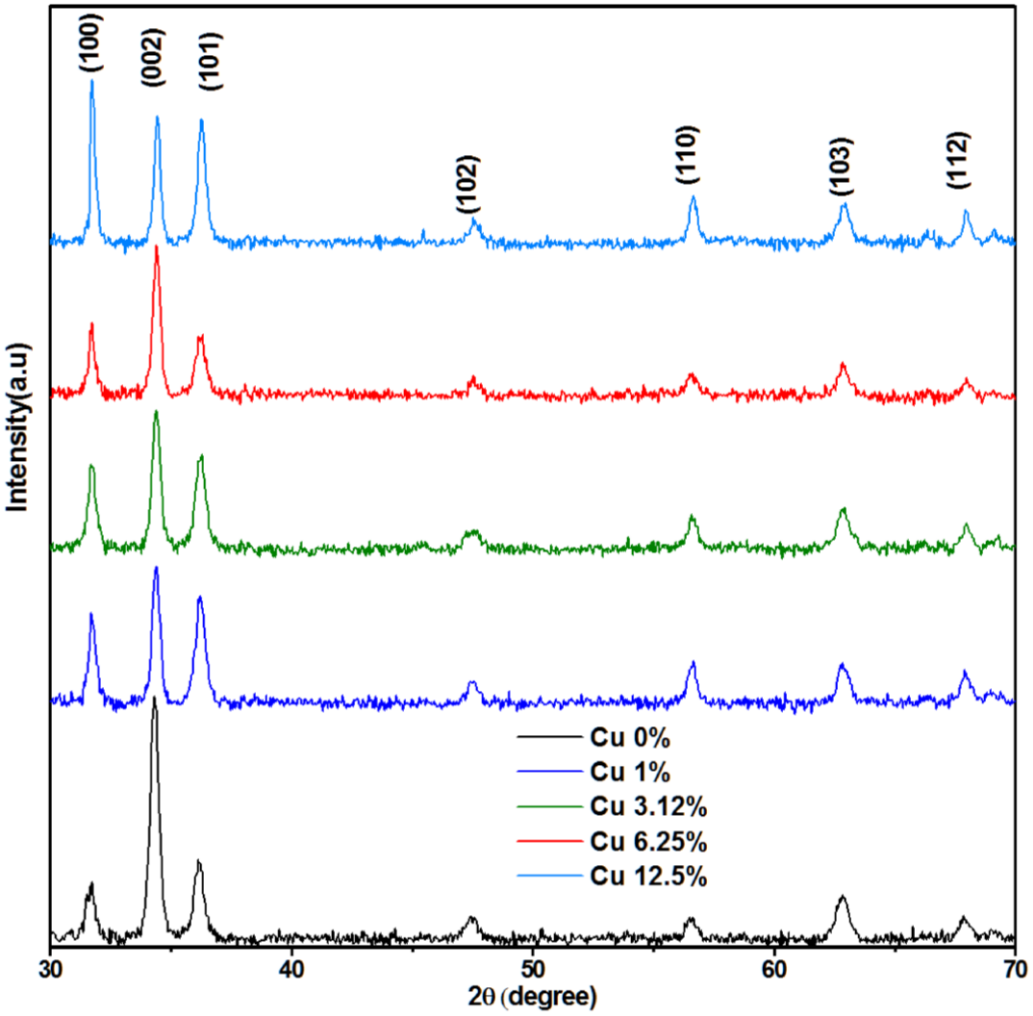

Figure IV.1. X-ray diffraction patterns of pure and Cu doped ZnO thin films (x= 1, 3.12, 6,25 and 12.5 at%).

IV.2.2.1 Lattice parameters

In the case of a hexagonal structure, such as ZnO wurtzite structure, we are interested in two parameters a=b and c. The analytical method used to calculate these parameters, is governed by the following formula:

$$sin^2\theta = {}^{\lambda^2}/_4\left[{}^4/_3\,(h^2 + hk + k^2)/a^2 + {}^{l^2}/_{c^2}\right] \qquad \textbf{(IV.1)}$$

where θ is the diffraction angle, λ is the wavelength of the incident Cu-Kα radiation (λ = 0.15406 nm) and h, k, l is the Miller indices.

From this formula, we can determine the lattice parameters a=b and c by taking into account the positions of their corresponding peaks (100) and (002), respectively. Then, we find:

$$a = \lambda / \sqrt{3}\, sin\theta_{100} \quad \textbf{(IV.2)}$$

and

$$c = \lambda / sin\theta_{002} \quad \textbf{(IV.3)}$$

Table IV.1 shows the lattice constants $a = b$ and c and their corresponding diffraction angle (2θ), full width at half maximum (FWHM) and peak intensity for pure and CZO thin films are calculated using XRD patterns**.** It is found that both $a = b$ and c are slightly decreased with Cu content for CZO thin films. This is due to incorporation of Cu into ZnO host lattice where the ionic radius of Cu^{2+}(0.73A˚) is slightly smaller than that of Zn^{2+} (0.74A˚).

Table IV.1: Lattice parameters ***a=b*** and ***c***, peak position and full width at half maxima (**FWHM**) as a function of doping rate, *x* (%), of Cu calculated from XRD diffractograms.of pure and CZO thin films (*x*= 1, 3.12, 6.25, 12.5 at%).

***x* (at %)**	**2θ (°) (002)**	**FWHM (°)**	**2θ (°) (100)**	**FWHM (°)**	**(hkl)**	**(hkl)**	**c (Å) (002)**	***a* (Å) (100)**
0	34.43	0.4731	31.81	0.4788	(002)	(100)	5.205	3.249
1	34.37	0.4141	31.73	0.3966	(002)	(100)	5.213	3.257
3.12	34.38	0.3982	31.72	0.4139	(002)	(100)	5.212	3.257
6.25	34.40	0.3664	31.75	0.3587	(002)	(100)	5.209	3.254
12.5	34.44	0.2498	31.75	0.2535	(002)	(100)	5.203	3.251

IV.2.2.2 Crystallite size

The average crystallite size (D) was estimated using the Scherrer formula:

$$D = K\lambda/\beta\cos\theta \quad \textbf{(IV.4)}$$

Where K is the shape factor (K=0.9), λ is the X-ray wavelength (λ=1.5406Å), β is the full width at half maxima of a given diffraction peak and θ is the Bragg angle **[17]**. In this case the most

intense peak (002) for 0,1,3.12,6.25 Cu% and (100) for 12.5 Cu % were used to estimate crystallite size.

Figure IV.2 exhibits the crystallite size value of pure and CZO thin films (*x*= 1, 3.12, 6,25 and 12.5 at%). The obtained crystallite size increases with increasing Cu doping. Similar behavior was also tabulated in the literature: Joshi et al. **[19]** observed an increase from 33.06 nm to 43.65 nm for Cu doping from 0 % to 10 %, Shewale et al. **[23]** estimated a crystallite size values of around 37.47 nm and 48.28 nm for undoped and 2 at.% CZO thin films, while Chen et al. **[24]** noticed an increase from 20 to 50 nm and then a decrease to 29 nm for Cu content of 2%, 6%, and 10%, respectively.

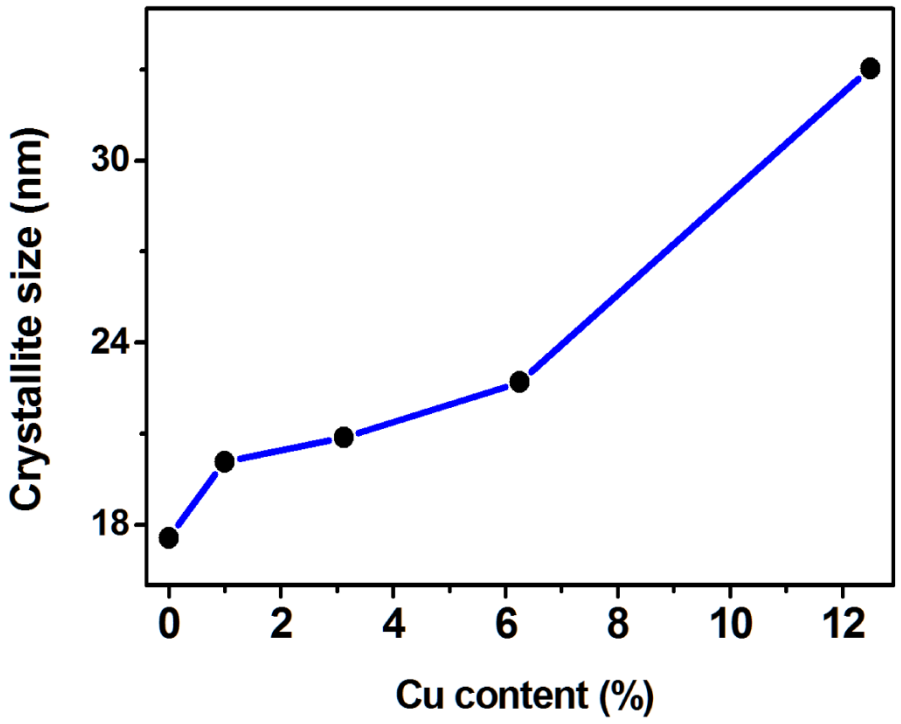

Figure IV.2. Crystallite size value of pure and CZO thin films (x= 1, 3.12, 6,25 and 12.5 at%).

IV.2.2.3 Strain

The lattice strain ε is estimated using the formula:

$$\varepsilon = \beta\cos\theta/4 \qquad \textbf{(IV.5)}$$

where β is the full width at half maximum of the corresponding peak and θ is the Bragg angle **[17]**.

Figure IV.3 shows the strain value of pure and CZO thin films (*x*= 1, 3.12, 6,25 and 12.5 at%). It is found that the undoped thin films possess a high strain value which goes on decreasing as *x* increases, suggesting that the films are getting relaxed due to replacement of the host (Zn^{2+}) by the dopant (Cu^{2+}) cations. Lee et al. **[25]**. observed the same behavior, who explained this phenomenon by the presence of excess Cu dopant located at grain boundaries.

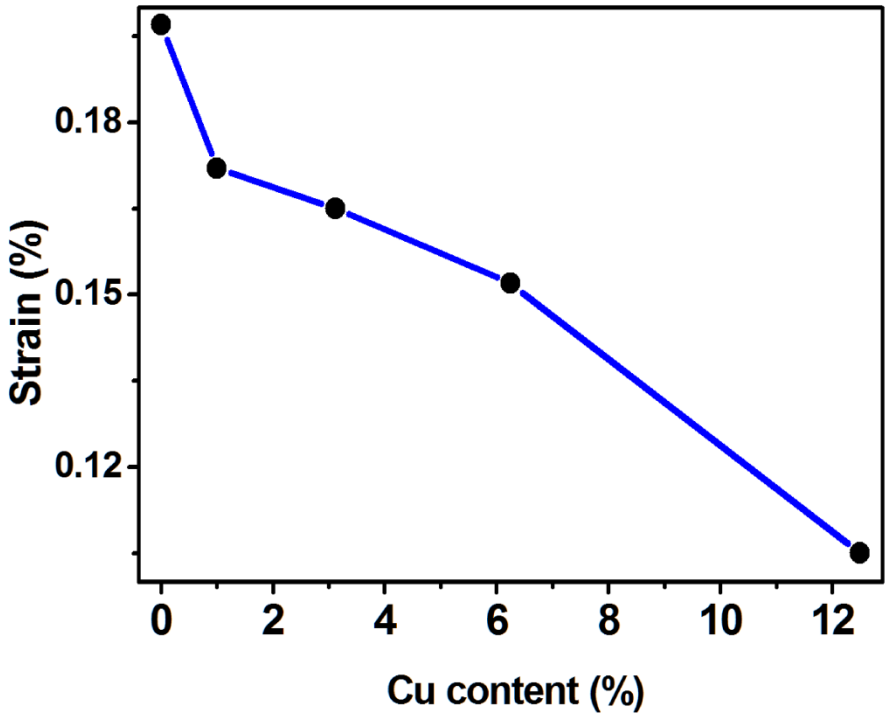

Figure IV.3. Strain value of pure and CZO thin films (x= 1, 3.12, 6,25 and 12.5 at%).

IV.2.2.4 Preferred orientation

To investigate the texture of a given plane, the texture coefficient ($TC_{(hkl)}$) is needed. It measures the relative degree of preferred orientation of a plane (*hkl*). This coefficient is estimated by using:

$$TC_{(hkl)} = I_{(hkl)}/I_{0_{(hkl)}}/\left(\sum_1^N I_{(hkl)}/I_{0_{(hkl)}}/N\right) \quad \textbf{(IV.6)}$$

where $I(hkl)$ and $I_0(hkl)$ are the measured relative intensity of a diffraction peak and the intensity of the standard powder diffraction peak taken from the JCPDS data, respectively,

and *N* is the number of diffraction peaks **[8]**. The higher values of *TC* (greater than unity) for a given (*hkl*) direction indicate the abundance of crystallites in this direction.

Figure IV.4 shows the TC values are as function of Cu doping for all peaks observed in the XRD pattern. It is observed that all films present highest TC values for (002) plane indicating a preferred growth along c-axis, which is converted to (100) plane for higher Cu content. This does mean that the degree of preferred growth orientation of the prepared thin films depends on the Cu concentration. Also, the higher value of texture coefficient reveals a better crystallinity of the prepared thin films. These findings are in agreement with **t**he obtained crystallite size.

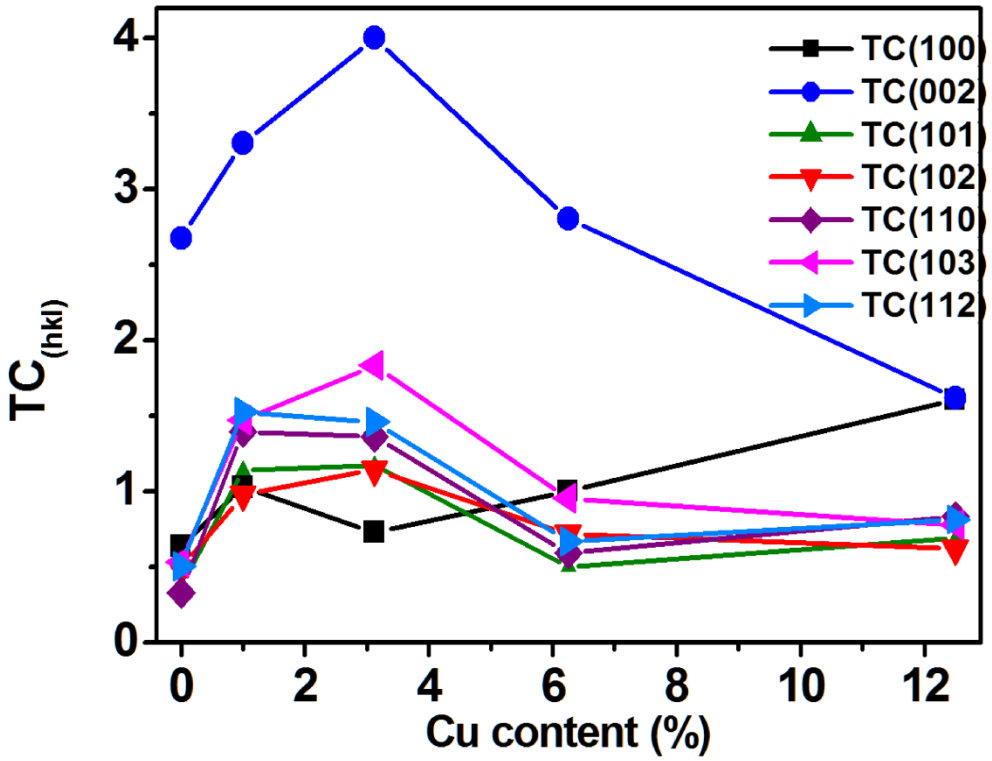

Figure IV.4. Texture coefficient variation of pure and CZO thin films (x= 1, 3.12, 6,25 and 12.5 at%).

IV.2.3 Surface morphology

It is well known that microstructure is important in many applications because the properties of the materials are closely related to their crystal size, morphology, and orientation **[44]**. In this section, the surface morphology of pure ZnO and CZO thin films were determined

by Field emission scanning electron microscopy (FESEM) and Atomic force microscopy (AFM). The crystal size, root mean squared roughness, and the growth mode are then deduced.

IV.2.3.1 Analysis by field emission scanning electron microscopy

Figures IV.5 f, g, h, i and **j** show the field emission scanning electron microscopy (FESEM) 2D images and their corresponding cross-sectional images of pure ZnO and CZO thin films with Cu content of 1, 3.12, 6,25 and 12.5 at %, respectively. All the FESEM images were obtained at 20,000× magnifications. It can be seen from these images that the morphology shows irregular sized aggregated clusters for pure ZnO, while it exhibits a randomly distributed mixer of spheroid-like and rod-like nanoparticles (granules) for CZO thin films. Moreover, the particles tend to agglomerate together to form large clusters by increasing *x*. The film thicknesses, estimated from cross-section images, were found to be about 318–357 nm, which seem slightly changed by Cu doping; 357(0%), 350(1%), 343(3.12%), 332(6.25%), 318(12.5 at %). These findings are in agreement with other previous results **[20, 45-47]**. Some other reports noticed no change in the film thickness with increasing level of Cu concentration **[24, 48]**.

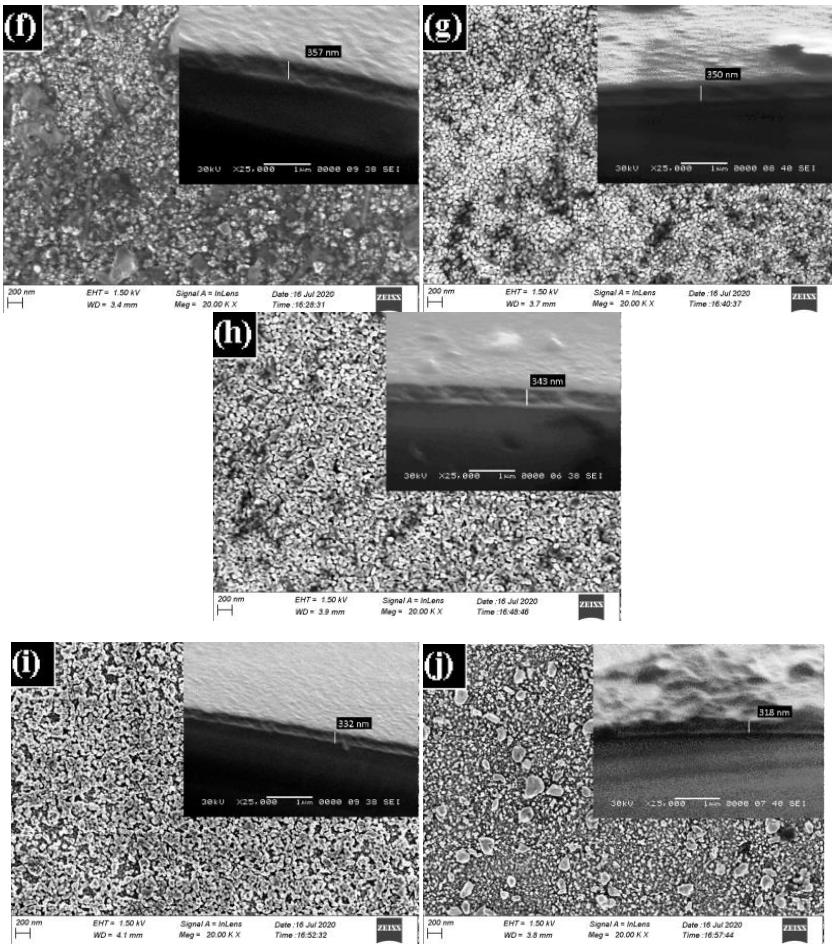

Figure IV.5. FESEM 2D images and their corresponding cross-sectional images of thin films for **(f)** x= 0 %, (g) 1 %, **(h)** 3.12 %, **(i)** 6.25 % and **(j)**12.5 at%.

IV.2.3.2 Analysis by atomic force microscopy

Figures IV.6a, b, c, d and **e** show the 1.0 X 1.0 μm^2 two and their corresponding three-dimensional AFM images for pure and CZO thin films with Cu content of 1, 3.12, 6,25 and 12.5 at%, respectively. The grains, extracted using WsXM software **[49]**, are round shape (two dimensional AFM images) and their average size increases with Cu doping **(Table IV.2)**. This is consistent with the changes occurred in (002) preferential orientation observed from XRD patterns, where the growth mode of grains translates from c-axis growth perpendicular to the substrate to the lateral one with increasing level of Cu doping.

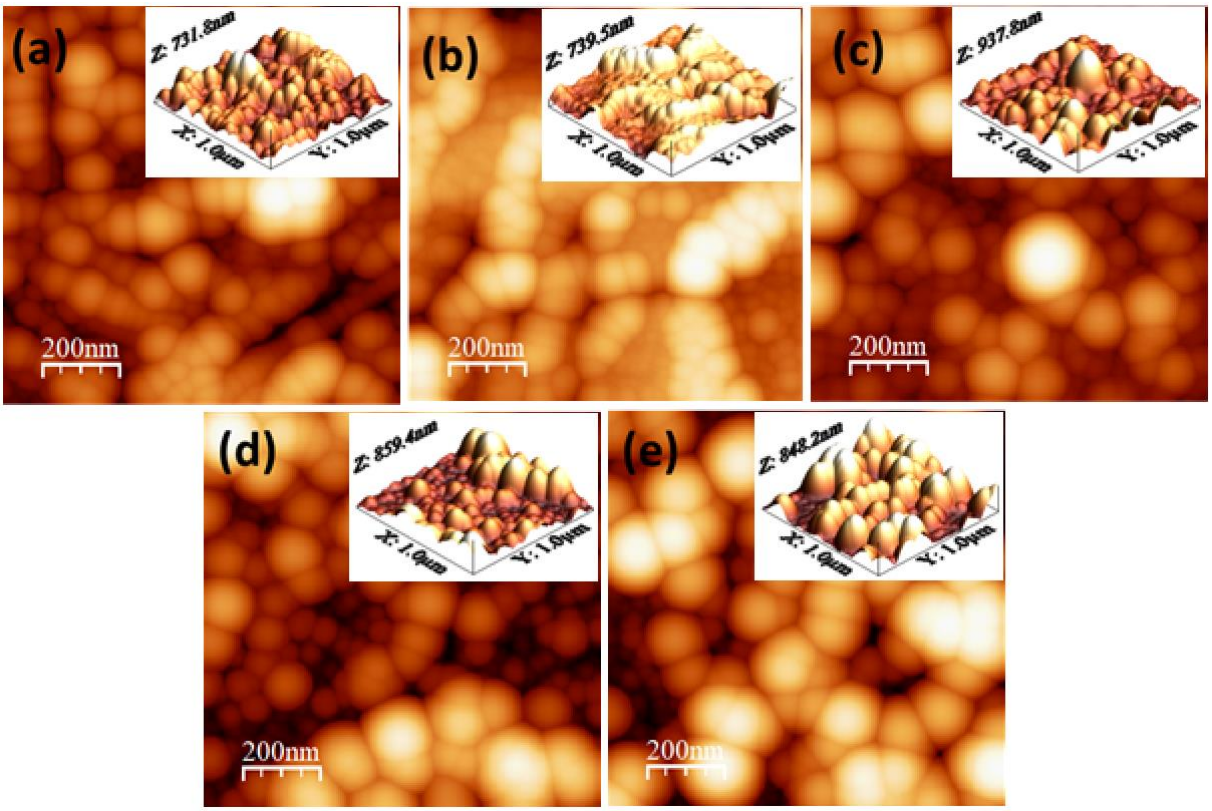

Figure IV.6. 1.0 X 1.0 μm^2 Two and three-dimensional AFM images of thin films for **(a)** x= 0 %, **(b)** 1 %, **(c)** 3.12 %, **(d)** 6.25 % and **(e)** 12.5 at%.

The pure ZnO films exhibit smooth surface. However, surface morphology is strongly influenced by the Cu doping and the surface becomes rough (three-dimensional AFM images), which is traduced by the increasing values of the root mean squared roughness (**Table IV.2**). The results of root mean squared roughness and average grain size are found to be consistent, i.e. thin films with small grain size exhibit a smooth surface. Joshi et al. **[19]** remarked an increase in both crystallite size and grain size and a decrease in strain with Cu doping. Sreedhar et al. **[18]** also reported results which exhibit a similar behavior except at high Cu concentration. Hashim et al. **[21]** reported that the type of substrate also affected the grain growth and shape. Salem et al. **[50]** noticed that the high doping concentration can lead to large grain size and rough surface morphology.

Table IV.2. Grain size and root mean squared roughness of pure and CZO thin films (*x*= 1, 3.12, 6.25, 12.5 at%).

***x* (at %)**	**Grain size (AFM) (nm)**	***Rrms* (nm)**
0	74.22	116.78
1	78.76	129.45
3.12	85.94	157.76
6.25	105.47	186.00
12.5	117.19	209.52

IV.2.4 Chemical composition

To confirm the presence of Cu in ZnO thin film, the energy dispersive spectroscopy (EDS) technique is usually used. EDX spectra of pure ZnO (Figure IV.7a) and CZO thin films with x= 6.25 at% **(Figure IV.7b)** and 12.5 at% **(Figure IV.7c)** are shown. The EDX spectrum of all samples exhibits an oxygen peak at around 0.529 keV and a Zinc peak at around 1.009 KeV. However, extra peak at around 0.939 KeV corresponding to the copper is also revealed together with the previous observed peaks for CZO thin films. Other peaks are also observed indicating the presence of other elements such as Si and C, which belong to the glass substrate and other residues. The significant decrease in Zn peak intensity with Cu doping is accompanied with the increase of its coinciding Cu peak intensity. Besides, the O peak intensity is still unchanged with Cu doping. This clearly suggests that Zn has been successfully substituted by Cu into the ZnO host lattice. Based on these findings, it is possible to suppose the stoichiometric films of the form Zn1-xCuxO **[20]**. Then, it is found from the quantitative analysis that the Cu concentrations of 8.56% and 10.81% are comparable to the actual Cu doping contents of 6.25% and 12.5% added during the preparation.

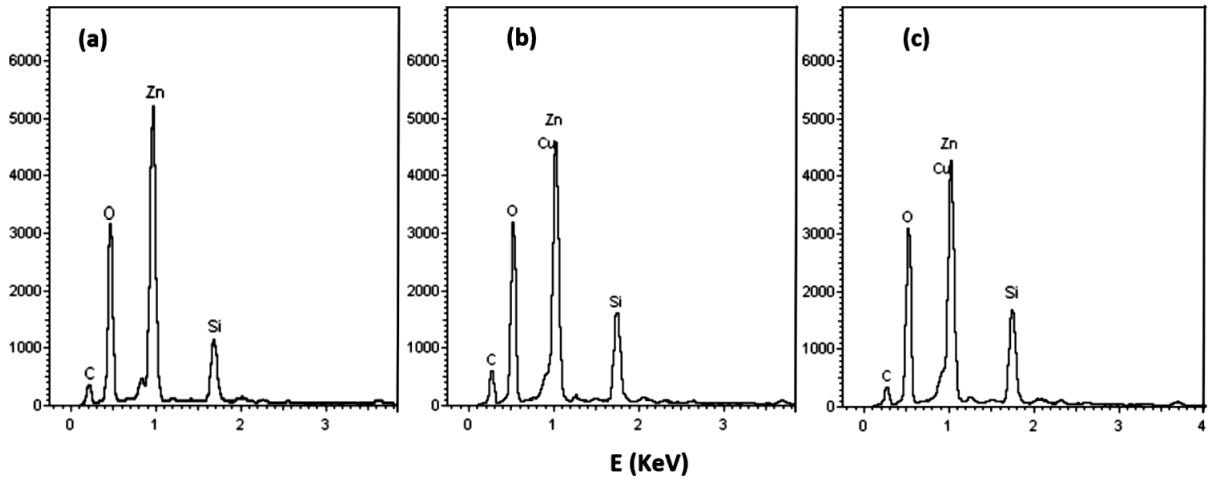

Figure IV.7. EDX spectra of pure ZnO (a) and CZO thin films; x= 6.25% (b), 12.5 at% (c).

IV.2.5 Optical properties

IV.2.5.1 Transmittance and reflectance spectra

The transmission and reflectance spectra of pure and CZO thin films with Cu content of 1, 3.12, 6,25 and 12.5 at%, are shown in the wavelength range 350–1000 nm (Figure IV.8), It can be seen that the transparency of films generally increases from 72% to 80% in the visible region with increasing of *x*. This is due to the increase of grain size with Cu doping, which leads to reducing the grain boundary density or scattering centers. Saidani et al. **[16]** found that the transmittance have increased from 77% to 92% when the concentration of Cu was increased from 0% to 5wt%. Sreedhar et al. **[18]** also measured a transmission greater than 83 % for Cu doping less than 6.2 at.% and transmission of 80% for Cu doping of 7.5 at.%.

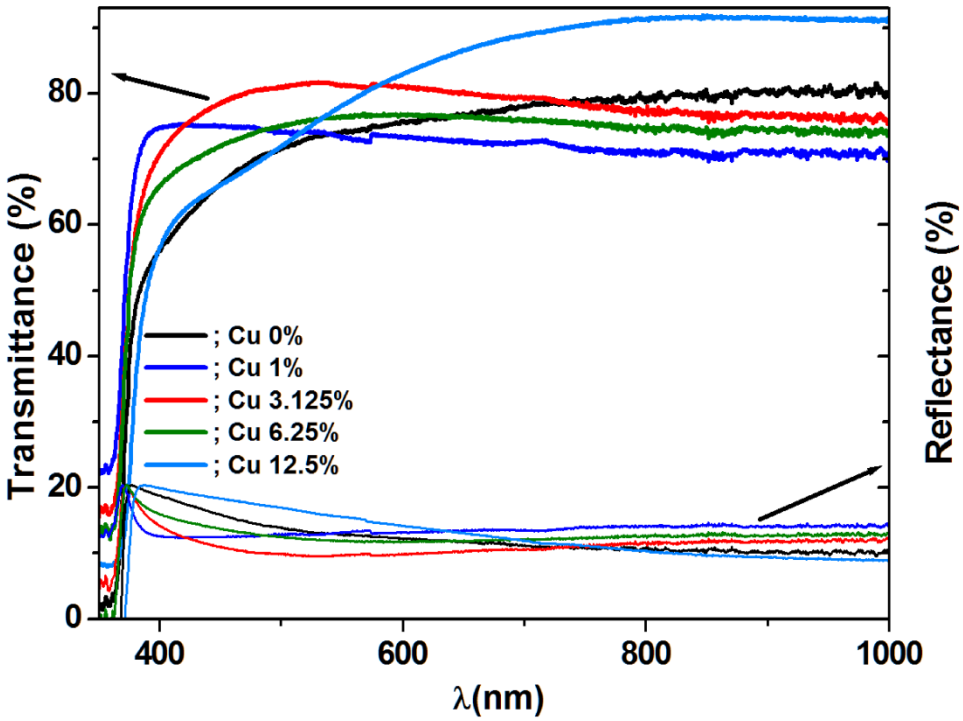

Figure IV.8. Optical transmittance and reflectance spectra of pure and CZO thin films with Cu content of 1, 3.12, 6,25 and 12.5 at%.

IV.2.5.2 Optical band gap

The transmission spectra of pure and CZO thin films in the wavelength range 350–1000 nm **(Figure IV.9)**, were also exploited to deduce the band gap *Eg* using the Tauc's equation **[51, 52]**:

$$\alpha h\nu = C(h\nu - Eg)^n \qquad \textbf{(IV.7)}$$

where n assumes the values 1/2, 2, 3/2 and 3 for the allowed direct, the allowed indirect, forbidden direct and forbidden indirect transitions, respectively, α is the absorption coefficient, C is a constant related to the extent of the band tailing, $h\nu$ is the photon energy and Eg is the optical band gap of the semiconductor.

The observed sharp absorption edge in the UV region (350-400 nm) for all films shifts to longer wavelengths by increasing Cu content leading to the decrease in the experimental band gap energy from 3.34 eV to 3.25 eV. Similar trend has been observed for ZnO thin films prepared at various Cu-doping range **[15, 17, 18, 20, 22, 24, 26, 50, 53-55]**.

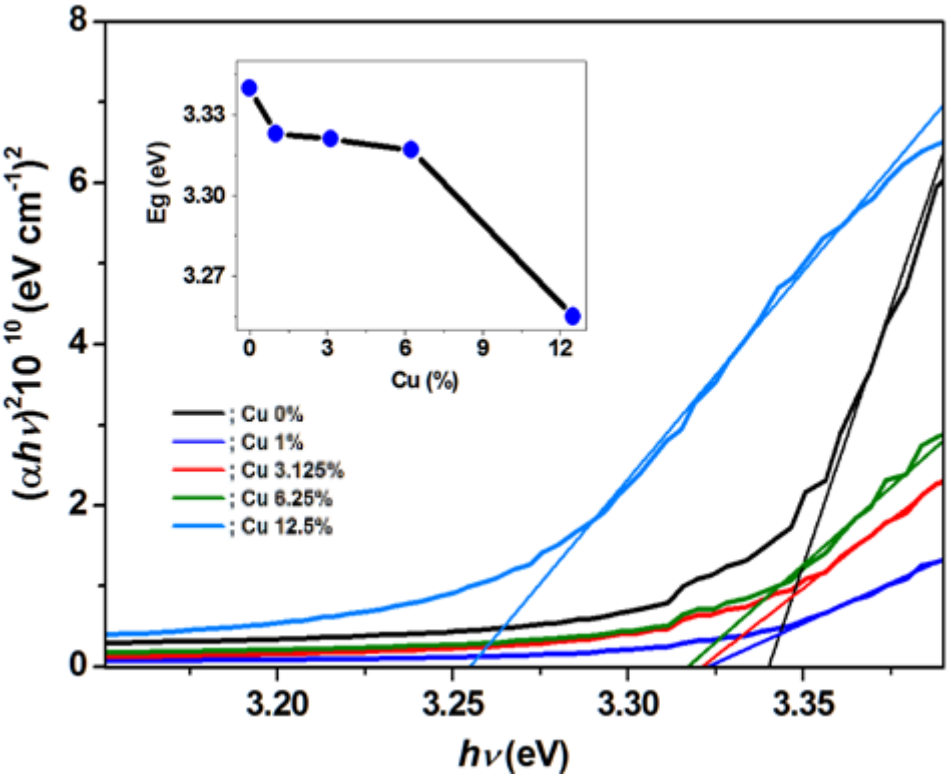

Figure IV.9. Extrapolation of the linear region of $(\alpha hv)^2$ as a function of photon energy hv. The band gap energy is extracted for pure and CZO thin films with Cu content of 1, 3.12, 6,25 and 12.5 at%.

According to Yan et al. **[56]**, the Cu 3d orbital is much shallower than the Zn 3d orbital. They noticed that the strong d-p coupling between Cu and O moves O 2p up with Zn substitution by Cu in ZnO and leads to narrowing the direct fundamental band gap.

IV.2.5.3 Optical parameters

The absorbance (**A**) of CZO thin films is calculated from measured transmittance (**T**) and reflectance (***R***) spectra **[57].**

$$A = 1 - R - T \qquad \textbf{(IV.8)}$$

The absorption coefficient α is then calculated for the sample **(Figure IV.10)** with thickness d as follows:

$$\alpha = 2.303\ \mathrm{A/d} \qquad \textbf{(IV.9)}$$

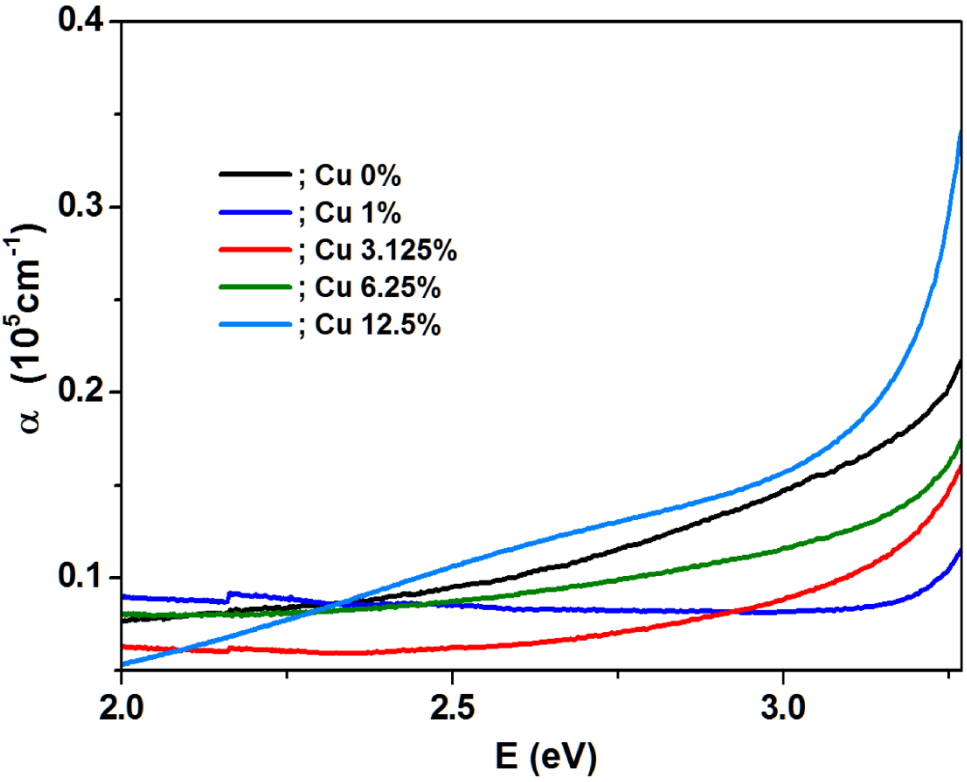

Figure IV.10. Absorption coefficient for pure and CZO thin films with Cu content of 1, 3.12, 6,25 and 12.5 at%.

For measurement with normal incidence of wavelength, λ, the extinction coefficient, ***k***, and the refractive index, *n*, of CZO thin film**,** Figure IV.11a, can then be determined from the surface of the sample by the following expressions:

$$k = \alpha\lambda/4\pi \qquad \textbf{(IV.10)}$$

$$n = (1+R)/(1-R) + \sqrt{4R/(1-R)^2 - k^2} \qquad \textbf{(IV.11)}$$

The dispersion formulae of DiDomenico and Wemple **[58]** is commonly used to calculate the refractive index in $E=hv < Eg$ range, where E is the photon energy. In such formulae the factors $1/(n^2-1)$ are plotted versus photon energy squared (E^2). Using straight line fitting technique to these plots **(Figure IV.11b)**, static refractive index $n_0=(1+E_d/E_o)^{1/2}$ (n_0 *equals* n when E~0, where E_d *and* E_o are the dispersion energy and the average oscillator energy, respectively) and static dielectric constant $\varepsilon_o = (n_o)^2$ are then estimated for CZO thin

films **(Inset in Figure IV.11b)**. E_o/Ed is the intercept of the straight line fitting and -1/(E_oEd) is its slope.

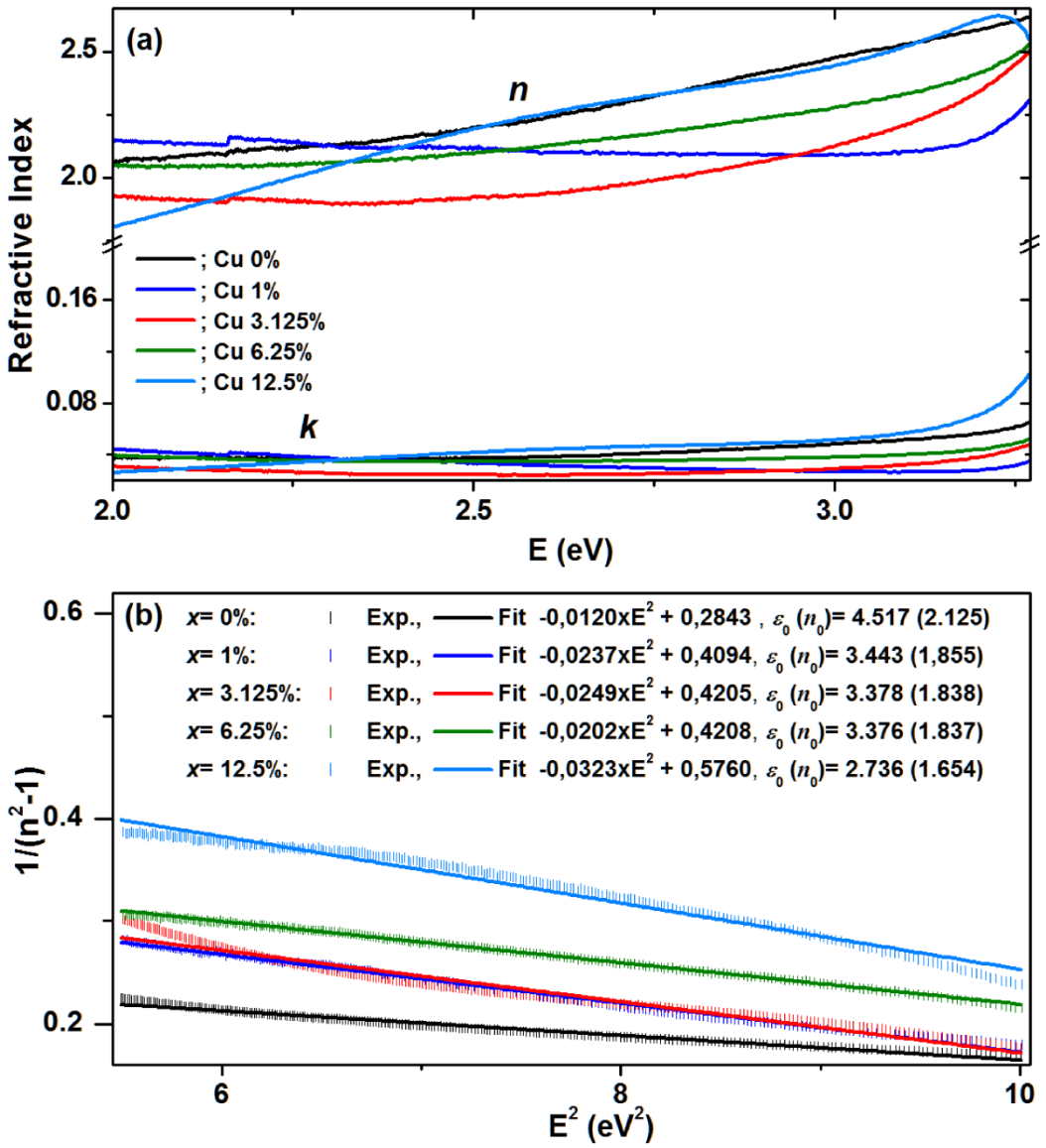

Figure IV.11. (a) complex refractive index, **(b)** 1/(n^2-1) versus photon energy squared (E^2) and its fitting for pure and CZO thin films with Cu content of 1, 3.12, 6,25 and 12.5 at%.

The real, ε_1, and imaginary, ε_2, parts of the complex dielectric function can also be estimated as:

$$\varepsilon_1 = n^2 - k^2 \quad \textbf{(IV.12)}$$

$$\varepsilon_2 = 2nk \quad \textbf{(IV.13)}$$

The dependence of the optical parameters (**ε_1** and **ε_2**) on the photon energy is presented for pure and CZO thin films **(Figure IV.12)**.

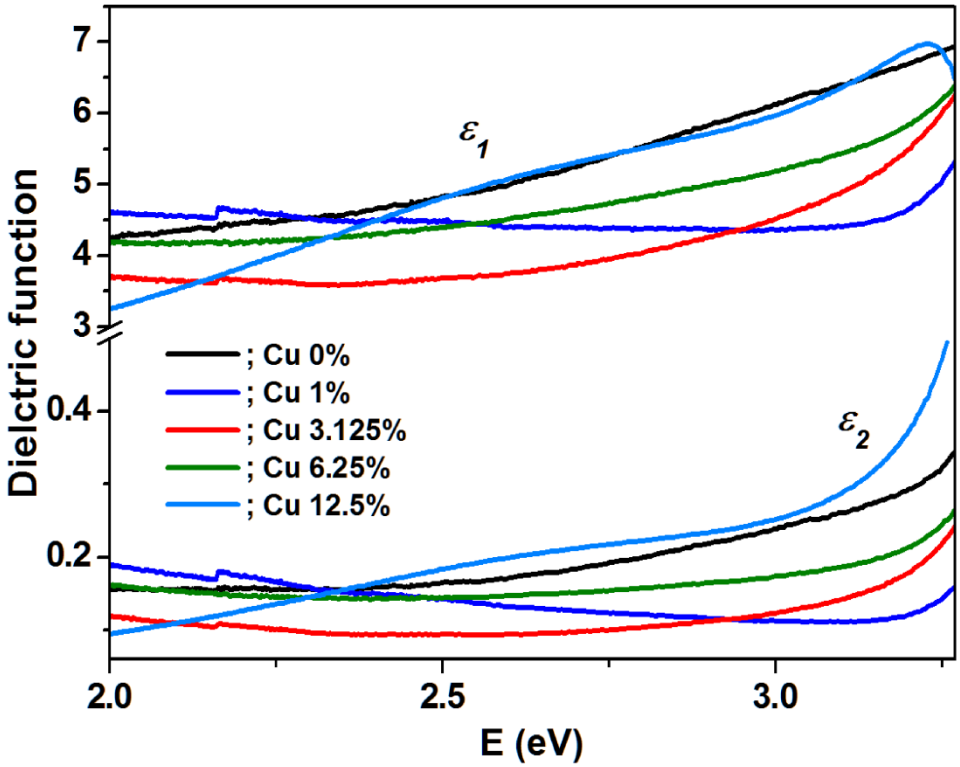

Figure IV.12. Complex dielectric function for pure and CZO thin films with Cu content of 1, 3.12, 6,25 and 12.5 at%.

The analysis shows that the value of absorption coefficient is still invariant with the increase in the incident energy for all thin films up to a certain value in the visible region (optical absorption edges) depending on the Cu doping. After that, α increases sharply and generally shifts to lower values of energy with Cu doping, which predicts a decrease in the band gap energy. The refractive index is found to be increased with energy in the visible light range and sensitive to Cu dopant concentration. Also, static refractive index n_0 decreases with Cu doping. This may be due to the decrease in film density caused by the increase in crystallite size (Figure IV.3). These findings are in agreement with those reported by other researchers for pure ZnO **[57, 59, 60]** and CZO thin films **[47]**. Furthermore, the dielectric function follow the same pattern as the refractive index from which is derived.

IV.3. Theoretical results

IV.3.1. Computational details

In this work, first-principles calculations of structural, electronic, magnetic and optical properties of pure and CZO wurtzite materials (*x*= 6,25%, 12.5 at%) were performed by DFT as implemented in CASTEP code (Cambridge Serial Total Energy Package: Commercialized by Accelrys) **[61]**.The generalized gradient approximation (GGA) in the scheme of Perdew–Burke–Ernzerhof (PBE) was employed to describe the exchange-correlation function **[62]**. 2x2x4 and 2x2x2 ZnO supercell model, derived from the optimized ZnO unit cell **(Figure IV.13a)**, and substitutional method **[63]** were used to achieve the considered Cu content of 6,25% and 12.5 at%, respectively **(Figure IV.13b)**. The Brillouin zone corresponding to Cu content of 12.5 at% with the points of high symmetry labeled is also shown **(Figure IV.13c)**. The valence-electron configurations for the O, Zn and Cu atoms are chosen as $2s^2\ 2p^4$, $3d^{10}\ 4s^2$ and $3d^{10}\ 4s^1$, respectively. The energy cut-off was fixed at 400 eV, which is enough to perform the present calculation with plane-wave ultrasoft pseudopotential method **[64]**. The Brillouin zone is sampled by a gamma-centered k-point meshes of 3x3x1 and 5x5x3 for 2x2x4 and 2x2x2 ZnO supercell, respectively. It is worth noting that the usual way for obtaining an appropriate cut-off energy and k-points for a given structure and set of pseudopotentials, is performed over two steps. The first step consists in establishing a convergence test for cut-off energy (Ecut), using a single k-point, by means of a series of calculations with increasing Ecut until the total energy of structure converges towards a fixed value. Then, a similar test is perform to determine the appropriate number of k-points to use. This is done by increasing the density of the k-point grid, keeping fixed the Ecut. The values of cut-off energy and k-points in our calculation are based on convergence test established in previous studies **[41, 65]**.The optimization convergence for maximum force, energy change, maximum displacement and maximum stress were fixed at 0.05 eV/Å, 5×10^{-6} eV/atom, 10×10^{-4} Å and 0.05 GPa, respectively. The SCF convergence threshold was $5.0\ 10^{-6}$ eV/atom.

The semiempirical LDA+U approach **[27]** was used with effective Hubbard U values of 5.5, 6.0 and 8.0 eV for Zn *3d, Cu 3d and O 2p* electrons, respectively. Furthermore, ferromagnetic phase of CZO (*x*= 6.25% and 12.5 at%) was adopted in which two Cu atoms substitute two Zn atoms according to five different geometry configurations (Figure IV.13b); for *x*=12.5 at%, the first Cu atom is taken to be fixed and the other Cu atom changes its place. The ferromagnetic phase adopted here was supported by previous studies **[36, 66]**.

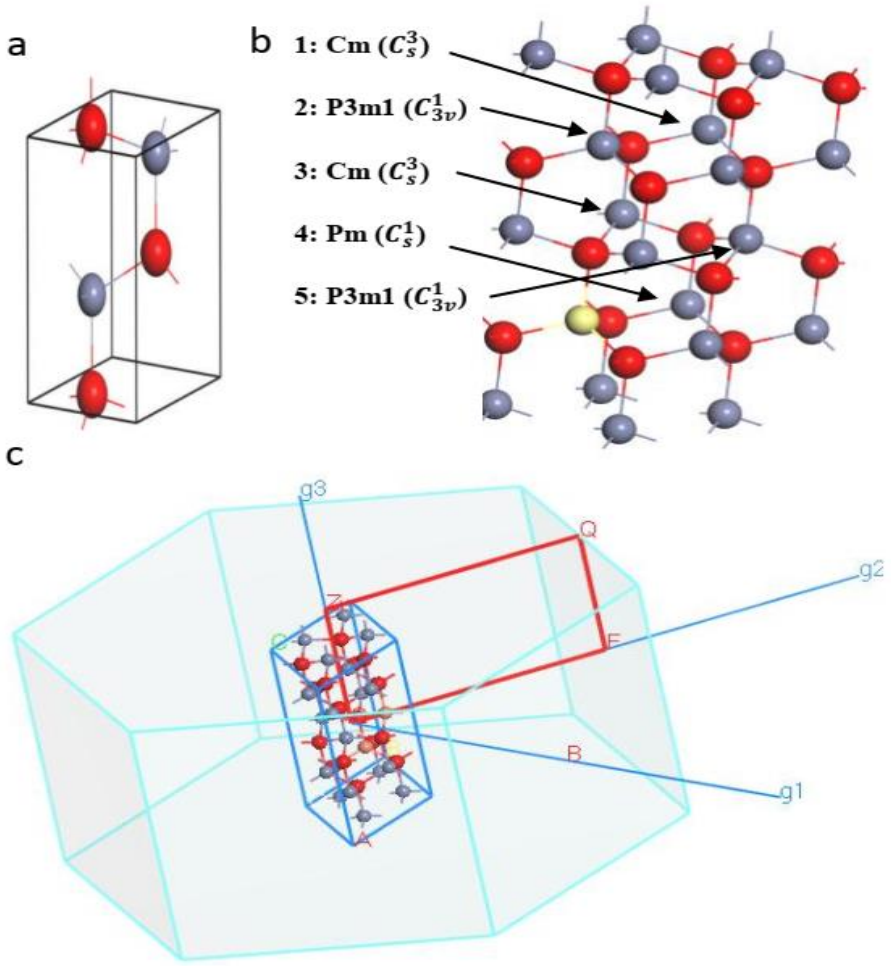

Figure IV.13. (a) ZnO unit cell, **(b)** 2x2x2 ZnO supercell; O atoms are in red, the first Cu atom (yellow) is taken to be fixed and the second one substitutes Zn atom (gray) at different geometry configurations for x=12.5 at%, (c) Brillouin zone with the points of high symmetry labeled. (Cells were constructed using the Materials Visualizer within the Materials Studio environment).

IV.3.2. Copper doped zinc oxide structure

Based on previous experimental **[20]** and theoretical **[67]** findings it is possible to suppose the stoichiometric films of the form $Zn_{1-x}Cu_xO$. This suggests that Zn has been successfully substituted by Cu into the ZnO host lattice, which is well confirmed by our EDX results (see experimental part). The difference in total energy ($\Delta E_i = E_i - E_3$; $i = 1,..5$) corresponding to third geometry configuration (E_3), taken as an energy reference, is estimated for the various geometry configurations from substitution of Zn by Cu, marked as 1, 2, 3, 4 and 5. The values of ΔE_i are summarized for CZO (x= 12.5 at%) as follows ; $\Delta E_1 = 0.5\ meV$, $\Delta E_2 = 4.1\ meV$, $\Delta E_3 = 0.0\ meV$, $\Delta E_4 = 17.6\ meV$ and $\Delta E_5 = 2.0\ meV$ corresponding to the distance between two Cu atoms ($d_i = d_{Cu_{Fix}-Cu_i}$; $i = 1,..5$, Cu_{Fix} denotes fixed Cu atom) $d_1 = 6.112$ Å, $d_2 = 5.181$ Å , $d_3 = 3.199$ Å, $d_4 = 3.243$ Å

and $d_5 = 4.552$ A°, respectively **(Figure IV.14)**. This does mean that the third configuration (symmetry group Cm (C_s^3)) is the more stable state (ground state) where Cu atoms are at a short distance around the O atom. This agrees with the results reported by Estrada et al. **[66]**, Nayek et al. **[34]** and Wang et al. **[40]**. The configuration corresponding to the stable state will also be considered for studying the effect of the Hubbard U values on the band gap energy.

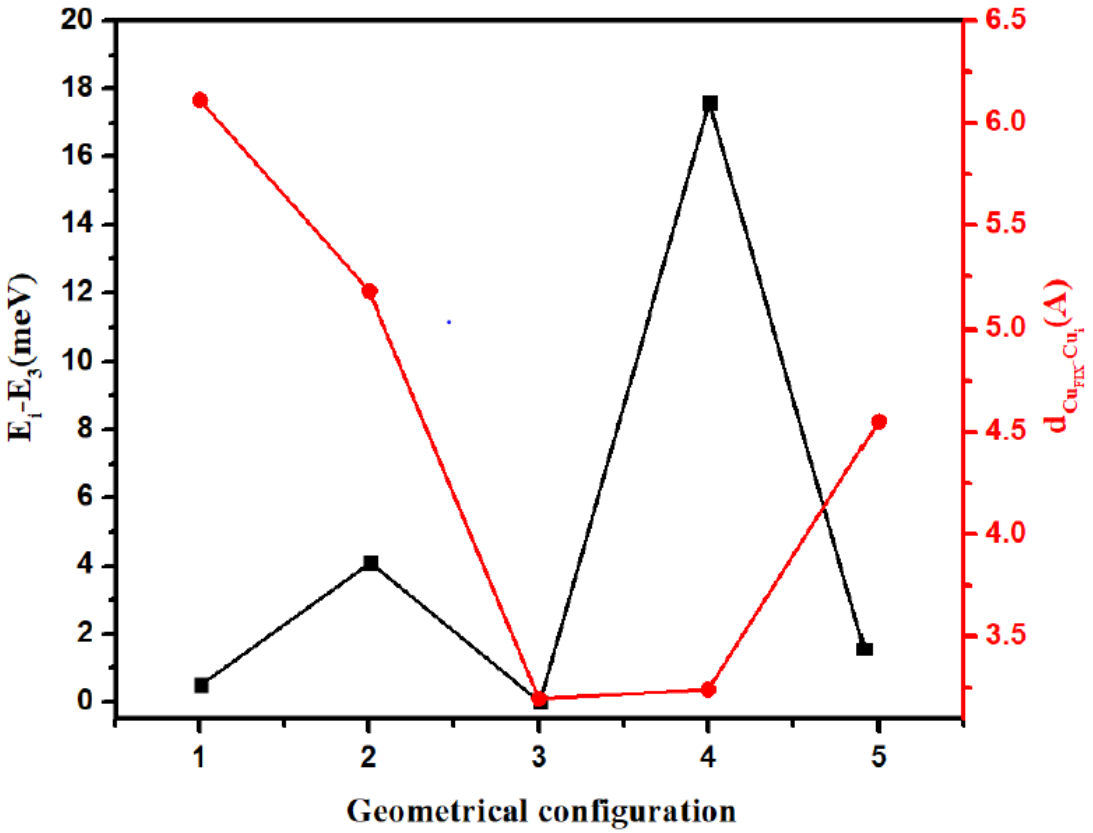

Figure IV.14. Variation of the total energy and distance between two Cu atoms for different geometry configurations. The energy corresponding to third configuration is chosen as an energy reference.

IV.3.3 Structural properties

Lattice parameter of pure and CZO wurtzite structures (*x*= 6,25 and 12.5 at%) are calculated by performing a geometry optimization as outlined in section III.9. Unlike the optimized lattice constant, *a=b*, the lattice constant *c* is slightly decreased with Cu concentration **(Table IV.3)**. Both optimized lattice constants exhibit an excellent comparison to the experimental ones; the maximum relative deviation is 0.46% and 0.21% for a=b and c, respectively. The decrease in lattice constant c is consistent with our results extracted from XRD patterns. This decrease has been also observed by Zhao et al. **[41]**. In addition, the bond

length was slightly changed when going from pure ZnO to Cu-doped structure, because of the comparable sizes of Zn and Cu atoms. Similar change has been found by Nayek et al. **[34]**.

Table IV.3: Bond length and lattice constants of pure and CZO wurtzite structures (*x*= 6,25 and 12.5 at%).

x (at %)	Bond length (A°)		Lattice constants (A°)	
	Zn-O	**Cu-O**	***a=b***	***c***
0	1.9717	-	3.236	5.204
6.25	1.9721	1.9785	3.239	5.199
12.5	1.9724	1.9791	3.243	5.192

IV.3.4 Electronic properties

IV.3.4.1 Hubbard correction and energy band gap

Based on previous studies **[28, 31-33]**, we focus on the effective Hubbard U values for *Cu 3d* state, which was found to be distributed around Fermi level and it was responsible for the shrinking of the band gap. The increase of effective Hubbard U values for *Cu 3d* state tends to enhance significantly the calculated electronic energy gap (*E*g) compared to that deduced from experiment; U *Cu 3d*= 6, 8 and 10 eV give *E*g= 1.860, 2.537 and 3.315 eV, respectively, for Cu-doped ZnO (x=12.5%). Furthermore, U *Cu 3d*= 10 eV gives *E*g= 3.380 and 3.328 eV for pure and Cu-doped ZnO (x=6.25 at%) **(Table IV.4)**. This enhancement in *E*g is due to the improved localization of *Cu 3d* states. Then, the effective Hubbard U values of 5.5, 10 and 8eV for Zn *3d, Cu 3d and O 2p* electrons, respectively, will be taken into account to evaluate the theoretical properties of the CZO structure. Earlier calculations of band gap have been reported in the literature **[31, 32, 34-39, 41]**, but most of them exhibited underestimation of the experimental band gaps of semiconductors. So, further calculations with convenient Hubbard U values are still justified to enhance the band gap.

Table IV.4: Variation of the calculated band gap energy according to U *Cu 3d* values for pure ZnO and Cu-doped ZnO structures (Cu content : 6.25% and 12.5 at%).

Structure	U *Cu 3d* (eV)	*Eg* (eV) Theo.	*Eg* (eV) Exp.
Cu-doped ZnO (x=12.5 at%)	6	1.86	3.251
	8	2.537	
	10	3.315	
Cu-doped ZnO (x=6.25 at%)	10	3.328	3. 317
Pure	10	3.380	3.340

In addition, the present findings of band gap from theoretical calculation are in good agreement with the present experimental values (maximum relative deviation does not exceed 1.96%), in which a direct band gap is observed for pure and CZO structure **(Figure IV.15 left)**. It confirms that the Cu doping can induce narrowing in the band gap where the bottom of the conduction band is mainly originated from Cu spin down states while Cu spin up states shift deeply into the bottom of the valence band **(Figure IV.15 right)**. This has also been observed by Fang et al. **[36]**.

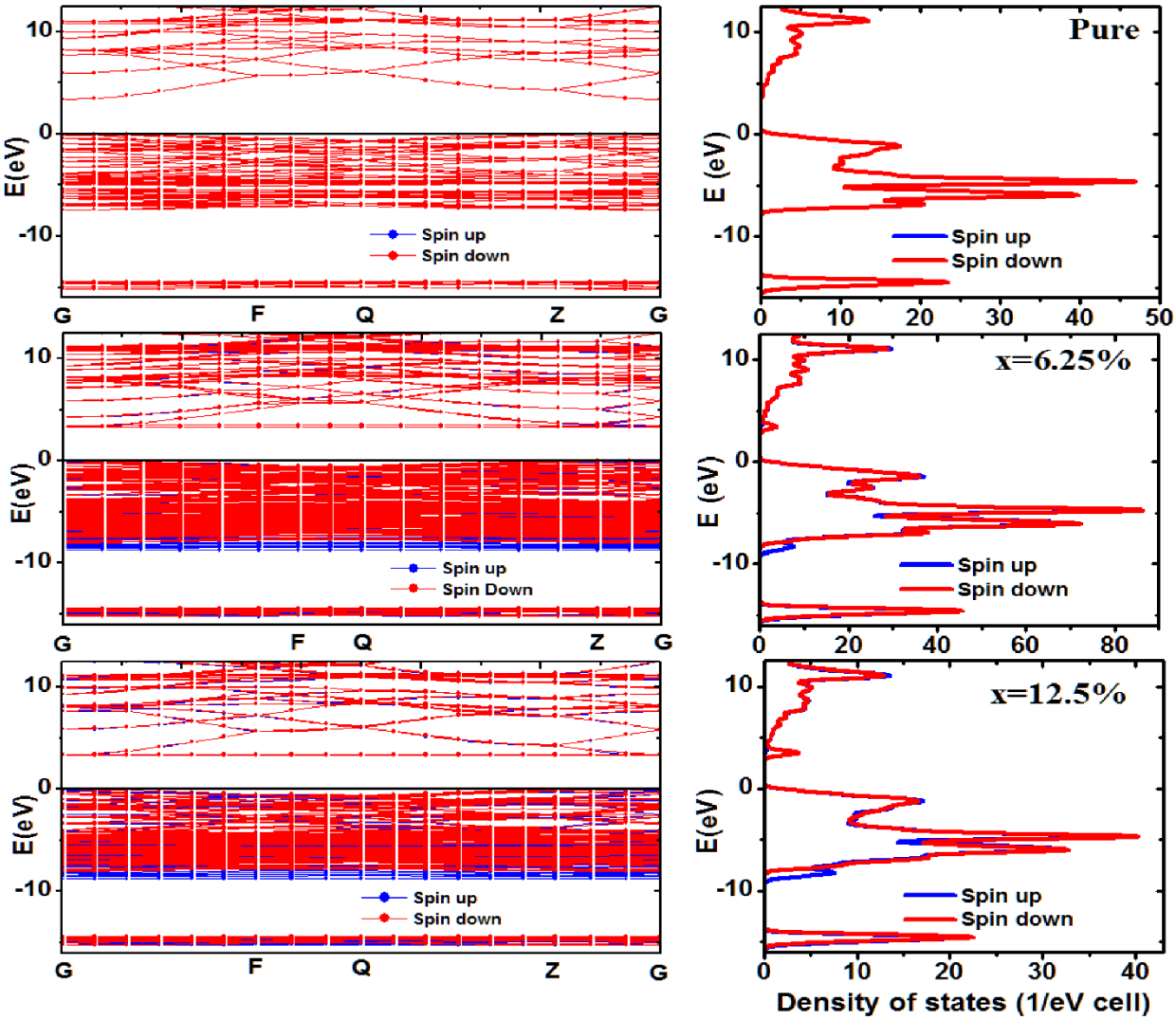

Figure IV.15. Band structures (left panels) and their corresponding spin up (blue) and spin down (red) total density of states (right panels) of pure and CZO wurtzite structures (x= 6,25%, 12.5 at%).

IV.3.4.2 Density of states

The density of states (DOS) of a system describes the proportion of states that are to be occupied by the system at each energy. The DOS for a given band *n*, $N_n(E)$, is defined as:

$$N_n(E) = \int \frac{d\boldsymbol{k}}{4\pi^3} \delta(E - E_n(\boldsymbol{K})) \qquad \textbf{(VI. 14)}$$

where $E_n(\boldsymbol{K})$ describes the dispersion of the given band and the integral is determined over the Brillouin zone. An alternative representation of the density of states is based on the fact that $N_n(E)dE$ is proportional to the number of allowed wave vectors in the *n*th band in the energy

Range E to $E + dE$. The total density of states, $N(E)$, is obtained by summation over all bands. The integral of N(E) from minus infinity to the Fermi level gives the total number of electrons in the unit cell. In a spin-polarized system, separate DOS for electrons with spin up and spin down can be introduced. Their sum produces the total DOS and their difference is referred to as the spin density of states.

The partial density of Zn 4s, Zn 3d, Cu 4s, Cu 3d, O 2s and O 2p spin up and down states (PDOS) for pure and CZO wurtzite structures (*x*= 6,25%, 12.5 at%) are shown **(Figure IV.16)**. The valence band states is mainly originated from a strong mixing among the Zn3d and O2p states. The valence band states are extended down to -7.8 eV and -9.2 eV for pure and CZO structure, respectively, while Cu3d states contribution is appeared in the bottom of valence band for the doped case. This large region is followed by a narrow band, centered at -14.6 eV and unaffected by Cu doping, which is mainly originated from O2s orbitals with a weak mixing between the Zn3d and Zn4s states. The downward shift of the conduction band, dominated by Zn4s with a little contribution of Cu3d states near the Fermi level **(Inset in Figure IV.16)**, leads to the decrease of the optical band gap with the increase of *x*. It is also found that Cu3d states were found to be distributed around Fermi level for Cu-doped structures (*x*= 6,25%, 12.5 at%) with ferromagnetic phase in which Cu atoms are close to each other around the O atom.

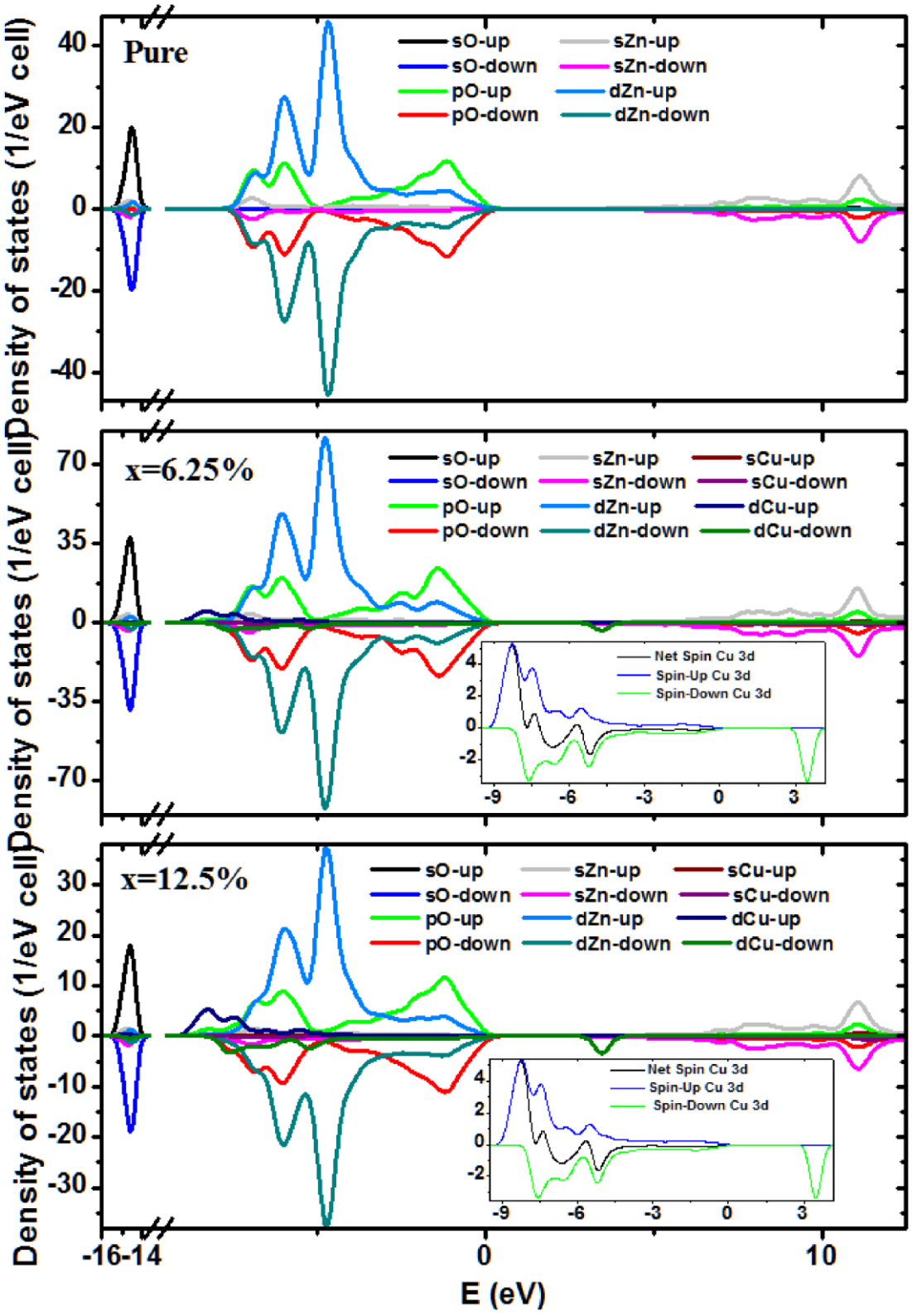

Figure IV.16. PDOS of Zn 4s, Zn 3d, Cu 4s, Cu 3d, O 2s and O 2p spin up and down states. Insets in PDOS show Cu 3d spin up, spin down and net spin states near Fermi level for CZO wurtzite structures (x= 6,25%, 12.5 at%).

IV.3.4.3 Charge density and mulliken population analysis

Population analysis in CASTEP is performed by a projection of the plane wave (PW) states onto a localized basis using a technique described by Sanchez-Portal et al. **[68]**. Population analysis of the resulting projected states is then performed using the Mulliken formalism **[69]**. This technique is widely used in the analysis of electronic structure calculations performed with LCAO basis sets. In Mulliken analysis the charge associated with a given atom, *A*, is determined by:

$$Q(A) = \sum_k \omega_k \sum_\mu^A \sum_v P_{\mu v}(\boldsymbol{k}) S_{v\mu}(\boldsymbol{k}) \quad \textbf{(VI. 15)}$$

and the overlap population between two atoms, *A* and *B*, is:

$$n(AB) = \sum_{\boldsymbol{k}} \boldsymbol{\omega_k} \sum_{\boldsymbol{\mu}}^{\boldsymbol{A}} \sum_{\boldsymbol{v}}^{\boldsymbol{B}} P_{\boldsymbol{\mu v}}(\boldsymbol{k}) S_{\boldsymbol{v\mu}}(\boldsymbol{k}) \quad \textbf{(VI. 16)}$$

where $S_{v\mu}(\boldsymbol{k})$ is the overlap matrix of the localized basis set:

$$S_{\boldsymbol{v\mu}}(\boldsymbol{k}) = \langle \emptyset_{\boldsymbol{\mu}}(\boldsymbol{k}) | \emptyset_{\boldsymbol{v}}(\boldsymbol{k}) \rangle \quad \textbf{(VI. 17)}$$

and $P_{\mu v}(\boldsymbol{k})$ is the density matrix for the atomic states ($\emptyset_{\boldsymbol{\mu}}$), calculated as follows:

$$P_{\boldsymbol{\mu v}}(\boldsymbol{k}) = \langle \emptyset_{\boldsymbol{\mu}} | \hat{\rho}(\boldsymbol{k}) | \emptyset_{\boldsymbol{v}} \rangle \quad \textbf{(VI. 18)}$$

where $\hat{\rho}(\boldsymbol{k})$ is he density operator which may be defined as:

$$\hat{\rho}(\boldsymbol{k}) = \sum_{\boldsymbol{\alpha}}^{\boldsymbol{Occ}} n_\alpha | \chi_\alpha(\boldsymbol{k}) \rangle \langle \chi^\alpha(\boldsymbol{k}) | \quad \textbf{(VI. 19)}$$

with n_α are the occupancies of the PW states, $|\chi_\alpha(\boldsymbol{k})\rangle$ are the projected PW states $\hat{p}(\boldsymbol{k}) | \psi_\alpha(\boldsymbol{k}) \rangle$ and $|\chi^\alpha(\boldsymbol{k})\rangle$ are the duals of these states:

$$|\chi^\alpha(\boldsymbol{k})\rangle = \sum_v S_{\alpha v}^{-1} |\chi_v(\boldsymbol{k})\rangle \quad \textbf{(VI. 20)}$$

and $\hat{p}(\boldsymbol{k})$ is the projection operator of Bloch functions with wavevector **k** generated by the atomic basis set:

$$\hat{p}(\boldsymbol{k}) = \sum_\mu | \emptyset_{\boldsymbol{\mu}}(\boldsymbol{k}) \rangle \langle \emptyset_{\boldsymbol{\mu}}(\boldsymbol{k}) | \quad \textbf{(VI. 21)}$$

The charge density difference, with respect to a linear combination of the atomic densities, of slice containing Cu atoms and their neighbors ((010) surface) for pure and CZO structures, is mapped **(Figure IV.17)**. Blue, yellow and red colors indicate a region with charge accumulation (around O atom), minimal difference and charge loss (around Zn or Cu atom),

respectively. The charge density difference demonstrates that the atom with high electronegativity tends to attract more electrons and vice versa (Zn:1.7, Cu:1.8 and O :3.5).

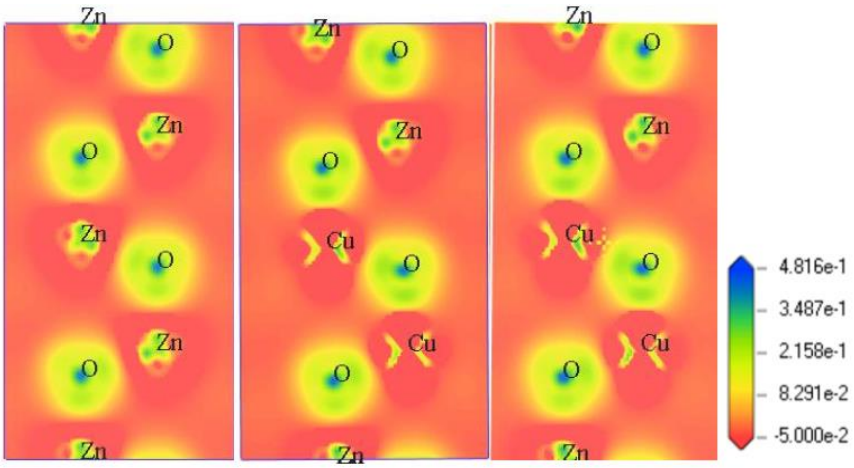

Figure IV.17. Distribution (010) surface of charge density difference for pure and CZO structures.

This is consistent with the values of the average Mulliken atomic and bond populations (**Table IV.5**). The difference between the formal ionic charge and the calculated effective valence charge refers to the mix of ionic and covalent bonding in both pure and CZO structures (*x*= 6,25%, 12.5 at%) with more covalency for Cu-O bonds than Zn-O ones. This covalency decreases with Cu doping.

Table IV.5: Average Mulliken population atomic, effective valence and bond populations of pure and CZO wurtzite structures (*x*= 6,25 and 12.5 at%).

***x* (at %)**	**Atomic Population (e)**			**Effectivevalence(e)**		**Bond Population (e)**	
	Zn	**Cu**	**O**	**Zn**	**Cu**	**Zn-O**	**Cu-O**
0	0.950	-	-0.950	1.050	-	0.402	-
6.25	0,967	0.690	-0.949	1.033	1.310	0.397	0.430
12.5	0.985	0.705	-0.949	1.015	1.295	0.395	0.425

IV.3.5 Magnetic properties

Spin-polarized calculations indicate that the Cu doping induces a magnetic moment of about 0.96 μ_B/Cu with a small contribution from its nearest-neighboring O atoms (0.04 μ_B/O) (**Figure IV.18a**). Magnetic moment value from our calculation is in agreement with that deduced from exchange split and crystal field theories. The splitting of the Cu^{+2} d-states in the wurtzite structure (Cu atom is tetrahedrally surrounded by four oxygen atoms) is due to exchange split into spin up and spin down states and crystal field split into a double and a triplet (**Figure IV.18b**)**.** This configuration leads to a net spin equal 1 μ_B/Cu **[70].**

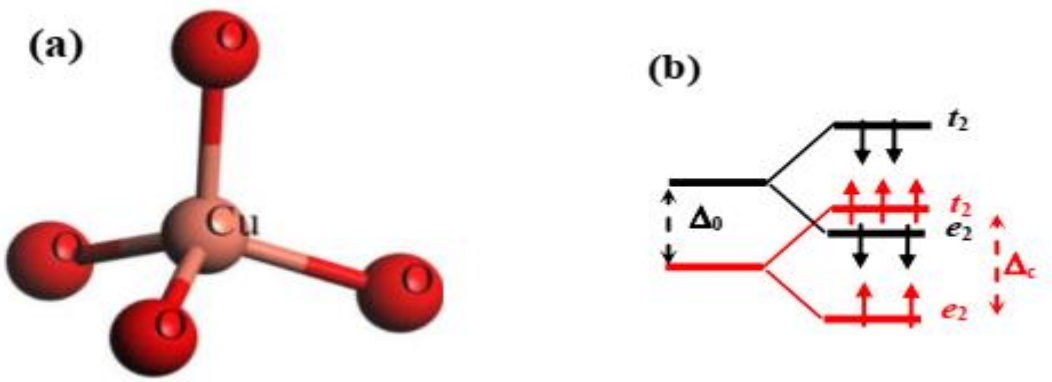

Figure IV.18. (a) Oxygen atoms are arranged with tetrahedral symmetry around copper atom in the wurtzite structure, **(b)** exchange splitting (**Δ_0**) and crystal field splitting **(Δ_c)** into a doublet (e_2) and a triplet (t_2) Cu^{+2} ***d***-states.

IV.3.6 Optical properties

It is useful to know the different ways in which light interacts with matter and modifies its direction and/or intensity. The dielectric function is an essential parameter to describe the behavior of matter subjected to the effect of an external electromagnetic excitation (light). It represent the ratio of the permittivity of a substance to the permittivity of the vacuum and is defined as **[71, 72]**:

$$\varepsilon(\omega) = \varepsilon_1(\omega) + i\varepsilon_2(\omega) \qquad \textbf{(VI. 22)}$$

The imaginary part of the dielectric function $\varepsilon_2(\omega)$ is calculated from the momentum matrix elements $P_{nn'}(k)$ between the occupied $|nk\rangle$ states (with energy $E_n(k)$) and unoccupied $|nk'\rangle$ states (with energy $E_{n'}(k)$) as follows:

$$\varepsilon_2(\omega) = \frac{8}{3\pi\omega^2}\sum_{nn'}\int_{BZ}|P_{nn'}(K)|^2\frac{dS_K}{\nabla\omega_{nn'}(K)} \quad \textbf{(VI. 23)}$$

where $\omega_{nn'}(k) = E_n(k) - E_{n'}(k)$ and S_k is an equi-energetic surface.

The real part $\varepsilon_1(\omega)$ can be extracted from Kramers-Kroning relationship **[28, 73]**:

$$\varepsilon_1(\omega) = 1 + \frac{2}{\pi}P\int_0^{\infty}\frac{\omega'\varepsilon_{2(\omega')}}{\omega'^2-\omega^2}d\omega' \quad \textbf{(VI. 24)}$$

where P is the principal value of the integral.

$$P = \lim_{a\to 0}\int_{-\infty}^{\omega-a}\frac{\varepsilon(\omega')}{\omega'-\omega}d\omega' + \lim_{a\to 0}\int_{\omega-a}^{+\infty}\frac{\varepsilon(\omega')}{\omega'-\omega}d\omega' \quad \textbf{(VI. 25)}$$

The refractive index is one of the most important optical constants. When an electromagnetic wave loses energy during its propagation, this last index becomes complex; the real part is usually the refractive index n, and the imaginary part is known as the extinction coefficient k:

$$n(\omega) = \left[\frac{\varepsilon_1(\omega)}{2} + \frac{\sqrt{\varepsilon_1(\omega)^2+\varepsilon_2(\omega)^2}}{2}\right]^{1/2} \quad \textbf{(VI. 26)}$$

$$k(\omega) = \left[\frac{\sqrt{\varepsilon_1(\omega)^2+\varepsilon_2(\omega)^2}}{2} - \frac{\varepsilon_1(\omega)}{2}\right]^{1/2} \quad \textbf{(VI. 27)}$$

Thus, three other parameters necessary to describe the behavior of materials subjected to the effect of an external light excitation; these are the reflectivity $R(\omega)$, the optical loss $L(\omega)$, and the absorption coefficient $I(\omega)$ which are given by the following expressions:

$$R(\omega) = \left|\frac{\varepsilon^{1/2}(\omega)-1}{\varepsilon^{1/2}(\omega)+1}\right|^2 \quad \textbf{(VI. 28)}$$

$$L(\omega) = -Im\left(\frac{1}{\varepsilon(\omega)}\right) = \frac{\varepsilon_2(\omega)}{\varepsilon_1^2(\omega)+\varepsilon_2^2(\omega)} \quad \textbf{(VI. 29)}$$

$$I(\omega) = \sqrt{2}(\omega)\left(\sqrt{\varepsilon_1(\omega)^2+\varepsilon_2(\omega)^2} - \varepsilon_1(\omega)\right)^{1/2} \quad \textbf{(VI. 30)}$$

The complex dielectric function is presented **(Figure IV.19a)** for pure and CZO structures (*x*= 6,25 and 12.5 at%). The imaginary part consists of three main peaks. Generally, the first peak, located at around ~ 5eV eV, corresponds to electron excitation of O-*2p* state to

Zn*4s* state or Cu-*3d* state. The intensity of this peak is slightly increased with Cu doping becauseof the replacement of Zn atom s by Cu ones. The second peak, located at around ~ 9.9eV eV, results from electron excitation of Zn-*3d* state near the top of valence band to O-*2p* state nearthe bottom of conduction band. The excitation of Zn-*3d* state to O-*2s* state constitutes the third strong peak, which is located at around ~ 14.9eV eV and decreases with Cu doping. This causes the decrease of Zn-*3d* states which are responsible for the concerned transition. Besides, an inappreciable shift of dielectric function toward the lower energy is due to the slight shrinking of band gap energy when going from pure structure to doped one. Also, the calculated static dielectric function $\varepsilon_1(0)$ is slightly affected by Cu doping; $\varepsilon_1(0) = 2.455$ for $x= 0\%$, 2.457 for $x= 6.25$ at% and 2.454 for $x= 12.5$ at% **(Inset in Figure IV.19a)** while a significant change is observed for the experimental static dielectric function (Figure VI.11). This may be due to the surface morphology not taken into account in the present DFT+LDA+U calculations.

Other optical properties, such as complex refractive index **(Figure IV.19b)**, complex conductivity function **(Figure IV.19c)** absorption coefficient **(Figure IV.19d)**, optical reflectivity **(Figure IV.19e)** and energy-loss function **(Figure IV.19f)** are also presented. It is observed that the absorption is near zero below absorption edges, which correspond to the band gap values, and presents tow more pronounced peaks at about 16.6 and 34.6 eV. Furthermore, the strong peak of the energy loss function (around 22.0 eV) corresponds to the abrupt reduction of the reflectivity.

The refractive index seems unchanged by Cu doping (around 1.56) and tends to be constant for lower photon energy in the visible light range **(Inset in Figure IV.19b)**, which is inconsistent with the experimental findings **(Figure VI.11)**. In addition, the refractive index and the absorption coefficient exhibit a similar behavior to those obtained experimentally in this work within the considered energy range (energy corresponding to the visible range).

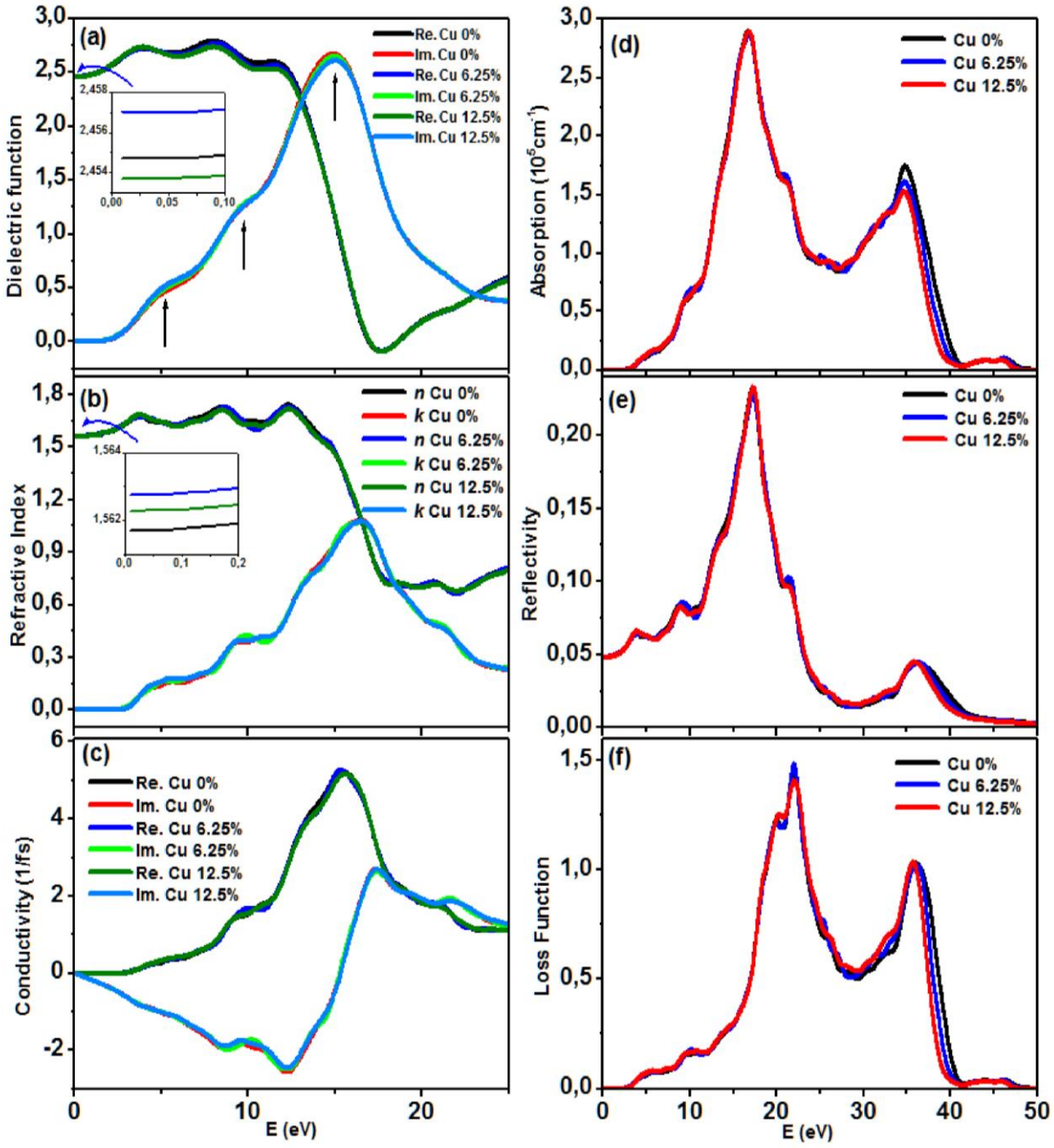

Figure IV.19. Complex dielectric function **(a)**, complex refractive index **(b)**, complex conductivity function **(c)** absorption coefficient **(d)** optical reflectivity **(e)** and energy-loss function **(f)** for pure ZnO and CZO wurtzite structures (x= 6,25%, 12.5 at%). Inset in (a) shows the evolution of real part of the complex dielectric (ε_1**)** and inset in (b) exhibits the refractive index n for lower photon energy**.**

IV.4. Conclusions

Pure and copper-doped zinc oxide (CZO) thin films at different contents *x* ($0 \leq x \leq 0.125$) were investigated both experimentally and theoretically. Structural results show that all samples exhibited a polycrystalline with wurtzite hexagonal phase. The (002) preferential orientation is degraded and leads to the enhancement along (100) orientation by increasing Cu-doping. The crystallite size, strain and growth mode are significantly influenced by the increasing level of Cu doping. Surface morphology reveals that grain size is strongly affected by the Cu-doping and the surface becomes more rough. The film thickness is slightly influenced by Cu doping. The transparency of films presents an increase in the visible region and the band gap energy slightly shrinks as the Cu content increases, indicating that the doping process by Cu makes these films suitable for use in opto-electronic applications.

In the calculation point of view, DFT+U with convenient effective Hubbard U values enhance the band gap. The ferromagnetic ground states at a geometry configuration with the closest Cu impurities in CZO structure is found the more stable and Cu3d states are distributed around Fermi level. Besides, the covalency for both Cu-O and Zn-O bonds is affected by Cu doping. The imaginary part consists of three main peaks whose intensity is slightly influenced by impurity doping. Cu doping leaves the static refractive index unchanged.

References

[1] B.G. Shohany, A.K. Zak, Doped ZnO nanostructures with selected elements-Structural, morphology and optical properties: A review. Ceramics International, 2020, vol. 46.5, p.5507-5520.

[2] D.R. Miller, S.A. Akbar, P.A. Morris, Nanoscale metal oxide-based heterojunctions for gas sensing: a review. Sensors and Actuators B: Chemical, 2014, vol. 204, p.250-272.

[3] S. Park, C.-H. Kim, W.-J. Lee, S. Sung, M.-H. Yoon, Sol-gel metal oxide dielectrics for all-solution-processed electronics. Materials Science and Engineering: R: Reports, 2017, vol 114, p. 1-22.

[4] A.B. Djurišić, Y.H. Leung, A.M.C. Ng, Strategies for improving the efficiency of semiconductor metal oxide photocatalysis. *Materials Horizons*, 2014, vol 1.4, p.400-410.

[5] H.A. Al-Khanbashi, W. Shirbeeny, A. Al-Ghamdi, L.M. Bronstein, W.E. Mahmoud, Development of highly conductive and transparent copper doped zinc oxide thin films via 2-methoxyethanol modified sol–gel dip-coating technique. *Ceramics International*, 2014, vol 40.1, p. 1927-1932.

[6] W. Vallejo, A. Cantillo, B. Salazar, C. Diaz-Uribe, W. Ramos, E. Romero, M. Hurtado, Comparative Study of ZnO Thin Films Doped with Transition Metals (Cu and Co) for Methylene Blue Photodegradation under Visible Irradiation. Catalysts, 2020, vol. 10.5, p. 528.

[7] A. Kronenberger, A. Polity, D.M. Hofmann, B.K. Meyer, A. Schleife, F. Bechstedt, Structural, electrical, and optical properties of hydrogen-doped ZnO films. Physical Review B, 2012, vol.. 86.11, p.115334.

[8] R. Amari, A. Mahroug, A. Boukhari, B. Deghfel, N. Selmi, optical and luminescence properties of ZnO thin films prepared by sol-gel spin-coating method: effect of precursor concentration. *Chinese Physics Letters*, 2018, vol. 35.1, p. 016801.

[9] A. Mahroug, R. Amari, A. Boukhari, B. Deghfel, L. Guerbous, N. Selmi, Synthesis, structural, morphological, electronic, optical and luminescence properties of pure and manganese-doped zinc oxide nanostructured thin films: effect of doping. Journal of Nanoelectronics and Optoelectronics, 2018, vol.13.5, p.732-742.

[10] D. Shuang, X. Zhu, J. Wang, X. Zhong, G. Huang, C. He, The influence of Mn content on luminescence properties in Mn-doped ZnO films deposited by ultrasonic spray assisted chemical vapor deposition. *Applied surface science*, 2011, vol. 257.14, p. 6085-6088.

[11] A. Mhamdi, R. Mimouni, A. Amlouk, M. Amlouk, S. Belgacem, Study of copper doping effects on structural, optical and electrical properties of sprayed ZnO thin films. *Journal of alloys and compounds*, 2014, vol. 610, p. 250-257.

[12] Y. Darma, S. Muhammady, Y.N. Hendri, E. Sustini, R. Widita, K. Takase, Tuning the point-defect evolution, optical transitions, and absorption edge of zinc oxide film by thermal exposure during molecular beam epitaxy growth. Materials Science in Semiconductor Processing, 2019, vol. 93, p. 50-58.

[13] Z. Vakulov, E. Zamburg, D. Khakhulin, O. Ageev, Thermal stability of ZnO thin films fabricated by pulsed laser deposition. Materials Science in Semiconductor Processing, 2017, vol. 66, p. 21-25.

[14] W. Thongsuksai, G. Panomsuwan, A. Rodchanarowan, Fast and convenient growth of vertically aligned ZnO nanorods via microwave plasma-assisted thermal evaporation. Materials Letters, 2018, vol.224, p. 50-53.

[15] S. Syed Zahirullah, J. Joseph Prince, P. Fermi Hilbert Inbaraj, Structural and optical properties of Cu-doped ZnO nanorods by silar method. *Materials technology*, 2017, vol. 32.12, p. 755-763.

[16] T. Saidani, M. Zaabat, M. Aida, B. Boudine, Effect of copper doping on the photocatalytic activity of ZnO thin films prepared by sol–gel method. *Superlattices and Microstructures*, 2015, vol. 88, p. 315-322.

[17] S. Osali, H. Esfahani, F. Dabir, P. Tajaslan, Structural and electro-optical properties of electrospun Cu-Doped ZnO thin films. *Solid State Sciences*, 2019, vol. 98, p. 106038

[18] A. Sreedhar, J.H. Kwon, J. Yi, J.S. Kim, J.S. Gwag, Enhanced photoluminescence properties of Cu-doped ZnO thin films deposited by simultaneous RF and DC magnetron sputtering. *Materials Science in Semiconductor Processing*, 2016, vol. 49, p.8-14.

[19] K. Joshi, M. Rawat, S.K. Gautam, R. Singh, R. Ramola, F. Singh, Band gap widening and narrowing in Cu-doped ZnO thin films. *Journal of Alloys and Compounds*, 2016, 680, p. 252-258.

[20] S. Roguai, A. Djelloul, Abdelkader. A structural and optical properties of Cu-doped ZnO films prepared by spray pyrolysis. *Applied Physics A*, 2020, vol. 126.2, p.1-8.

[21] N.H. Hashim, S. Subramani, M. Devarajan, A.R. Ibrahim, Structural and surface characterization of undoped ZnO and Cu doped ZnO using sol–gel spin coating method. *Journal of Materials Science: Materials in Electronics*, 2016, vol. 27.4, p. 3520-3530.

[22] A.R. Nimbalkar, M.G. Patil, Synthesis of highly selective and sensitive Cu-doped ZnO thin film sensor for detection of H2S gas. Materials Science in Semiconductor Processing, 2017, vol. 71, p. 332-341.

[23] P. Shewale, Y. Yu, UV photodetection properties of pulsed laser deposited Cu-doped ZnO thin film. *Ceramics International*, 2017, vol. 43.5, p.4175-4182.

[24] G.-J. Chen, S.-R. Jian, J.-Y. Juang, Surface analysis and optical properties of Cu-doped ZnO thin films deposited by radio frequency magnetron sputtering. Coatings, 2018, vol. 8.8, p. 266

[25] J.-H. Lee, K. Oh, K. Jung, K. Wilson, M.-J. Lee, Tuning the morphology and properties of nanostructured Cu-ZnO thin films using a two-step sputtering technique. Metals, 2020 vol., 10.4, p. 437.

[26] N. Narayanan, N. Deepak, Enhancement of visible luminescence and photocatalytic activity of ZnO thin films via Cu doping. Optik, 2018, vol. 158, p. 1313-1326.

[27] V.I. Anisimov, F. Aryasetiawan, A. Lichtenstein, First-principles calculations of the electronic structure and spectra of strongly correlated systems: the LDA+ U method. *Journal of Physics: Condensed Matter*, 1997, vol. 9.4, p. 767.

[28] M. Yaakob, N. Hussin, M. Taib, T. Kudin, O. Hassan, A. Ali, M. Yahya, First principles LDA+ U calculations for ZnO materials. Integrated Ferroelectrics, 2014, vol. 155.1, p. 15-22.

[29] J.-Q. Wen, J.-M. Zhang, Z.-G. Qiu, X. Yang, Z.-Q. Li, The investigation of Ce doped ZnO crystal: the electronic, optical and magnetic properties. Physica B: Condensed Matter, 2018, vol. 534, p. 44-50.

[30] Q. Hou, D. Xi, W. Li, X. Jia, Z. Xu, First-principles research on the optical and electrical properties and mechanisms of In-doped ZnO. Physica B: Condensed Matter, 2018, vol. 537, p. 258-266.

[31] Z. Ma, F. Ren, X. Ming, Y. Long, A.A. Volinsky, Cu-doped ZnO electronic structure and optical properties studied by first-principles calculations and experiments. Materials, 2019, vol. 12.1, p. 196.

[32] F. Li, C. Zhang, M. Zhao, Magnetic and optical properties of Cu-doped ZnO nanosheet: First-principles calculations. Physica E: Low-dimensional Systems and Nanostructures, 2013, vol. 53, p. 101-105.

[33] L. Chen, S. Li, Y. Cui, Z. Xiong, H. Luo, Y. Gao, Manipulating the electronic and magnetic properties of ZnO monolayer by noble metal adsorption: a first-principles calculations. *Applied Surface Science*, 2019, vol. 479, p. 440-448.

[34] A.K. Nayek, H. Luitel, B. Haldar, D. Sanyal, M. Chakrabarti, Ferromagnetic property of copper doped ZnO: A first-principles study. *Computational Condensed Matter*, 2020, vol. 23, p. e00455.

[35] C. Xia, F. Wang, C. Hu, Theoretical and experimental studies on electronic structure and optical properties of Cu-doped ZnO. Journal of alloys and compounds, 2014, vol. 589, p. 604-608.

[36] D. Fang, A. De Sarkar, R. Zhang, First-principles study on the origin of ferromagnetism in n-type Cu-doped ZnO. *Solid state communications*, 2012, vol. 152.12, p.1057-1060.

[37] C. Feng, Z. Chen, W. Li, F. Zhang, X. Li, L. Xu, M. Sun, First-principle calculation of the electronic structures and optical properties of the metallic and nonmetallic elements-doped ZnO on the basis of photocatalysis. Physica B: Condensed Matter, 2019, vol. 555, p. 53-60.

[38] S. Sriram, K. Lalithambika, A. Thayumanavan, Experimental and theoretical investigations of photocatalytic activity of Cu doped ZnO nanoparticles. *Optik*, 2017, vol. 139, p.299-308.

[39] M.A. Lahmer, The effect of hydrogen adsorption on the properties of undoped and Cu-doped ZnO ($10\bar{1}0$) surfaces: A first-principles study. Journal of Physics and Chemistry of Solids, 2016, vol. 89, p.89-96.

[40] Q. Wang, J. Wang, X. Zhong, Q. Tan, Y. Zhou, The magnetic phase transition in Cu-doped ZnO: From bulk to nanocluster. Solid state communications, 2012, vol. 152.1, p. 50-52.

[41] Z. Long, L. Peng-Fei, Y. Zhong-Yuan, L. Yu-Min, W. Dong-Lin, Y. Han, First-principles study of electronic and optical properties in wurtzite Zn1–xCuxO. Chinese Physics B, 2010 vol., 19.5, p.056104.

[42] B.-S. Kang, K.-S. Kim, S.-C. Yu, H. Chae, First-principles study for ferromagnetism of Cu-doped ZnO with carrier doping. Journal of Solid State Chemistry, 2013, vol. 198: 120-124.

[43] V. Mendoza-Estrada, A. González-García, D. Barragán-Yani, W. López-Pérez, J. Rivera-Julio, R. González-Hernández, Ferromagnetic orderings in CoxCuyZn1−(x+ y) O by GGA and GGA+ U formalisms within density functional theory. Computational Materials Science, 2017, vol. 126, p. 344-350.

[44] A.M. Peiró, P. Ravirajan, K. Govender, D.S. Boyle, P. O'Brien, D.D. Bradley, J. Nelson, J.R. Durrant, Hybrid polymer/metal oxide solar cells based on ZnO columnar structures. Journal of Materials Chemistry, 2006, vol. 16.21, p.2088-2096.

[45] S. Yang, Y. Zhang, D. Mo, Spectroscopic ellipsometry studies of sol-gel-derived Cu-doped ZnO thin films. Thin Solid Films, 2014, vol. 571: 605-608.

[46] P. Jongnavakit, P. Amornpitoksuk, S. Suwanboon, N. Ndiege, Preparation and photocatalytic activity of Cu-doped ZnO thin films prepared by the sol–gel method. Applied Surface Science, 2012, vol.258.20, p.8192-8198.

[47] A. El Sayed, G. Said, S. Taha, A. Ibrahim, F. Yakuphanoglu, Influence of copper incorporation on the structural and optical properties of ZnO nanostructured thin films. Superlattices and Microstructures, 2013, vol. 62, p. 47-58.

[48] L. Xu, F. Xian, G. Zheng, M. Lai, Realization of strong violet and blue emissions from ZnO thin films by incorporation of Cu ions. *Materials Research Bulletin*, 2018, vol. 99 , p. 144-151.

[49] I. Horcas, R. Fernández, J. Gomez-Rodriguez, J. Colchero, J. Gómez-Herrero, A. Baro, WSXM: a software for scanning probe microscopy and a tool for nanotechnology. *Review of scientific instruments*, 2007, vol. 78.1: 013705.

[50] M. Salem, I. Massoudi, S. Akir, Y. Litaiem, M. Gaidi, K. Khirouni, Photoelectrochemical and opto-electronic properties tuning of ZnO films: Effect of Cu doping content. Journal of Alloys and Compounds, 2017 vol., 722, p. 313-320.

[51] Y. Kim, J.-Y. Leem, Effects of precursor concentration on structural and optical properties of ZnO thin films grown on muscovite mica substrates by sol–gel spin-coating. *Journal of nanoscience and nanotechnology*, 2016, vol. 16.5: 5186-5189.

[52] A. Saboor, S.M. Shah, H. Hussain, Band gap tuning and applications of ZnO nanorods in hybrid solar cell: Ag-doped verses Nd-doped ZnO nanorods. Materials Science in Semiconductor Processing, 2019, vol. 93, p. 215-225.

[53] Y. Liu, H. Liu, Y. Yu, Q. Wang, Y. Li, Z. Wang, Structural and optical properties of ZnO thin films with heavy Cu-doping prepared by magnetron co-sputtering. Materials Letters, 2015, vol. 143 ,p.319-321.

[54] V. Ganesh, G. Salem, I. Yahia, F. Yakuphanoglu, Synthesis, optical and photoluminescence properties of Cu-doped ZnO nano-fibers thin films: nonlinear optics. Journal of Electronic Materials, 2018, vol. 47.3, p. 1798-1805.

[55] M. Sajjad, I. Ullah, M. Khan, J. Khan, M.Y. Khan, M.T. Qureshi, Structural and optical properties of pure and copper doped zinc oxide nanoparticles. Results in Physics, 2018, vol. 9, p.1301-1309.

[56] K.-S. Ahn, T. Deutsch, Y. Yan, C.-S. Jiang, C.L. Perkins, J. Turner, M. Al-Jassim, Synthesis of band-gap-reduced p-type ZnO films by Cu incorporation. *Journal of Applied Physics*, 2007, vol. 102.2: 023517.

[57] M. Mazhdi, J. Saydi, M. Karimi, J. Seidi, F. Mazhdi, A study on optical, photoluminescence and thermoluminescence properties of ZnO and Mn doped-ZnO nanocrystalline particles. *Optik*, 2013, vol.124.20, p. 4128-4133.

[58] M. DrDomenico Jr, S.H. Wemple, Oxygen-octahedra ferroelectrics. I. Theory of electro-optical and nonlinear optical effects. Journal of Applied Physics, 1969, vol. 40.2, p. 720-734.

[59] Y. Caglar, Sol–gel derived nanostructure undoped and cobalt doped ZnO: Structural, optical and electrical studies. Journal of alloys and Compounds, 2013, vol. 560, p. 181-188.

[60] E.Ş. Tüzemen, S. Eker, H. Kavak, R. Esen, Dependence of film thickness on the structural and optical properties of ZnO thin films. Applied Surface Science, 2009, vol. 255.12, p. 6195-6200.

[61] S.J. Clark, M.D. Segall, C.J. Pickard, P.J. Hasnip, M.I. Probert, K. Refson, M.C. Payne, First principles methods using CASTEP. Zeitschrift für Kristallographie-Crystalline Materials, 2005, vol. 220.5-6, p. 567-570.

[62] J.P. Perdew, K. Burke, M. Ernzerhof, Generalized gradient approximation made simple. *Physical review letters*, 1996, vol. 77.18, p.3865

[63] R. Amari, B. Deghfel, A. Mahroug, A.A. Mohamad, A. Boukhari, N. Selmi, Effects of Mn doping on the structural, morphological, electronic and optical properties of ZnO thin films by sol-gel spin coating method: An experimental and DFT+ U study. Physica B: Condensed Matter, 2020, vol. 577, p. 411766.

[64] D. Vanderbilt, Soft self-consistent pseudopotentials in a generalized eigenvalue formalism. Physical review B, 1990, vol. 41.11, p.7892.

[65] S. Guo, Q. Hou, C. Zhao, Y. Zhang, Study of the effect of Cu heavy doping on band gap and absorption spectrum of ZnO. Chemical Physics Letters, 2014, vol. 614, p. 15-20.

[66] V. Mendoza-Estrada, W. López-Pérez, R. González-Hernández, A. González-García, Electronic structure and magnetic order in CuxZn (1− x) O: A study GGA and GGA+ U. Physica B: Condensed Matter, 2019, vol. 557, p.74-81.

[67] S. Horzum, E. Torun, T. Serin, F. Peeters, Structural, electronic and optical properties of Cu-doped ZnO: experimental and theoretical investigation. Philosophical Magazine, 2016, vol. 96.17, p. 1743-1756.

[68] D. Sanchez-Portal, E. Artacho, J.M. Soler, Projection of plane-wave calculations into atomic orbitals. *Solid State Communications*, 1995, vol. 95.10, p.685-690.

[69] R.S. Mulliken, Electronic population analysis on LCAO–MO molecular wave functions. I. The Journal of Chemical Physics, 1955, vol. 23.10, p.1833-1840.

[70] A. Ciechan, P. Bogusławski, Transition metal ions in ZnO: effects of intrashell coulomb repulsion on electronic properties. Optical Materials, 2018, vol. 79, p.264-268.

[71] Q.-J. Liu, Z.-T. Liu, J.-C. Chen, L.-P. Feng, H. Tian, First-principles study of structural, mechanical, electronic and optical properties of 3R-and 2H-CuGaO2. *Physica B: Condensed Matter*, 2011, vol. 406.18, p.3377-3382.

[72] M. Khan, A. Kashyap, A. Solanki, T. Nautiyal, S. Auluck, Interband optical properties of Ni 3 Al. Physical Review B, 1993, vol. 48.23, p.16974.

[73] K. Harun, N.A. Salleh, B. Deghfel, M.K. Yaakob, A.A Mohamad, DFT+ U calculations for electronic, structural, and optical properties of ZnO wurtzite structure: A review. Results in Physics, 2020, vol. 16, p. 102829.

General conclusions and perspectives

GENERAL CONCLUSIONS AND PERSPECTIVES

The aim of this thesis was the development by sol-gel method of pure ZnO and copper-doped zinc oxide (CZO) thin films with somewhat higher Cu contents (x) (x = 1%, 3.12%, 6,25% and 12.5 at%) and low thickness**.** Starting from **,** Copper (II) chloride, Zinc acetate dihydrate and 2-Methoxyethanol as a dopant source, starting material and stabilizer**,** the preparation protocol by spin coating technique of undoped and doped-ZnO thin films on glass substrates, was developed.

To ensure well crystallization of the prepared thin films, ideal experimental conditions were adopted, which based on our experimental literature review, such as molar ratio of the solvent to metal ions, stirring, aging, cleaning and drying of substrates, spinning, preheating and annealing. Various techniques were employed to investigate the fabricated samples such as X-ray diffraction, Atomic Force Microscopy, Field emission scanning electron microscopy and Ultraviolet-visible UV-vis spectrophotometry.

On the other hand, first-principles calculations of structural, electronic, magnetic and optical properties of pure and CZO wurtzite materials (x= 6,25%, 12.5 at%) were performed by DFT as implemented in CASTEP code . The generalized gradient approximation (GGA) in the scheme of Perdew–Burke–Ernzerhof (PBE) was employed to describe the exchange-correlation function. ZnO supercell model, derived from the optimized ZnO wurtzite primitive cell, and substitutional method were used to achieve the considered Cu content. To ensure well convergence of the calculation, ideal input criteria of computer code were adopted, which based on our theoretical literature review, such as the valence-electron configurations for the O, Zn and Cu atoms, the energy cut-off, pseudopotential, the sampling of the Brillouin zone by k-point meshes, the optimization convergence for maximum force, energy change, maximum displacement, maximum stress and the SCF convergence threshold.

The semiempirical LDA+U approach was used with convenient effective Hubbard U values for Zn *3d, Cu 3d* and *O 2p* electrons and the ferromagnetic phase of CZO structure was adopted in which two Cu atoms substitute two Zn atoms according to different geometry configurations.

Experimental investigations indicates that structural results show that all samples exhibited a polycrystalline with wurtzite hexagonal phase. The (002) preferential orientation is degraded and leads to the enhancement along (100) orientation by increasing Cu-doping. The

crystallite size, strain and growth mode are significantly influenced by the increasing level of Cu doping. Surface morphology reveals that grain size is strongly affected by the Cu-doping and the surface becomes more rough. The film thickness is slightly influenced by Cu doping. The transparency of films presents an increase in the visible region and the band gap energy slightly shrinks as the Cu content increases.

DFT+U calculations reveal that convenient effective Hubbard U values enhance the band gap. The ferromagnetic ground states at a geometry configuration with the closest Cu impurities in CZO structure is found the more stable and Cu3d states are distributed around Fermi level. Besides, the covalency for both Cu-O and Zn-O bonds is affected by Cu doping. The imaginary part consists of three main peaks whose intensity is slightly influenced by impurity doping. As Cu doping increases, the static refractive index is found unchanged.

Finally, it is worth noting that tow valuable results can be extracted from the present study,

In the experimental point of view, the transparency and the band gap energy of CZO thin films were found to be influenced by Cu content in the visible region, indicating that the doping process by Cu makes these films suitable for use in opto-electronic devices, in which CZO thin films can absorb the ultra violet wave range in the spectrum and it is transparent to the visible light.

In the theoretical point of view, including DFT+U correction within standard DFT reveals that convenient effective Hubbard U values enhance significantly the band gap energy and its corresponding electronic and optical properties.

In perspective, the present calculation reveals the importance of including DFT+U correction within standard DFT. So, it is interesting to verify the validity of such model for other transition metals and various defects in ZnO host lattice such as zinc vacancies(V_{Zn}), oxygen interstitial (O_i) oxygen vacancies (V_O), zinc interstitials (Zn_i), oxygen antisites (O_{Zn}) and zinc antisites (Zn_O). On the hand, Cu-doping exhibits significant influence on the properties of CZO thin films, which allows us to thinking about use of other elements in the transition-metals group to make their properties controllable and to widen the range of their potential applications. So, the issue is still left open.

Abstract: In the present work, pure ZnO and copper-doped zinc oxide (CZO) thin films at different contents (*x*) were synthesized by sol–gel spin coating process and investigated using various techniques. All samples exhibited a polycrystalline with wurtzite hexagonal phase. The grain size increased and changed its growth mode from c-axis growth to lateral one and the surface morphology was strongly influenced by Cu doping. Optical properties of CZO thin films were investigated. As *x* increased, the transparency of films was generally increased in the visible region and the band gap energy (*Eg*) presented a slight shrinking. Ferromagnetic phase was adopted within density functional theory corrected by Hubbard method (DFT+LDA+U) to investigate the properties of pure and CZO structure. The closest Cu impurities gave the more stable configuration. Cu3d states were distributed around Fermi level inducing a major contribution to the magnetic moment. A mix of ionic and covalent bonding was remarked. DFT+LDA+U enhanced significantly the calculated *Eg*, which presented a narrowing with *x*. The imaginary part of the dielectric functions presented three main peaks and the static dielectric constants were slightly influenced by Cu doping.
Key-Words: Density Functional Theory; Copper-doped zinc oxide thin films; Sol-gel technique; Magnetic phase; Spin coating method; LDA+U approach.

ملخص: في العمل الحالي، تم تحضير الطبقات الرقيقة لأكسيد الزنك النقي و المطعم بالنحاس (CZO) بتراكيز مختلفة (*x*) بواسطة طريقة الطلاء بالتدوير محلول–هلام وتم فحصها باستخدام تقنيات مختلفة. أبدت جميع العينات طور متعدد البلورات مع وورتزيت سداسي. زاد حجم الحبيبات وتغير نمط نموها من نمو بموازاة المحور C إلى نمو جانبي وتأثر شكل السطح بشدة مع التطعيم بالنحاس. تم فحص الخواص الضوئية للطبقات الرقيقة CZO. مع زيادة *x*، زادت شفافية الطبقات الرقيقة بشكل عام في المنطقة المرئية وأظهرت طاقة فجوة النطاق (*Eg*) إنكماشا طفيفًا. تم اعتماد الطور حديدي المغنطة ضمن نظرية دالية الكثافة المصححة بطريقة Hubbard (DFT+LDA+U) لتقصي خصائص بنية ZnO النقية و المطعمة CZO. أعطت التطعيم بشوائب النحاس القريبة من بعضها البعض بنية أكثر استقرارًا. تم توزيع حالات Cu3d حول مستوى Fermi مما أدى إلى مساهمة كبيرة في العزم المغناطيسي. تمت ملاحظة مزيج من الروابط الأيونية والتساهمية. حسن نموذج DFT+LDA+U بشكل ملحوظ القيمة المحسوبة *Eg* والتي أظهرت انكماشا مع زيادة *x*. ابدى الجزء التخيلي من دالة العزل الكهربائي ثلاث قمم رئيسية وتأثرت ثوابت العزل الكهربائي الساكنة بشكل طفيف مع التطعيم بالنحاس.

الكلمات المفاتيح: نظرية دالية الكثافة؛ التطعيم بالنحاس لطبقات أكسيد الزنك؛ تقنية محلول–هلام؛ الطور المغناطيسي؛ طريقة الطلاء بالتدوير؛ تقريب LDA+ U.

Résumé : Dans le présent travail, des couches minces d'oxyde de zinc pur (ZnO) et dopé au cuivre (CZO) à différentes concentration (*x*) ont été synthétisés par un procédé de revêtement par centrifugation sol-gel et ont été étudiés par diverses techniques. Tous les échantillons présentaient une phase hexagonale polycristalline avec wurtzite. La taille des grains a augmenté et son mode de croissance a changé de la croissance suivant l'axe *c* à la croissance latérale. La morphologie de la surface a été fortement influencée par le dopage au Cu. Les propriétés optiques des couches minces de CZO ont été étudiées. Lorsque *x* augmente, la transparence des couches augmente généralement dans la région visible et l'énergie de la bande interdite (Eg) présente un léger rétrécissement. La phase ferromagnétique a été adoptée dans la théorie de la fonctionnelle de la densité corrigée par la correction de Hubbard (DFT+LDA+U) pour étudier les propriétés de la structure CZO. Les impuretés de Cu les plus proches ont donné la configuration la plus stable. Les états Cu3d sont distribués autour du niveau de Fermi induisant une contribution majeure au moment magnétique. Un mélange de liaisons ioniques et covalentes a été remarqué. DFT+LDA+U a amélioré significativement Eg calculé, qui a présenté un rétrécissement avec *x*. La partie imaginaire des fonctions diélectriques présente trois pics principaux et les constantes diélectriques statiques sont légèrement influencées par le dopage Cu.

Mots-clés : Théorie de la fonctionnelle de la densité ; Couches minces d'oxyde de zinc dopé au cuivre ; Technique sol-gel ; Phase magnétique ; Méthode de revêtement par rotation ; Approche LDA+U.